

AD-A125 882

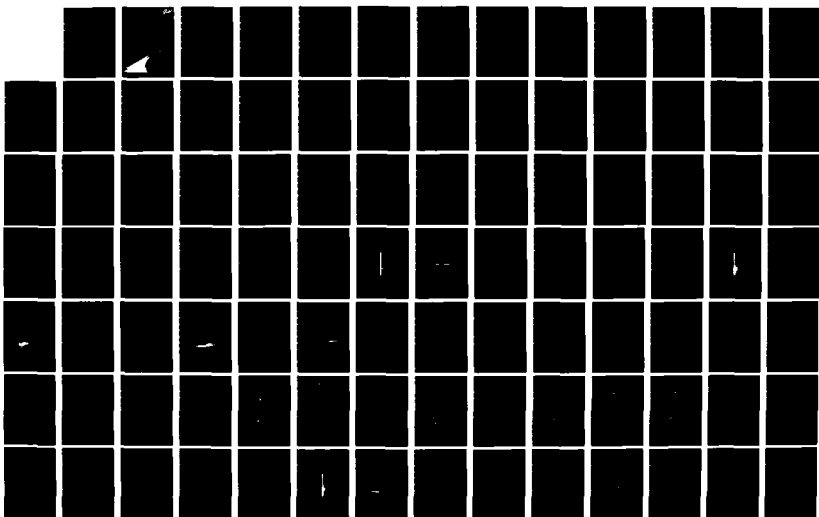
A NUMERICAL STUDY OF STRAKE AERODYNAMICS(U) NIELSEN
ENGINEERING AND RESEARCH INC MOUNTAIN VIEW CA
G D KERLICK ET AL. JUL 82 NEAR-TR-270 N00014-78-C-0388

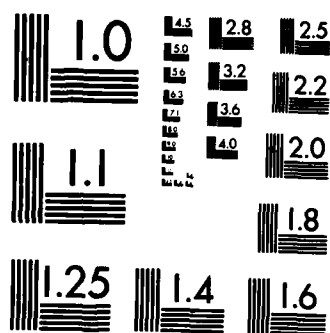
1/2

UNCLASSIFIED

F/G 20/4

NL

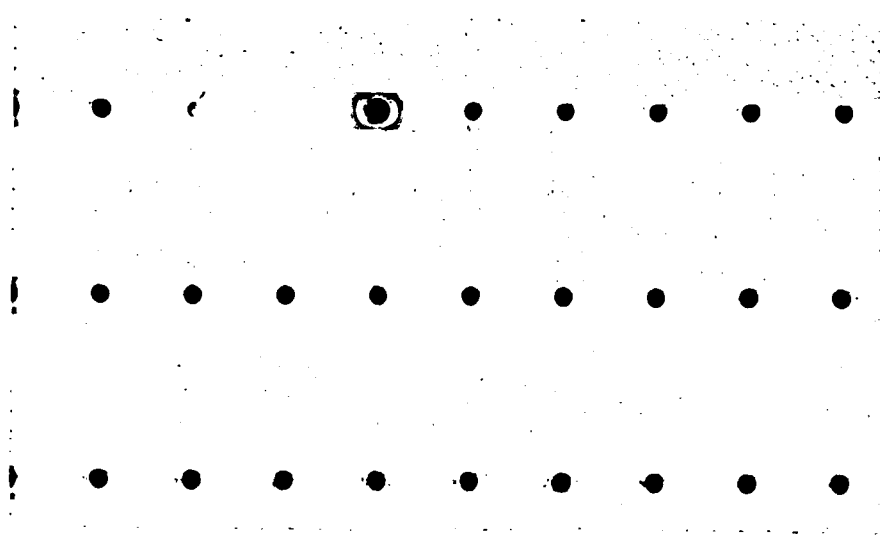




MICROCOPY RESOLUTION TEST CHART
NATIONAL BUREAU OF STANDARDS-1963-A

12

WA 125882



DTIC FILE COPY

DTIC
ELECTE
MAR 22 1983
D

DISTRIBUTION STATEMENT A
Approved for public release;
Distribution Unlimited

83 03 21 059

**NIELSEN ENGINEERING
AND RESEARCH, INC.**

OFFICES: 510 CLYDE AVENUE / MOUNTAIN VIEW, CALIFORNIA 94043 / TELEPHONE (415) 968-9457

A NUMERICAL STUDY OF STRAKE AERODYNAMICS

by

G. D. Kerlick, G. H. Klopfer
and D. Nixon



Accession For	
NTIS GRA&I	<input checked="" type="checkbox"/>
DTIC TAB	<input type="checkbox"/>
Unannounced	<input type="checkbox"/>
Justification	
By	
Distribution/	
Availability Codes	
Dist	Avail and/or Special
A	

NEAR TR 270
July 1982

Prepared under Contract No. N00014-78-C-0388

for

OFFICE OF NAVAL RESEARCH
Arlington, Virginia 22217

by

NIELSEN ENGINEERING & RESEARCH, INC.
510 Clyde Avenue, Mountain View, CA 94043
Telephone (415) 968-9457

Unclassified

SECURITY CLASSIFICATION OF THIS PAGE (When Data Entered)

REPORT DOCUMENTATION PAGE		READ INSTRUCTIONS BEFORE COMPLETING FORM
1. REPORT NUMBER	2. GOVT ACCESSION NO. AD-A125882	3. RECIPIENT'S CATALOG NUMBER
4. TITLE (and Subtitle) A NUMERICAL STUDY OF STRAKE AERODYNAMICS		5. TYPE OF REPORT & PERIOD COVERED Final Report 7/80 - 3/82
7. AUTHOR(s) G. D. Kerlick, G. H. Klopfer, and D. Nixon		6. PERFORMING ORG. REPORT NUMBER NEAR TR 270
9. PERFORMING ORGANIZATION NAME AND ADDRESS Nielsen Engineering & Research, Inc. 510 Clyde Avenue Mountain View, CA 94043		8. CONTRACT OR GRANT NUMBER(s) N00014-78-C-0388
11. CONTROLLING OFFICE NAME AND ADDRESS Office of Naval Research 800 N. Quincy Street Arlington, VA 22217		10. PROGRAM ELEMENT, PROJECT, TASK AREA & WORK UNIT NUMBERS
14. MONITORING AGENCY NAME & ADDRESS (if different from Controlling Office)		12. REPORT DATE July 1982
		13. NUMBER OF PAGES 133
		15. SECURITY CLASS. (of this report) Unclassified
		15a. DECLASSIFICATION/DOWNGRADING SCHEDULE
16. DISTRIBUTION STATEMENT (of this Report) Approved for public release; distribution unlimited.		
17. DISTRIBUTION STATEMENT (of the abstract entered in Block 20, if different from Report)		
18. SUPPLEMENTARY NOTES		
19. KEY WORDS (Continue on reverse side if necessary and identify by block number) Vorticity Numerical Simulation Vortex Shedding Two-Dimensional Flow Three-Dimensional Flow Navier-Stokes Equations		
20. ABSTRACT (Continue on reverse side if necessary and identify by block number) As part of a combined experimental and analytical study of vortex shedding at sharp edges characteristic of strakes on fighter aircraft, numerical simulations were made of a two-dimensional and a three-dimensional case. The former is a sharp-edge flat plate normal to the flow, for which some experimental data were taken earlier in this program. The latter is a double-delta, sharp-edged wing at angle of attack. In both cases, a free-stream Mach number of 0.5 was used. The objective of the work was to		

DD FORM 1 JAN 73 1473

EDITION OF 1 NOV 65 IS OBSOLETE

Unclassified

SECURITY CLASSIFICATION OF THIS PAGE (When Data Entered)

Unclassified

SECURITY CLASSIFICATION OF THIS PAGE(When Data Entered)

investigate the suitability of using the numerical simulation to augment experimental flow field data, after the major features of the simulation were verified by data.

Two existing Navier-Stokes codes developed at Ames Research Center NASA were used for the numerical simulations. Neither code had been used in an application involving flow separation, sharp edges, and the aggregation of vorticity into small regions in the flow such as the two present applications demonstrate. The applications of the codes were largely successful, in that for both applications the numerical flow fields generally reproduced the gross flow features exhibited by experimental data.

The larger objective of demonstrating the suitability of using numerical simulations to augment experimental data was not achieved. The principal difficulty in both applications was mesh resolution. In the two-dimensional case, the mesh resolution was inadequate to determine the details of the boundary layer on the windward side, particularly near the edge where experimental data is very difficult to obtain. In the three-dimensional case, the problem was exacerbated by the requirement to store more information. In this case there were differences in the location of the peak suction pressure on the wing and the vorticity distribution above the wing which were caused, at least in part, by mesh limitations. The objective is felt to be attractive and feasible but considerable care must be taken in the numerical simulation to permit the mesh to capture and accurately represent important flow phenomena.

Unclassified

SECURITY CLASSIFICATION OF THIS PAGE(When Data Entered)

SUMMARY

As part of a combined experimental and analytical study of vortex shedding at sharp edges characteristic of strakes on fighter aircraft, numerical simulations were made of a two-dimensional and a three-dimensional case. The former is a sharp-edge flat plate normal to the flow, for which some experimental data were taken earlier in this program. The latter is a double-delta, sharp-edge wing at angle of attack. In both cases, a free-stream Mach number of 0.5 was used. The objective of the work was to investigate the suitability of using the numerical simulation to augment experimental flow field data, after the major features of the simulation were verified by data.

Two existing Navier-Stokes codes developed at Ames Research Center NASA were used for the numerical simulations. Neither code had been used in an application involving flow separation, sharp edges, and the aggregation of vorticity into small regions in the flow such as the two present applications demonstrate. The applications of the codes were largely successful, in that for both applications the numerical flow fields generally reproduced the gross flow features exhibited by experimental data.

The larger objective of demonstrating the suitability of using numerical simulations to augment experimental data was not achieved. The principal difficulty in both applications was mesh resolution. In the two-dimensional case, the mesh resolution was inadequate to determine the details of the boundary layer on the windward side, particularly near the edge where experimental data is very difficult to obtain. In the three-dimensional case, the problem was exacerbated by the requirement to store more information. In this case there were differences in the location of the peak suction pressure

on the wing and the vorticity distribution above the wing which were caused, at least in part, by mesh limitations. The objective is felt to be attractive and feasible, but considerable care must be taken in the numerical simulation to permit the mesh to capture and accurately represent important flow phenomena.

ACKNOWLEDGEMENTS

The help of Drs. Barrett Baldwin and Ching-Mao Hung in providing the two-dimensional Navier-Stokes code and running some of the cases is appreciated. Dr. Thomas Pulliam facilitated the running of the three-dimensional Navier-Stokes code on the ILLIAC IV before it was decommissioned. Finally the provision of computer time by Mr. Harvard Lomax for running these codes is greatly appreciated.

TABLE OF CONTENTS

	Page
1. INTRODUCTION.....	7
2. TWO-DIMENSIONAL CASE.....	10
2.1 Governing Equations.....	11
2.2 Numerical Algorithm.....	14
2.3 Checks on the Numerical Results.....	15
2.4 Comparison with Experimental Data.....	20
3. THREE-DIMENSIONAL PROBLEM.....	25
3.1 Body Geometry and Mesh Arrangement.....	26
3.2 Calculation Procedure.....	30
3.3 Results.....	31
3.4 Notes on the ILLIAC IV Calculation.....	35
3.5 Note on Mesh Generation.....	36
4. CONCLUDING REMARKS.....	37
REFERENCES.....	41
FIGURES 1 THROUGH 58.....	43

1. INTRODUCTION

The use of strakes, or leading edge extensions, on recent fighter type aircraft has been shown to improve greatly the high angle of attack aerodynamic characteristics of these aircraft. The beneficial effects stem from the formation of leading edge separation vortices on the highly swept strake and the subsequent interaction of these vortices with the flow over the wing to produce significant lift on the wing-strake combination at considerably higher angles of attack than is the case for the wing alone. These benefits have been derived primarily by cut and try methods in wind tunnel tests during aircraft development programs. Some studies of strake aerodynamics have been undertaken but the understanding of the fundamental fluid flow phenomena necessary to do a priori design of strake-wing-body combination does not exist. The purpose of this report is to describe a fundamental investigation undertaken to help fill this need. This investigation builds on the recent work that has been started on strake flows and on recent advances in numerical techniques for predicting fluid flows.

The present study is part of a larger program conducted by Nielsen Engineering & Research, Inc. (NEAR) for the Office of Naval Research under Contract N00014-78-C-0388. The first part of that work involved some two-dimensional tests in a wind tunnel at the NASA Ames Research Center as a first step in developing a method for predicting the rate at which vorticity is shed on a strake edge. That work is reported in reference 1. The current work reported herein involves numerical simulation of flows over surfaces with sharp edges. In addition to this numerical simulation work, the program was to include some wind tunnel tests on a highly swept wing to obtain three-dimensional

data which would be combined with the numerical and two-dimensional results to develop and evaluate an engineering prediction method for leading edge shedding rate.

One of the difficulties in using the three-dimensional data is the fact that the detailed flow field data acquisition is a time consuming process and the quantity of data that can be obtained in a reasonable tunnel entry is not as great as one would like. Also, it is very difficult to obtain boundary layer measurements, particularly near the edge where the flow separates, which is the region of greatest interest. Therefore in this study a recently developed computational technique for solving the Navier-Stokes equations is extended to treat flows with leading edge separation. These numerical results can then be used together with the experimental data to validate the theoretical flows and to define the flow field in greater detail, particularly in the windward side boundary layer and near the edge. The combined theoretical (numerical) and experimental flow fields can then be used to develop the engineering design methods.

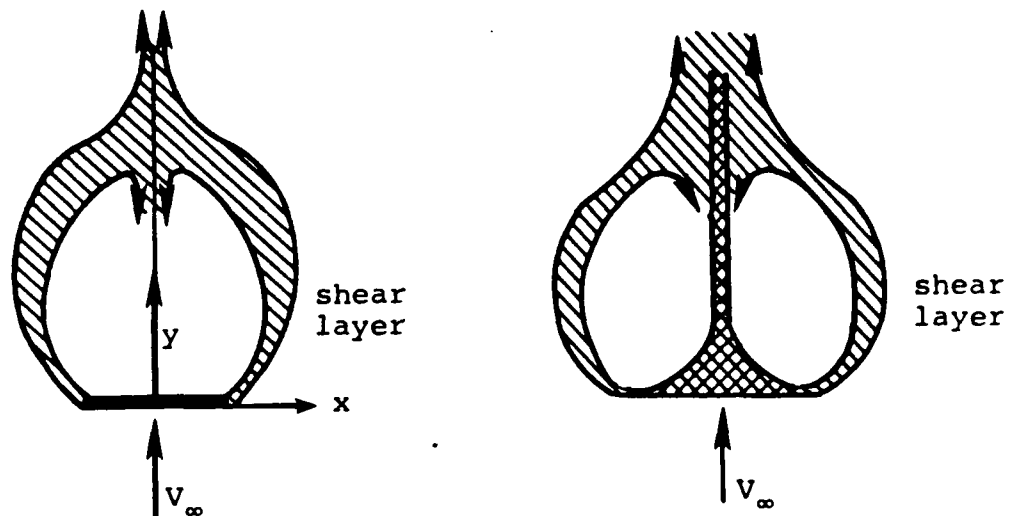
Thus the driving force for using a numerical simulation of the flow to supplement the experimental work is the relative difficulty of obtaining sufficient detailed flow characteristics from the latter. The kinds of details required for the development of an engineering prediction method are the vorticity in the subsequent separated vortex. Some of the existing Navier-Stokes computer codes, especially those developed by the Computational Fluid Dynamics (CFD) Branch at NASA Ames Research Center, are available to help define the flow in more detail. However, before embarking on a discussion of the numerical computations it is helpful to be more specific about the problem to be solved.

Modern strake configurations are curved, highly swept and blend into the wing to give a "double delta" appearance. To ensure a clean separation of the strake vortex, the strake leading edge is sharp. The free-stream Mach number at high angles of attack where strake vortex formation is important tends to be subsonic. Finally, the strake-wing combination will operate at high angles of attack, e.g., 30° . These characteristics are not common in the usual computational fluid dynamics problems. The only available three-dimensional code applicable to the problem is that of Lomax-Pulliam of the C₁ Branch at Ames Research Center. The code uses a fully implicit, delta form algorithm developed by Beam and Warming (ref. 2). The main conceptual difficulty of the code is that it solves a "thin layer" approximation to the Navier-Stokes equations. This approximation essentially consists of the retention only of those second derivatives normal to the surface. This allows treatment of separated flows.

The remainder of this report is concerned with the two problems studied. The first problem is a two-dimensional variant of the configuration examined experimentally in completed work for ONR (ref. 1). This work generated information on the required grid clustering, convergence rates, boundary conditions at the sharp edge, and the ability (and limitations) of the code to predict the flow. The two-dimensional experimental results of reference 1 are used for comparisons. The information gained during this phase of the investigation was then used in the solution of the more complex three-dimensional problem. Since the two problems are solved by different codes and are sufficiently dissimilar, they will be discussed in the two following sections separately.

2. TWO-DIMENSIONAL CASE

The problem of interest is the two-dimensional flow approaching a flat plate, as shown in the left sketch below. In the numerical simulation, the plate is treated as infinitely



thin and thus has sharp edges. For comparison purposes, data are available from reference 1 for a configuration shown in the right sketch. The plate has a sharp edge with a finite angle (a cusp) and a splitter plate extending well downstream to prevent alternate vortex shedding which can occur when the two sides of the flow can communicate with one another.

The data (ref. 1) which are available for comparison are static pressure distributions on the front face, two orthogonal velocity components in the flow field near the edge of the plate, and the location of the reattachment point at the rear of the separation bubble behind the plate. The velocity data can be used to calculate vorticity, rate of transport of vorticity, and circulation in specified contours in the flow field.

The experiment was conducted at Mach numbers of 0.25 and 0.5 at a Reynolds number based on the half face width in the range of $0.15 - 0.25 \times 10^6$. Thus the boundary layer on the front face approaching the edge is laminar.

2.1 Governing Equations

The equations governing the flow adjacent to the two-dimensional strake are the compressible Navier-Stokes equations. Since the Reynolds numbers are 0.5×10^6 or less, laminar flows only will be considered. The equations are in Cartesian coordinates

$$\frac{\partial}{\partial t} \vec{q} + \frac{\partial}{\partial x} \vec{E} + \frac{\partial}{\partial y} \vec{F} + \text{Re}^{-1} \left(\frac{\partial}{\partial x} \vec{R} + \frac{\partial}{\partial y} \vec{S} \right) \quad (1)$$

where

$$\vec{q} = \begin{bmatrix} \rho \\ \rho u \\ \rho v \\ e \end{bmatrix}, \quad \vec{E} = \begin{bmatrix} \rho \\ \rho u^2 + p \\ \rho u^5 \\ k(e+p)u \end{bmatrix}, \quad \vec{F} = \begin{bmatrix} \rho v \\ \rho uv \\ \rho v^2 + p \\ (e+p)v \end{bmatrix}, \quad \vec{R} = \begin{bmatrix} 0 \\ \tau_{xx} \\ \tau_{xy} \\ R_4 \end{bmatrix}, \quad \vec{S} = \begin{bmatrix} 0 \\ \tau_{xy} \\ \tau_{yy} \\ S_4 \end{bmatrix} \quad (2)$$

where

$$\tau_{xx} = (\lambda + 2\mu)u_x + \lambda v_y, \quad \tau_{xy} = \mu(u_y + v_x)$$

$$\tau_{yy} = (\lambda + 2\mu)v_y + \lambda u_x$$

$$R_4 = u\tau_{xy} + v\tau_{xy} + K \text{Pr}^{-1}(\gamma - 1)^{-1} \frac{\partial}{\partial x} (a^2)$$

$$S_4 = u\tau_{xy} + v\tau_{yy} + K \text{Pr}^{-1}(\gamma - 1)^{-1} \frac{\partial}{\partial y} (a^2)$$

and

$$p = (\gamma - 1) \left\{ e - \frac{1}{2} \rho (u^2 + v^2) \right\}$$

Here

- γ = specific heat ratio
- p = pressure
- a = sound speed
- Re = Reynolds number
- κ = thermal conductivity coefficient
- $\lambda = -(2/3)\mu$, by Stokes hypothesis
- μ = viscosity coefficient
- Pr = Prandtl number

The velocity components are nondimensionalized with respect to the free-stream sound speed a_∞ , the density ρ with respect to ρ_∞ , and the total energy e with respect to $\rho_\infty a_\infty^2$. The pressure is referenced with respect to $\gamma \rho_\infty$.

Since the two-dimensional strake is a thin flat plate, the Cartesian mesh is ideally suited for this case. However, clustering is necessary to adequately resolve the flow field near the plate. Thus two one-dimensional clustering functions are introduced,

$$\begin{aligned} \xi &= \xi(x), \\ \eta &= \eta(y), \\ \tau &= t. \end{aligned} \tag{3}$$

Under this transformation the governing equations become

$$\frac{\partial}{\partial \tau} \hat{Q} + \frac{\partial}{\partial \xi} \hat{E} + \frac{\partial}{\partial \eta} \hat{F} = Re^{-1} \left\{ \frac{\partial}{\partial \xi} y_n \vec{R} + \frac{\partial}{\partial \eta} x_\xi \vec{\delta} \right\} \tag{4}$$

where

$$\hat{q} = \vec{q}/J$$

$$\hat{E} = y_{\eta} \vec{E}$$

$$\hat{F} = x_{\xi} \vec{F}$$

and, for example,

$$\tau_{xx} = (\lambda + 2\mu) \frac{1}{x_{\xi}} u_{\xi} + \lambda \frac{1}{y_{\eta}} v_{\eta}$$

The transformation Jacobian is

$$J = 1/(x_{\xi} y_{\eta}) \quad (5)$$

The viscous terms are resolved only in a thin layer near the body due to lack of sufficient computer capacity. The viscous terms in y only are retained and those along ξ (along the strake surface) are dropped from the equations. Thus equation (4) is simplified to

$$\frac{\partial}{\partial \tau} \hat{q} + \frac{\partial}{\partial \xi} \hat{E} + \frac{\partial}{\partial \eta} \hat{F} = Re^{-1} \frac{\partial}{\partial \eta} (\hat{S})$$

where

$$\hat{S} = \frac{x_{\xi}}{y_{\eta}} \left[\begin{array}{l} 0 \\ \{(\mu) u_{\eta}\} \\ \{(4/3\mu) v_{\eta}\} \\ \{\kappa Pr^{-1}(\gamma - 1)^{-1} \frac{\partial}{\partial \eta} a^2 + (\mu/2) \frac{\partial}{\partial \eta} (u^2 + \frac{4}{3} v^2)\} \end{array} \right]$$

The nomenclature is shown in Figure 1.

The thin layer model is a useful simplification incorporated in the numerical codes used for this study (refs. 2 and 3).

For this two-dimensional case where ξ is normal to η , the viscous terms dropped are the same as those deleted in boundary layer theory. However, the normal momentum equation is retained in the thin layer model and the pressure can vary through the viscous layer. Therefore, the thin layer model does not incur the matching problem of boundary layer theory with the inviscid field and separation points are not singular points.

On the body surface [$\eta(y) = 0$ and $\xi(k) \leq 1$], the no slip condition requires

$$\begin{pmatrix} u \\ v \end{pmatrix} = \begin{pmatrix} 0 \\ 0 \end{pmatrix}$$

The pressure on the body surface is obtained from the normal momentum equation which for this configuration is the y-momentum equation.

The other four surfaces of the flow domain of Figure 1 are the symmetry plane, inflow and outflow planes, and the far field boundary. Symmetry conditions are imposed on the plane of symmetry. Free-stream conditions are imposed on the inflow plane and the far field boundary.

On the outflow plane zero gradients of all the flow variables are imposed.

2.2 Numerical Algorithm

The numerical algorithm used to solve the transformed equations and boundary conditions is the time-implicit numerical algorithm developed by Beam and Warming (ref. 2). Since the scheme and the code has been reported elsewhere (refs. 2 and 3) it will not be presented here again. The reader is referred to the cited references.

2.3 Checks on the Numerical Results

The numerical results were obtained on a thin flat plate of unit semispan normal to a flow with free-stream Mach number of 0.5. The Reynolds number based on free-stream velocity and semispan is 0.5×10^6 . The schematic of the flow geometry is shown in Figure 1. The inflow and outflow boundaries are at eight and twenty semispans upstream and downstream of the plate, respectively. The centerline is a plane of symmetry and the far field boundary is nine semispans from the centerline. The boundaries of this domain were determined by numerical experimentation so that the flow field in the neighborhood of the plate did not change with any further extensions of the boundaries.

Checks were made to evaluate accuracy, resolution, and convergence of the numerical solution. On the windward side of the plate the flow is essentially a stagnation-point-like flow which has an exact solution for incompressible flow. Figure 2 depicts the pressure coefficient at the windward stagnation point as a function of the initial mesh spacing normal to the plate. The theoretical pressure coefficient based on isentropic compression at $M_\infty = 0.5$ is $C_p = 1.0641$. Most of the results for this figure were obtained for a flow domain substantially smaller than the final domain. The outflow boundary was at eight semispans downstream of the plate for the first set of four runs, labelled points (a), (b), (c), and (d). The run for point (e) was with the outflow at twenty semispans downstream.

The first case, point (a), has a mesh spacing normal to the plate of 0.001 (all lengths are nondimensionalized with respect to the plate semispan). The mesh point distribution is 24 points on the windward side of the plate, 21 points on the leeward side, and 78 points parallel to the plate of which 41 points are on the plate equally spaced at $\Delta x = 0.025$. The

stagnation pressure is 0.62 which is about 40% lower than the isentropic pressure of 1.0641. For this case there are 8 points within the boundary layer on the windward side. Thus there are only 16 points between the inflow boundary and the viscous layer.

Increasing the number of points in the windward inviscid region at the expense of leeward side resolution gives the results of point (b). The stagnation pressure is up to 1.13 which compares favorably with the exact value. Further increases in the number of mesh points in the windward boundary layer (to 12) and the inviscid region (to 28 from 24) and properly resolving the leeward region gives the results of point (c). There is no further improvement.

Reducing the mesh spacing normal to the plate to 0.0002 (from 0.001) and increasing the number of boundary layer points to 15 gives the results shown by point (d). Here the pressure coefficient is 1.67, some 60% too high. With this small initial step size, the mesh must be rapidly expanded to reach the inviscid layer with approximately the same number of mesh points. The thin layer approximation used in the code is not correct for highly stretched meshes according to reference 4. The numerical results seem to verify the contentions of reference 4. Since it was not possible to change the thin layer approximation, it was decided to choose a stretching function and mesh spacing so that the thin layer approximation as used in the code did not introduce an appreciable error. Thus 30 points were selected upwind of the plate with 8 points in the boundary layer and an initial mesh spacing of 0.0005. The flow field on the leeside of the plate with the outflow boundary at 8 semispans downstream of the plate indicated that the separation bubble was not closed. Experimental data indicated that the separation bubble should extend approximately 8-10 semispans downstream of the plate. For that reason the outflow boundary

was extended to 20 semispans downstream. With this outflow boundary 48 points were needed to properly resolve the separated region and the shear layers. This mesh arrangement is the final one used for the numerical results and is shown as point (e) on Figure 2.

The grid network for this final configuration is shown in Figures 3 and 4. The former shows the entire grid and the latter shows the detailed mesh near the plate.

The convergence history of the numerical solution process is shown in Figure 5. The L^2 residual error drops more than 3 orders of magnitudes in about 4000 iterations. The time step was taken to be at $\Delta t = 0.01$ for the first 4000 iterations and then reduced to 0.001 for the last 2000 iterations. Since the algorithm is implicit, excessive dissipation occurs for large time steps. This has the tendency to smear the shear layers out too much. By reducing the time steps at the end of the run the shear layers can be "sharpened up" to yield more meaningful results.

The final check to verify the numerical results was made by comparing the boundary layer profiles on the windward side of the plate with the exact solution available for the incompressible Navier-Stokes equation for laminar flows (Rosenhead, ref. 5).

A brief description of the exact solution for a stagnation point flow is appropriate. A stagnation point flow on a flat plate is defined as a flow where the velocities external to the boundary are given by

$$u_e = kx \text{ and } v_e = -ky$$

where k is a constant dependent on the normalization used to nondimensionalize u_e , v_e , and y and the inviscid flow field.

The subscript 'e' refers to the flow external of the boundary layer. For an infinite flat plate u_e is independent of y . However, for a finite flat plate u_e attains a maximum at the edge of the boundary layer and then decays with increasing y . This is shown in the sketch in Figure 6. Therefore, for the finite flat plate u_{\max} must be linear in x for the flow to be a stagnation point flow. This linearity is shown in Figure 6 for the numerical solution. As shown the constant k is

$$k = 0.57 V_{\infty} / \ell$$

The exact solution (Rosenhead, ref. 5) is given in terms of a similarity solution, and the similarity variables are

$$\eta = \left(\frac{k}{\nu} \right)^{1/2} y = (0.57)^{1/2} \left(\frac{V_{\infty} \ell}{\nu} \right)^{1/2} \frac{y}{\ell}$$

$$u = kx f'(\eta) = 0.57 V_{\infty} \frac{x}{\ell} f'(\eta)$$

and

$$v = - (\nu k)^{1/2} f(\eta) = (0.57)^{1/2} V_{\infty} \left(\frac{\nu}{V_{\infty} \ell} \right)^{1/2} f(\eta)$$

The boundary layer profiles in terms of the similarity variables are shown in the next two figures. The numerical results agree fairly well with the exact solution, although it is apparent that the boundary layer should be resolved better with more mesh points. This can be seen by the difference between the numerical and exact solution in Figures 7 and 8. However, as indicated previously, increasing the resolution

in the boundary layer at the expense of the inviscid region causes errors in the stagnation pressure and reducing the normal step size near the plate introduces errors from the thin layer approximation. So the mesh point distribution as shown in Figures 3 and 4 was accepted as a workable compromise. However, as will be shown later the thicker numerical boundary layer on the windward side will effect the sharpness of the shear layer coming off the plate edge.

The velocity vector plot for the entire flow domain is shown in the several parts of Figure 9. The details near the plate are in Figure 10. As shown there is a large separated flow region behind the plate extending some 11.5 semispans downstream. Within this region is a small secondary separated flow region just inboard of the leeside of the plate edge. This can be seen better in Figures 11 and 12. The boundary layer profiles are also readily apparent in these two figures. Apparent in the former figure is the constant thickness of the boundary layer on the windward side of the plate. Also apparent in the latter figure is the shear layer coming off the plate edges.

The shear layers and separated flow region can be better observed in the stream function contour plots shown in figures 13, 14, and 15. These three figures depict the stream functions of the entire flow domain, the primary separated zone, and the secondary separated region, respectively. As can be seen the primary separated zone extends about 11.5 semispans downstream of the plate. The secondary bubble although small does extend over 20% of the semispan length and being near the tip of the plate has an influence on the shedding rate. Contour levels of Mach number, pressure, and density are shown in Figures 16, 17, and 18.

2.4 Comparison with Experimental Data

An extensive set of experiments was conducted on two-dimensional strakes as reported in reference 1. In this section the numerical results are compared with those experimental data and some theoretical data.

The first comparison, shown in Figure 19, is the static pressure along the windward side stagnation streamline. The data consists of measurements on the plate surface plus, in the $M = 0.25$ case, static pressures deduced from velocity measurements off the surface using the incompressible Bernoulli equation. The numerical results at $M_\infty = 0.5$ resemble the behavior of the experimental data for $M_\infty = 0.25$ and would be in relatively good agreement if the numerical results were displaced downward to cause the C_p on the plate to agree.

The static pressure on the face of the plate is shown in Figure 20. Except for the constant shift upward of the numerical results due to the differences of pressures at the stagnation point, the numerical and experimental data agree quite well. We note that the experimental pressure coefficient of 1.06 at the stagnation point agrees within 1% of the theoretical isentropic values of 1.0641. As discussed previously the numerical stagnation pressure depends on the boundary layer and the inviscid region resolution.

There are two principal differences between the numerical and experimental results. One is the sharpness of the shear layer. The lack of mesh resolution has the effect of spreading the numerical shear layer and thus making the velocity gradients less severe than is indicated by the data. Also the fact that the physical model has a cusp while the numerical model has zero plate thickness may have some influence on the differences in the gradients. The second difference is due to the

small secondary separation bubble near the leeward edge in the numerical solution which causes the v component to be everywhere downstream (positive), whereas the data show an upstream flow (negative v) in the recirculation region inside the shear layer. The effect of Reynolds number (0.15×10^6 for experiment and 0.5×10^6 for numerics) is not important. The rapid change of the axial gradients of the spanwise velocity at the same spanwise location is shown in Figure 23.

The spanwise variation of the velocity components at a station just behind the model face ($y \approx 0.2$) is given in Figures 24 and 25. The same trend is shown here, i.e. sharper experimental shear surfaces. The effect of the secondary separation bubble is apparent in the numerical results for $x \leq 1$. The velocity gradient variations at the same axial station are shown in Figures 26 and 27. The vorticity defined as

$$\zeta = \frac{\partial u}{\partial y} - \frac{\partial v}{\partial x}$$

is shown in Figure 28 as a function of span at the same axial location. Figure 29 gives corresponding vorticity transport rate ($v\zeta$) variation. Although all of the experimental gradients are higher than the numerical ones, the combination of the lower gradients and higher v produce vorticity transport rates similar to the data.

The next set of six figures (30 through 35) presents the same sequence of results as shown by the previous six figures except at an axial station $x \approx 1.1$ semispans downstream from the model face. The rapid decay of the spanwise velocity component (u) is evident. This decay is much more rapid for the numerical results. This is due not to any physics but to a lack of adequate mesh resolution. At this location of the shear layer ($y \approx 1.1$ and $x \approx 1.7$) the mesh is substantially

coarser than at the plate tip (see Figures 3 and 4). Since the numerical error and numerical dissipation is proportional to $O(\Delta x^2, \Delta y^2, \Delta x \Delta y)$ for the implicit scheme used in the code, the increasing coarseness rapidly increases the effective dissipation of the scheme and thus the shear layers will be spread much faster than dictated by the physical dissipation.

The lack of adequate resolution will affect the other properties of the shear layer as shown by Figures 36, 37, and 38. The first figure is the axial variation of the stream-wise vorticity transport rate, R , defined by

$$R = \int_0^{\infty} v \zeta \, dx$$

Shown are two sets of experimental data. One set is based on the above formula and the other set is based on a thin shear layer approximation where

$$\begin{aligned} \zeta &= \frac{\partial u}{\partial y} - \frac{\partial v}{\partial x} \\ &\approx - \frac{dv}{dx} \end{aligned}$$

$$R = - \int_i^o v \frac{\partial v}{\partial x} \, dx \approx - \int_i^o d\left(\frac{v^2}{2}\right) = - \frac{v_o^2 - v_c^2}{2}$$

and o and i represent the outer and inner edges of the shear layer, respectively. The vorticity transport rate was computed from the exact formula by the trapezoidal rule for the numerical results. As can be seen from Figure 36, the numerical vorticity transport rate is low compared to the experimental results.

Also shown on this figure are the numerical vorticity transport rates at a point where the shear layer is just coming

off the plate edge. In this case the transport rate is

$$R = - \int_{-\delta\ell}^{\delta w} u \zeta dy$$

$$= - \int_{-\infty}^{\infty} \left(\frac{u^2}{2} \right) dy \approx - \left(\frac{u_{\delta w}^2}{2} - \frac{u_{\delta\ell}^2}{2} \right)$$

where $u_{\delta w}$ is the spanwise velocity component at the boundary layer edge on the windward side of the plate tip and $u_{\delta\ell}$ is the corresponding velocity on the lee side of the plate tip. The calculated vorticity transport rate in the shear layer and the boundary layer at the tip agree fairly well. The differences between the numerical calculation and the experimental data are the same no matter how they are computed.

The effect of decreasing numerical resolution and thus the faster spreading rate of the shear layer is quite evident in this figure and the following two figures. Figure 37 depicts the integrated vorticity (γ) along various axial stations. The integrated vorticity is defined as

$$\gamma = \int_0^{\infty} \zeta dx$$

which becomes with the thin shear layer approximation

$$\gamma \approx v_i - v_o$$

Again the lower values for the numerical results are evident.

The circulation, Γ , can be computed around rectangular contours at many y locations, each contour extending spanwise from the symmetry plane to the far field boundary and having a streamwise length of 10% of the plate semispan. This comparison is shown in Figure 38. The circulation is essentially zero upstream of the plate face, a rapid increase occurs just after the face to a final peak at about 1.5 semispans downstream of the face and then a gradual decay. As expected the numerical results are lower than the experimental data.

Another difference between the numerical results and the experiment is the lateral extent of the primary separation bubble. This can be observed by comparing figures 39 and 40 with Figure 23(b) of reference 1. Shown in these figures are the axial velocity profiles at various axial stations behind the model face. If $v = 0$ is used as a measure of the size of the primary separated flow region, then the experiment indicated for $y = 2.0$ that $v = 0$ at $x \approx 1.8$ whereas for the computations $x \approx 1.0$. The proper measure of the size of the separated region is the dividing streamline (the streamline emanating from the tip of the plate) as shown in Figure 15 for the numerical computations. Unfortunately this is not available for the experiment. It can be approximated, however, from Figure 23(b) of reference 1 to be at $x = 2.1$ for $y = 2.0$. The numerical dividing streamline is at $x = 1.6$ (Fig. 40). Thus the spanwise extent of the primary separated region is much smaller for the numerical results.

There are at least two possible reasons for this discrepancy. One is the model configuration. The experimental model has a finite thickness plate, finite tip angle, and a splitter plate whereas the numerical configuration consists of a thin flat plate with a plane of symmetry having no boundary layer instead of the splitter plate with its own boundary layer. These differences in the model geometry can be expected to

enlarge the separated region. The second reason is the difference in the secondary separation regions. In the numerical simulation, there is a secondary separation on the downstream side of the plate near its edge, as shown on the left sketch. The experiment has a secondary separation region



on the splitter plate as shown on the right. There was also a difference in channel half-width (9 for the computation vs. 12 for the experiment) although this should have very little effect on the problem.

While the numerical results show good qualitative agreement with the experiment, the mesh points must be better distributed or the number must be increased to properly resolve the shear layers. If the shear layers are not sufficiently resolved then little accuracy can be expected from the numerical computations about the vorticity shedding (transport) rates or the circulation. While the general features of the flow field are fairly easy and inexpensive to compute, accurate details of the field are much more expensive unless flow adaptive meshes are incorporated into the numerical computations.

3.0 THREE-DIMENSIONAL PROBLEM

A calculation of the flow field about a $75^\circ/63^\circ$ double-delta wing was performed on the CDC 7600 computer using the version AIR3DP5 of the code AIR3D developed by Pulliam and Steger and described in reference 6. The code solves the three-dimensional "thin layer" Navier-Stokes equations by an implicit approximate factorization finite-difference algorithm. The body surface must be topologically similar to a hemisphere cylinder.

As in the two-dimensional code, the thin layer approximation means that the only second derivatives which are retained in the viscous terms are those normal to the body. This is necessitated anyway because the available computer storage only allows us to cluster the grid in one direction, namely a "boundary-layer like" coordinate ζ normal to the body.

The wing configuration used in the calculations was that selected originally for the three-dimensional wind tunnel test. The sweep of the forward part of the wing (75°) is essentially that of an aspect ratio 1 delta wing, on which Hummel (refs. 7 and 8) has taken surface pressure and flow visualization data which could be used to evaluate the computed results forward of the break in sweep. The sweep of the aft position of the wing was selected first to be not so different than that of the forward part that the leading edge vortex from the forward part would "tear off" at the break in sweep and second to be close to a double-delta wing for which some data exist. Wentz (refs. 9 and 10) has taken data on a number of double-delta wings, one of which has sweeps of 75° and 62° . The data consists of forces and moments, oil flow, surface pressures, and velocities above the wing. This configuration is sufficiently close to the $75^\circ/63^\circ$ wing to permit evaluation of the numerical results.

3.1 Body Geometry and Mesh Arrangement

The computational body is pictured in orthographic projection in Figure 41. The planform is a double-delta shape with sweep angles of 75° and 63° , with the break in sweep occurring at midchord ($x = 0.5$). Because of coding requirements, the body is extended aft of the root chord position at constant semispan (the "sting"), thus implying a second break in sweep to 90° at the tail plane $x = 1.0$. All dimensions are normalized to root chord.

The cross sections are ellipses chosen so that the vertical axis is .01 root chord and the horizontal axis is equal to the

semispan. This sectional shape allows the use of orthogonal elliptic coordinates in the crossflow planes, as can be seen in the grid plots (Fig. 42). Since the vertical axis is constant and the semispan varies, the axis ratio ϵ of the ellipses is not constant but varies from more than one near the nose to about .013 at and aft of $x=1$. Hence, the configuration is not conical.

In order to avoid a coordinate singularity at the nose, the body was truncated at $x = .01$ and a prolate spheroidal "cap" was appended thereto.

Physical coordinates (x,y,z) are chosen so that x increases from zero along the chord line going aft, y increase toward starboard and z increases upward. Computational coordinates (ξ,η,ζ) are chosen so that $\zeta = 0$ is the body surface. Except on the cap, ξ measures the axial distance and is equal to x . η is an azimuthal angle and ζ increases radially outward. Both systems of coordinates are right-handed. On the cap, coordinate ξ measures the polar angle.

Let $b(\xi)$, $\xi > .01$, be the semispan as a function of radius. Thus,

$$b(\xi) = \begin{cases} \xi \tan 15^\circ, & .01 < \xi < 0.5 \\ 0.5 \tan 15^\circ + (\xi - 0.5) \tan 27^\circ, & 0.5 < \xi < 1 \\ 0.5 (\tan 15^\circ + \tan 27^\circ), & 1.0 < \xi \end{cases}$$

Let $b_{\min} = .01 \tan 15^\circ$ and $b_{\max} = .5 (\tan 15^\circ + \tan 27^\circ)$. Then, the transformation between physical and computational coordinates is as follows:

On the cap:

$$x = .01 - \sqrt{\zeta^2 + b_{\min}^2} \cos \eta \cos \xi$$

$$y = \sqrt{\zeta^2 + b_{\min}^2} \cos \eta \sin \xi$$

$$z = \zeta \sin \eta \sin \xi$$

On the wing:

$$x = \zeta$$

$$y = \sqrt{\zeta^2 + [b(\xi)]^2} \cos \eta$$

$$z = \zeta \sin \eta$$

On the sting:

$$x = \zeta$$

$$y = \sqrt{\zeta^2 + b_{\max}^2} \cos \eta$$

$$z = \zeta \sin \eta$$

The computation takes place in a cubical domain pictured in Figure 43 (see also Fig. 2(b) of ref. 1). The computational coordinates are discretized so that

$$\xi = \xi(J), J = 1, 30$$

$$\eta = \eta(L), L = 1, 30$$

$$\zeta = \zeta(K), K = 1, 24$$

The cross flow planes are represented by $J = \text{constant}$ computational planes, and are tabulated in Table 1. The nose is at $J = 8$ and the sting begins at $J = 24$. There is a singular line at $J = K = 1$ corresponding to the pole of the cap. This singularity is avoided in the finite-difference version of the problem because the fluxes in the ξ - and ζ - directions vanish identically on this line (ref. 6).

The mesh is clustered in the axial direction near the nose, break in sweep, and root chord, and in the circumferential

TABLE I. 75°/63° DOUBLE DELTA WING CALCULATION

Mesh Crossflow Planes

Index J	Chord z(J)	Semispan b(J)	Ellipse Axis Ratio ϵ	Wentz Coordinate $X = \left(\frac{1-z}{b_{\max}} \right)$
1	} Nose region "cap"			
2				
3				
4				
5				
6				
7				
8	.0100	.0026	1.92	2.547
9	.0341	.0091	.55	2.485
10	.0824	.0220	.227	2.360
11	.1579	.0423	.118	2.166
12*	.2496	.0669	.075	1.930
13	.3408	.0913	.055	1.696
14	.4162	.1115	.045	1.502
15	.4683	.1255	.040	1.368
-----	.50	-----Break in sweep -----		
16*	.5025	.1353	.037	1.280
17	.5384	.1535	.0326	1.187
18	.5936	.1816	.0275	1.045
19	.6712	.2212	.0226	.846
20*	.7632	.2681	.0187	.609
21	.8543	.3145	.0159	.375
22	.9287	.3524	.0142	.183
23	.9761	.3765	.0133	.061
24*	1.00	.38874	.0129	0
25	1.031	↓	↓	-.080
26	1.123			-.316
27	1.389			-1.001
28	2.166			-2.999
29	4.425			-8.811
30	11.000			-25.724

*Indicates plots

direction near about 80% semispan on the leeward side where we expected that the primary leading edge separation vortex would form. In the circumferential direction, one extra point beyond the plane of symmetry at each boundary is required by the code for implementing the boundary conditions. The radial direction is clustered so that 8 of the 24 points lie within .15 chordlengths of the body surface. The grid is exponentially stretched out to an outer boundary 10 chord-lengths away. Figures 42 and 44 give typical views of the grid.

The grid generation routine calculates $x(J,K,L)$, $y(J,K,L)$, $z(J,K,L)$ for each of the 21,600 grid points and stores these on tape for use in the calculation itself and the graphics display package.

3.2 Calculation Procedure

The free-stream Mach number of the calculation was 0.5. This was large enough to let the calculation converge but small enough to prevent the development of a large supersonic region near the edges. The angle of attack was 15° , so the Mach number in the crossflow plane was 0.13. The Reynolds number was 0.5×10^6 based on root chord, and a laminar boundary layer was selected. The Prandtl number was 0.72 and the free-stream temperature was 500°K .

The calculations were run on a CDC 7600 computer at Ames Research Center. Two smoothing parameters were used in AIR3D, as described in reference 6. The explicit smoothing parameter was set at 0.1 and the implicit parameter was set at 1.0, based on previous experience with the code.

Following past experience with the code, the boundary conditions were entered during the first 30 iterations, and the code was run at a timestep of 2×10^{-4} , corresponding to a Courant number of about 4 for 500 iterations. The timestep

was increased to 5×10^{-4} (CFL ≈ 10) after 100 iterations and to 10×10^{-4} (CFL ≈ 20) after 1400 iterations. The program was run for 9500 iterations, until the residual was down by about a factor of 30. The CPU time per iteration was about 17 seconds. Thus, even on this relatively coarse grid, the calculation required more than 80 hours of CPU time. The convergence history is shown in Figure 45.

3.3 Results

The flow field (i.e., values of the density, three components of the velocity, and the internal energy at every grid point) was written into a disc file for analysis and graphic display.

The closest experimental comparison to this calculation is the work of Wentz and McMahon (refs. 9 and 10) who used a $75^\circ/62^\circ$ double delta pictured in Figure 46. There are two primary differences between the experiment and the calculation. The experimental model has a fuselage attached, and has a sharp trailing edge, while the computational model has neither. Also, the experiment was run at $M_\infty \approx .16$ while the calculation was at $M_\infty = .50$ (the latter was necessitated in order to obtain convergence within a reasonable time). Wentz's most complete data were obtained at angles of attack of 10° or 20° , so the comparisons at 15° are somewhat limited.

Plots of the flow field were obtained for every crossflow plane aft of the nose. Four sets of these are reproduced here. Figures 47(a)-(h) show the flow field at about one-quarter root chord, halfway between the nose and the break in sweep. Figures 48(a)-(h) show the flow field just aft of the break in sweep at mid-chord. Figures 49(a)-(h) show the flow field at three-quarters chord and Figures 50(a)-(h) show the flow field at the root chord where the sting begins.

For each of these chordwise stations are plotted (a) the mesh, (b) an overall view of the crossflow velocity field, (c) a closeup of the velocity field near the tip, (d) a plot of C_p along the wing surface, and (e) contours of the crossflow Mach number, with 20 equally spaced levels between maximum and minimum Mach number, $\Delta M \approx .05$. Figure (f) of each set shows the vorticity contours, with levels exponentially concentrated near the maximum value. In all cases the concentration is very near the tip. Figure (g) of each set shows contours of density and Figure (h) of each set shows contours of total pressure, with equal increments between contours.

The most important qualitative features of the flow can be seen in the velocity vector plots. One can see the primary vortex system forming at about $x = .25$. The center of this vorticity moves inboard until at the tail plane, its center is at about $y = .22$ and $z = .12$, or, in terms of semispan, $y/b \approx .6$ and $z/b \approx .3$. This may be compared with the simplified theory of Brown and Michael (ref. 4) which predicts a location $y/b = .88$, $z/b = .14$. We can see that the onset of primary separation occurs at about $x = .25$ and that the separation line reaches the plane of symmetry at about $x = .5$. One can see the development of secondary separation near the tip in Figure 50(c), but the mesh is too coarse to resolve it. In the same figure, note the typical boundary layer profile on the lower surface. This feature is qualitatively correct, but the profile should have a much smaller thickness. This is again due to the inadequacy of the grid, even though it is the largest that can be run on the CDC 7600.

Looking at the pressure contours, we find that the C_p distribution is very sharply peaked near the tip, unlike the experimental (i.e., ref. 8 for a delta wing and ref. 9 for a double delta) results which show milder peaks at about 70%

semispan. Indeed, there is a small region where the crossflow is supersonic, even though the crossflow freestream Mach number is about 0.13. Perhaps this is due in part to the unevenness of the mesh in the region and a large concentration of grid points near the tip.

The other plots are more or less self-explanatory. Contours of the pressure coefficient on the wing surface are presented in Figure 51. Wentz's experimental result is presented in Figure 52. Several features are different. In the calculation, we find a minimum C_p of -2.45, which corresponds to a slightly supersonic Mach number. Wentz's minimum C_p is about -1.95. Part of this is due to compressibility. Applying the Prandtl-Glauert correction (the effect of compressibility to first order - see ref. 11) yields the following comparison: Wentz's value (at $M_\infty = .16$) is corrected to

$$[C_p (1-M_\infty^2)^{1/2}]_{\min} = - 1.93$$

and our minimum (at $M_\infty = .5$) is corrected to

$$[C_p (1-M_\infty^2)^{1/2}]_{\min} = - 2.12$$

The predicted vortex lift is more concentrated and further outboard (near 95% semispan) than the experimental result, which shows the locus of minimum C_p at roughly 70% of the semispan.

On the computational wing there is not as much lift on the portion near the nose. This is due, at least in part, to the absence of a forebody which for the Wentz results causes additional upwash near the wing leading edge where the span is the same order as the body radius.

The total circulation, nondimensionalized as $\tilde{\Gamma} = \Gamma / 2V_{\infty} b_{\max}$ to compare with Wentz's measurements, was calculated over half the wing by performing the contour integration $\oint \vec{V} \cdot d\vec{\ell}$ over the contours shown in Figure 53. Contour C_1 encloses the entire flow field bounded by the plane of symmetry. Thus the contribution on the wing surfaces vanishes due to the boundary condition $v = 0$. Contour C_v encloses the upper quadrant of the flow field but excludes the first three grid points from the wing surface (i.e. the "boundary layer"). This is a closer approximation to the contour Wentz used, since he could not obtain measurements in the boundary layer. The circulation is presented as a function of axial distance in Figure 54. Theoretical values according to Jones (linear theory, ref. 3) and Brown and Michael (concentrated vortex core, ref. 12) are shown for $\alpha = 15^\circ$. Wentz's experimental results for $\alpha = 20^\circ$ and his contour are shown in Figure 55. In both cases the results lie between the two theoretical curves. The falloff in circulation over the aft half of the wing is due to the presence of the trailing edge in the experiment and the "sting" in the calculation. A more recent experiment by Sforza and Smorto (refs. 14-15) also has shown a value for the circulation which lies between the Jones and Brown-Michael theories.

Integrating the pressure coefficient over the body surface, we find a normal force coefficient

$$C_N = \frac{N}{qS} = 0.7738$$

and a lift coefficient $C_L = C_N \cos(15^\circ) = 0.747$. Here S is the planform area and $q = \frac{1}{2} \rho U^2$ is the dynamic pressure. Normalized by aspect ratio we obtain $(C_L/AR) = 0.420$ for an aspect ratio of 1.84. Wentz (refs. 9 and 10) obtains the values $C_L = 0.70$ and $(C_L/AR) = 0.43$, respectively, his aspect ratio being 1.61. While the agreement is very good, it is difficult to interpret

this result, in that the nonlinear portion of the lift can be considered the product of the vortex strength and span, which could both be somewhat in error while still producing the correct overall lift.

Again by integration we obtain a center of pressure of $x_{cp} = 0.77$ compared to Wentz's $x_{cp} = 0.58$. That is to say, the calculation shows rather more lift on the aft sections. This is most likely attributable to the presence of the sting on the wing, which maintains the lift near the "trailing edge", as can be seen from the C_p contour plots.

3.4 Notes on the ILLIAC IV Calculation

The plan in this work was to run the AIR3D code on the CDC 7600 to evaluate its ability to treat slender thin wings and if successful then move to the ILLIAC IV where a finer mesh could be used. The calculation performed on the CDC 7600, while generally successful, did not permit a sufficient number of grid points to capture the boundary layer. A typical boundary layer velocity profile occurs on the windward side [Fig. 50(c)], but it is "stretched out" to about ten times what one would normally expect for a Reynolds number of 500,000. Clearly, it was necessary to calculate on a finer mesh. Thus, the calculation was programmed for the ILLIAC IV computer.

Fortunately, the program AIR3D has been implemented on the ILLIAC IV and run for simple geometries (ref. 17). The capacity of the ILLIAC IV in 64-bit mode is 80 axial \times 56 circumferential \times 48 radial grid points, a total of 215,040 or about ten times what could be done on the CDC 7600. Simpler geometries, like the hemisphere cylinder, has been run before, but this new calculation would be more complicated, and on a slightly larger mesh than had been run before.

The unique nature of the ILLIAC hardware requires equally unique data structures. Thus, there was a time-consuming process of generating the mesh, and formatting it and the data onto files which could be used by the ILLIAC.

A new problem was chosen, with a somewhat simpler geometry, in order to concentrate on modeling the leading edge vortex to see if better agreement could be obtained on spanwise location and surface pressure distribution. The problem selected was a simple delta wing of unit aspect ratio, at 20.5° angle of attack, such as had been investigated by Hummel (refs. 7 and 8).

It was clear from experience with the CDC 7600 calculation that the orthogonal mesh used there inhibited convergence. Thus a new, clustered mesh, nonorthogonal in the crossflow planes, was generated for the new calculation.

The new mesh was written onto tape and the code was assembled on tapes for the ILLIAC IV computer. The code was run for 100 iterations, long enough to make sure it was running properly and to impose the boundary conditions. The CPU time was about 72 seconds per iteration. Unfortunately, the ILLIAC IV was decommissioned before further iterations could be run, and no further work was possible.

The code AIR3D is being rewritten for use on the CRAY-1 but it will not be possible to run the code on the CRAY until the size of the memory is extended to 8 million words, which will not occur until 1983.

3.5 Note on Mesh Generation

It was noted during the work that the largest permissible timestep for a given Courant number was controlled by the mesh cell size near the leading edge. This is illustrated in the closeup of the mesh, Figure 56. Consider a crossflow plane where the semispan is b , and the minimum radius at the edge

has the value σ . Then the $\zeta = \text{constant}$ surfaces, those surfaces parallel to the wing surface, are given by the ellipses.

$$z^b = [(y + \sigma)^2 + b^2]^{1/2}$$

Differentiating, we find

$$\frac{dy}{dz} = \frac{z}{\sqrt{z^2 + b^2}}$$

For small z , we have $dy \approx \frac{z}{b} (dz)$. Since z/b is of the order 0.01 near the $z = 1$ plane, this compression of the $\zeta = \text{const.}$ surfaces near the edge slowed down the maximum timestep by at least an order of magnitude.

A remedy for this, which was checked in working out the mesh for the ILLIAC IV calculation was to use the non-orthogonal mesh

$$z = [(y + \sigma)^n + b^n]^{1/n}$$

which is orthogonal for $n = 2$. For $n = 1$, there were problems with skewness of the mesh; $n = 1.5$ provided a good compromise, and allowed a tenfold larger time-step for a given Courant number. The visible improvement over Figure 56 is seen in Figure 57, where the same region of the edge is shown in the new mesh.

4. CONCLUDING REMARKS

The objective of this portion of the strake vorticity shedding work was to demonstrate that computational solutions could be used to enhance one's knowledge of an experimentally determined flow, particularly for regions in the flow where

measurements are very difficult to obtain. In order to use a computational solution in this manner, the important features of the computational solution must agree well with those of the experiment. In the two cases considered here, the flow is dominated by shear layers separating from an edge which depends strongly on the boundary layer characteristics of the flow approaching the edge. Thus, it is important to be able to adequately resolve and describe in the computation the boundary layers on the surfaces approaching the edge and the large flow property gradients in the shear layer adjacent to the edge.

The two cases considered here were a two-dimensional flow normal to a thin flat plate and a three-dimensional flow over a thin slender wing at moderate angle of attack. In spite of the fact that the two cases are conceptually simple, there is little flow field data available. In the two-dimensional case, the data consist of laser velocimeter measurements taken as an earlier part of this study and data taken 6 decades ago with a hot wire anemometer. In the three-dimensional case, there are flow field data above the wing and pressures on the wing, but no data near the edge to define the shear layer and vorticity shedding rate.

It is important to note that when the present investigation was initiated, neither the two-dimensional nor the three-dimensional computer code had been used to compute flows with substantial separation. Hence the present work can be viewed as a preliminary study of the ability of these computer codes to capture and represent the various separated flow phenomena.

In both cases, the important flow features of the computational flow agreed qualitatively with those shown by the data. Specifically, the computational boundary layers on the windward and leeward surfaces near the edge generated vorticity

which appears in a shear layer leaving the edge. In the two-dimensional case, the primary separation bubble behind the plate had nearly the same axial and lateral extent as shown by the experiment. In the three-dimensional case, the computational vorticity appeared in the flow above the wing, although it did not tend to roll up into a concentrated vortex as the experiment shows [compare Figs. 48(b) and 58].

In both cases, computational mesh size and arrangement limitations are an important factor in the comparisons with data. It was not possible to keep enough mesh points in the boundary layer and still define well enough the flow away from the surface. This was particularly so for the three-dimensional case, which had a much more severe storage problem for the computer. This is felt to be a major limitation in achieving the objective of using computational flow fields to augment experimental measurements.

In both cases, the computational problem was slightly, but probably importantly, different than the experimental problem. In the two-dimensional case, the experimental flat plate normal to the flow was required to have a splitter plate downstream to enforce steady flow and a plane of symmetry. Thus, the boundary condition on the plane of symmetry in the experiment was a no-slip zero-velocity condition yielding a forward moving boundary layer which caused secondary separation to occur on the splitter plate just downstream of the plate. The computation had a plane of symmetry condition only, with a no-slip condition only on the back face of the plate, which yielded secondary separation on the back face of the plate near the edge. These differences were probably responsible for some of the differences in the vorticity shedding rate and location of the shear layer.

In the three-dimensional case, the forward portion of the wing was not thin because of a limitation in the "body" geometry the code could handle. Also the code could not treat a trailing edge. Both of these factors would affect the load distribution, as compared to the experiment and possibly the general character of the vorticity-dominated region above the wing.

In the three-dimensional case, there was also a qualitative difference between the computational and experimental flow. The computational suction peak was further outboard than the measured one, and the computational vorticity appears to be more diffuse above the wing than the data would indicate. The extent to which these differences are dependent on the mesh size and arrangement and the wing geometry model is not clear.

In the three-dimensional calculation, it became clear that the design of the coordinate mesh has a significant effect on the convergence time of the solution, as well as on the accuracy with which the features of the flow can be predicted with a fixed mesh (in which the mesh points do not move as the solution progresses); one must pre-cluster the points where the flow features are expected to appear. Here, we clustered the points near the vortex loci shown by the data, but the code caused the vorticity to occur at a different spanwise location. In an adaptive mesh algorithm, the points are allowed to move in such a manner as to "capture" the flow phenomena. Although the storage problem is not eased, an adaptive mesh algorithm should provide better definition of the flow, and thus an improved solution for a given amount of computer time.

In summary, it appears that for two dimensional flows with separation, there is probably a reasonable expectation for using computational solutions for augmenting experimental ones, provided care is exercised in modeling the flow and generating the mesh. For three-dimensional flows, the problem appears

more difficult because of the mesh requirements and the additional computer storage due to the third dimension and would probably require the development of an adaptive mesh algorithm.

REFERENCES

1. Spangler, S. B., Schwind, R. G., and Owen, K.: Experimental Results on Vorticity Shedding at the Edge of a Flat Plate in Two-Dimensional Flow. NEAR TR-224, Sept. 1980.
2. Beam, R. M. and Warming, R. F.: An Implicit Factored Scheme for the Compressible Navier-Stokes Equations. AIAA J., Vol. 16, No. 4, 1978.
3. Steger, J. L.: Implicit Finite Difference Simulation of Flow about Arbitrary Two-Dimensional Geometries. AIAA J., Vol. 16, No. 7, 1978.
4. Mehta, U. and Lomax, H.: Numerical Prediction Methods. In Transonic Aerodynamics, ed. D. Nixon, Progress in Aeronautics and Astronautics, Vol. 81, 1982 (to be published).
5. Rosenhead, L.: Laminar Boundary Layers. Clarendon Press, Oxford, 1963.
6. Pulliam, T. H. and Steger, J. L.: Implicit Finite Difference Simulations of Three-Dimensional Compressible Flow. AIAA J., Vol. 18, No. 2, Feb. 1980, pp. 159-167.
7. Hummel, D.: Zer Unstromung sharfkantiger schlanker Deltaflugel bei gro en Anstellwinkeln. Z. Flugwiss., 15 (1967) Heft 10, pp. 376-385.
8. Hummel, D.: On the Vortex Formation over a Slender Wing at Large Angles of Incidence. AGARD CP-247, Paper #15, 1978 (Sandefjord, Norway).
9. Wentz, W. H., Jr. and McMahon, M. C.: An Experimental Investigation of the Flow Fields about Delta and Double-Delta Wings at Low Speeds. Wichita State University (Kansas), Aeronautical Report 65-2, Aug. 1965.
10. Wentz, W. H., Jr. and McMahon, M. C.: Further Experimental Investigations of Delta and Double-Delta Wing Flow Fields at Low Speeds. NASA CR-714, Feb. 1967.

11. Liepmann, H. W. and Roshko, A.: Elements of Gasdynamics. John Wiley and Sons, New York, 1957.
12. Brown, C. E. and Michael, W. H., Jr.: On Slender Delta Wings with Leading-Edge Separation. NACA Tech. Note 3430, Apr. 1955.
13. Jones, R. T.: Properties of Low-Aspect-Ratio Pointed Wings at Speeds Below and Above the Speed of Sound. NACA Rept. No. 835, May 1945.
14. Sforza, P. M. and Smorto, M. J.: Streamwise Development of the Flow over a Delta. AIAA J., Vol. 19, No. 7, July 1981, pp. 833-834.
15. Lamar, J. E.: Comment on "Streamline [sic] Development of the Flow over a Delta Wing." AIAA J., Vol. 20, No. 4, April 1982, p. 576.
16. Sforza, P. M. and Smorto, M. J.: Reply by the authors to J. E. Lamar, AIAA J., Vol. 20, No. 4, Apr. 1982, p. 576.
17. Pulliam, T. H. and Lomax, H.: Simulation of Three-Dimensional Compressible Viscous Flow on the ILLIAC IV Computer. AIAA Paper 79-0206, Jan. 1979.

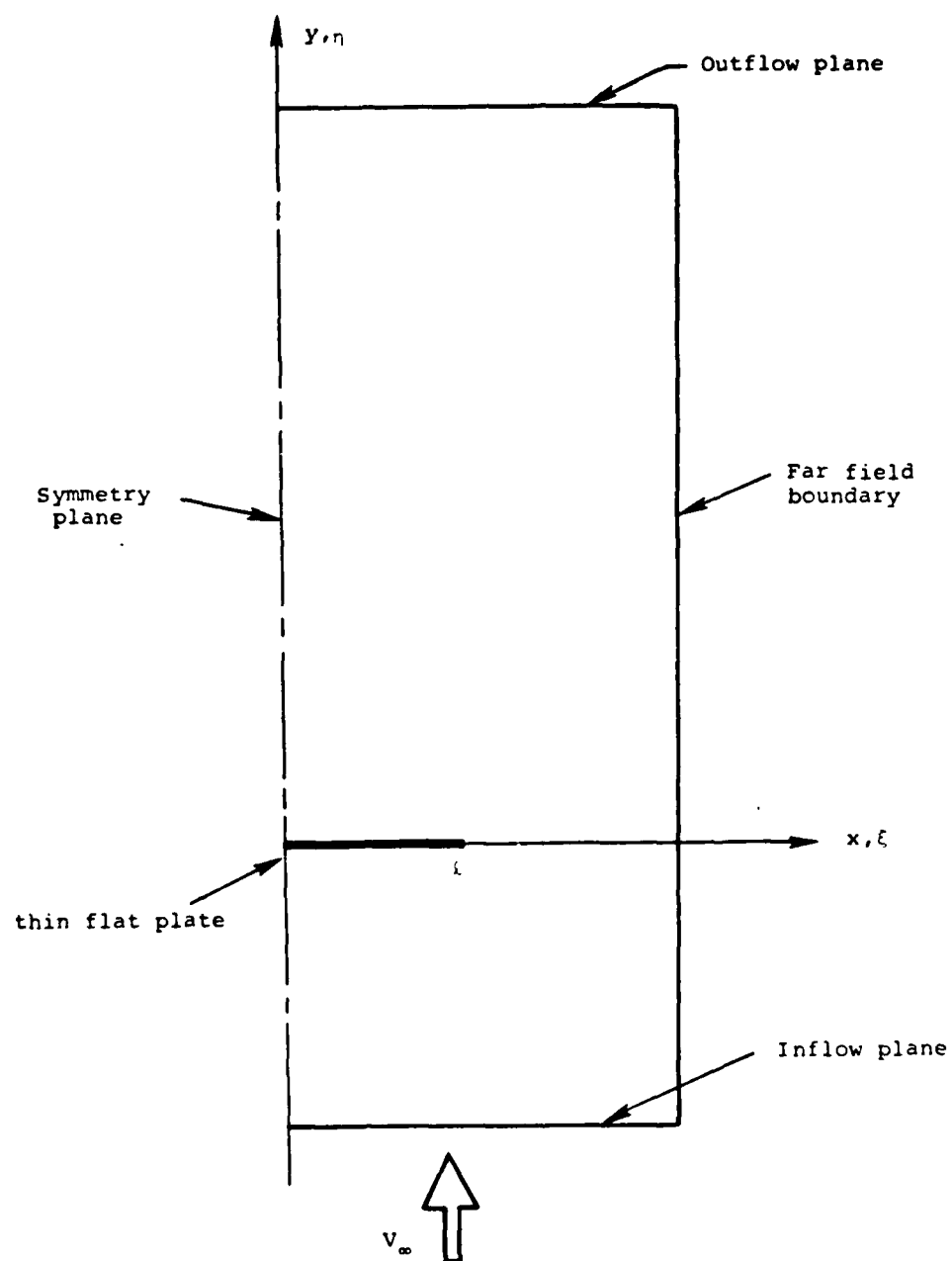


Figure 1. Two-dimensional flow domain
semispan length $l = 1$.

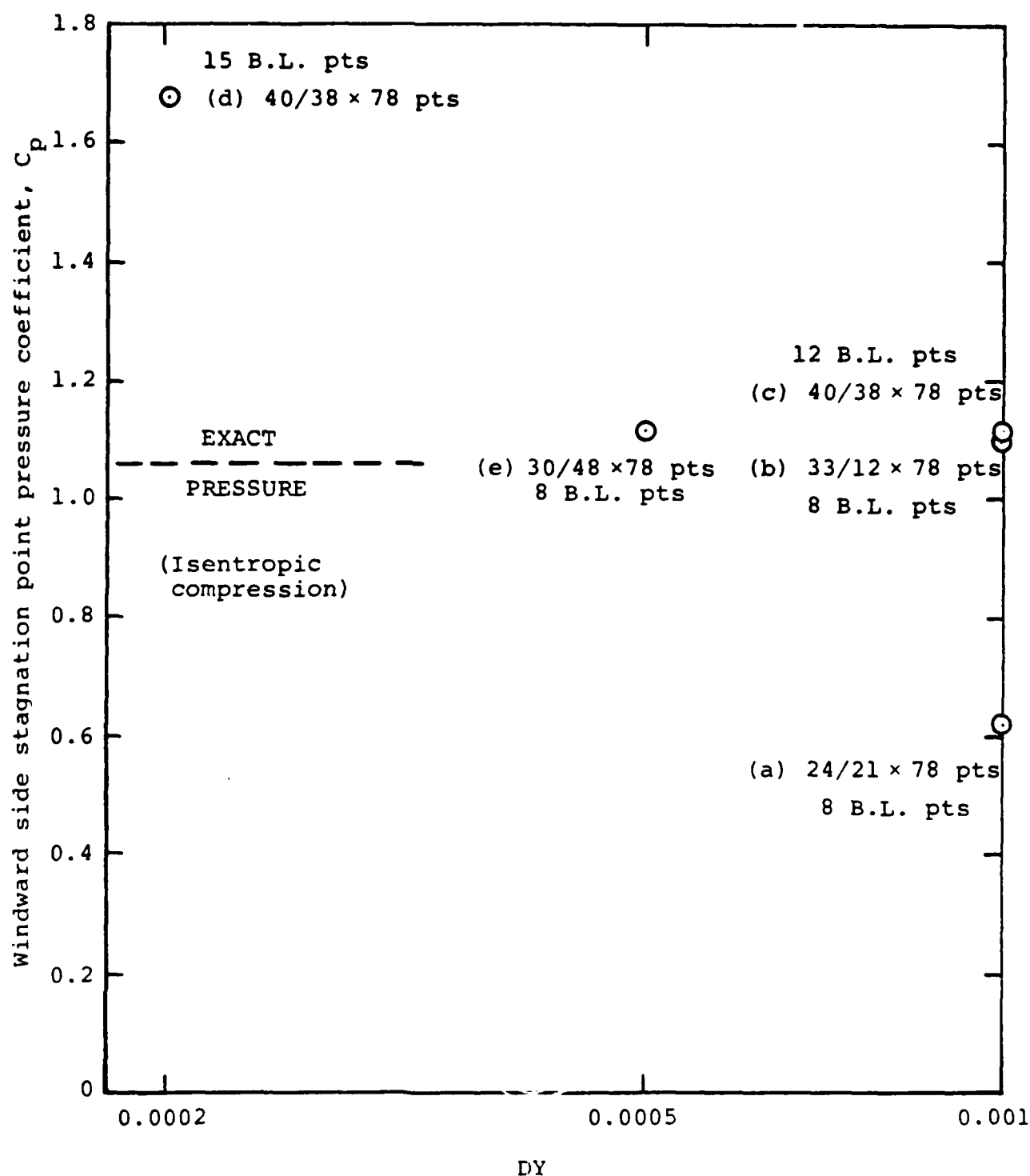


Figure 2. Windward stagnation pressure coefficient as a function of mesh spacing near plate DY and number of points in boundary layer.

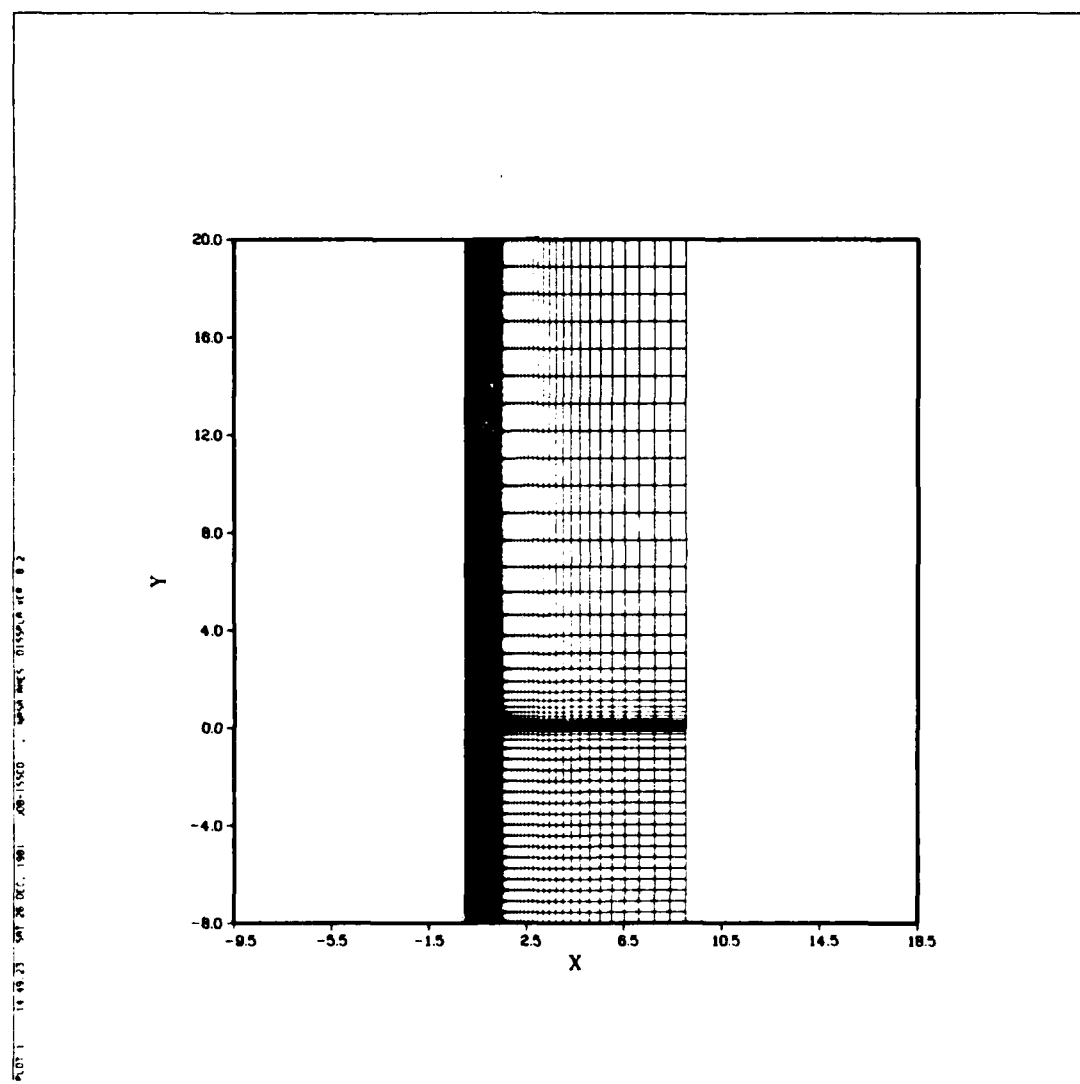


Figure 3. Grid plot for the 2-dimensional strake.

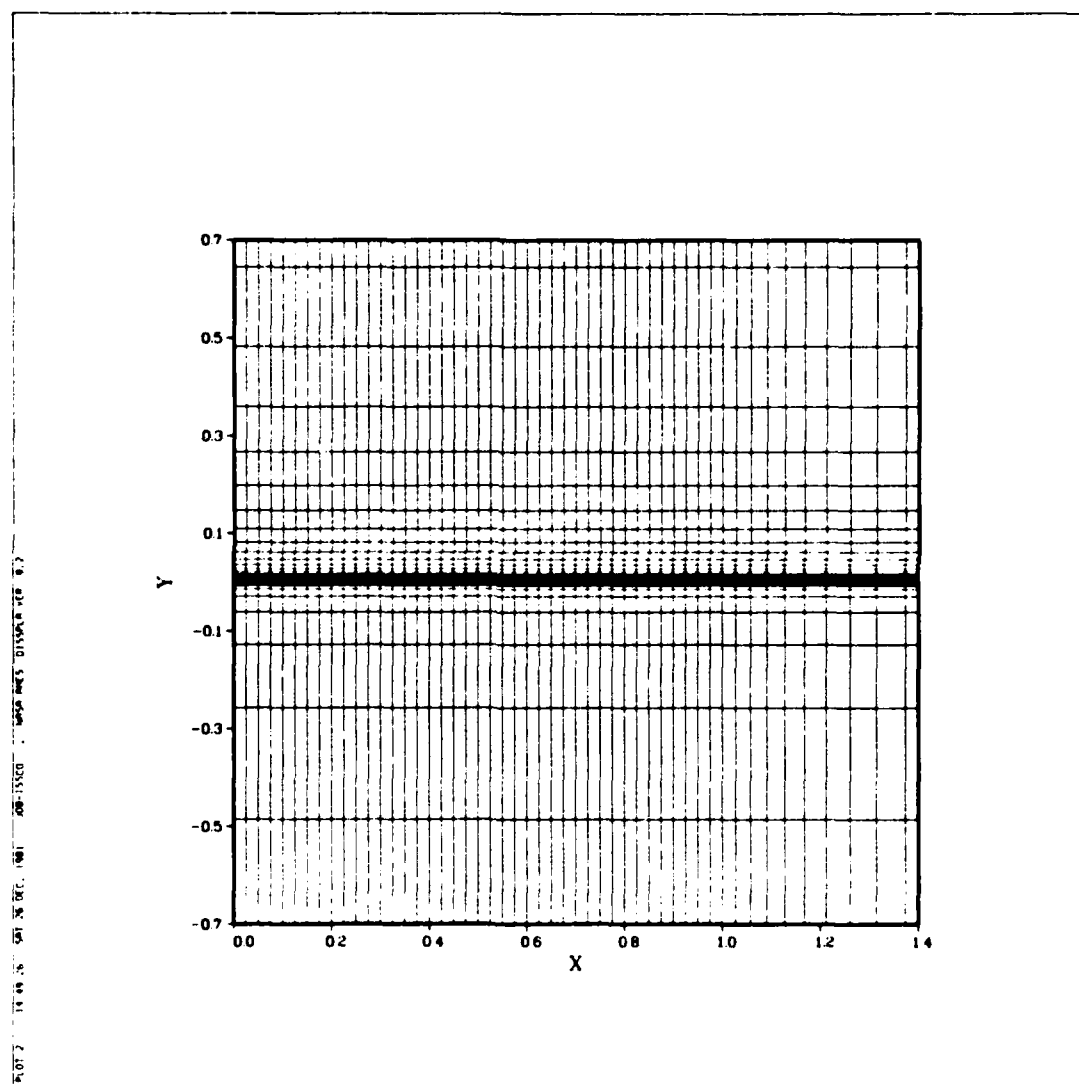


Figure 4. Detail of grid plot near the 2-dimensional strake.

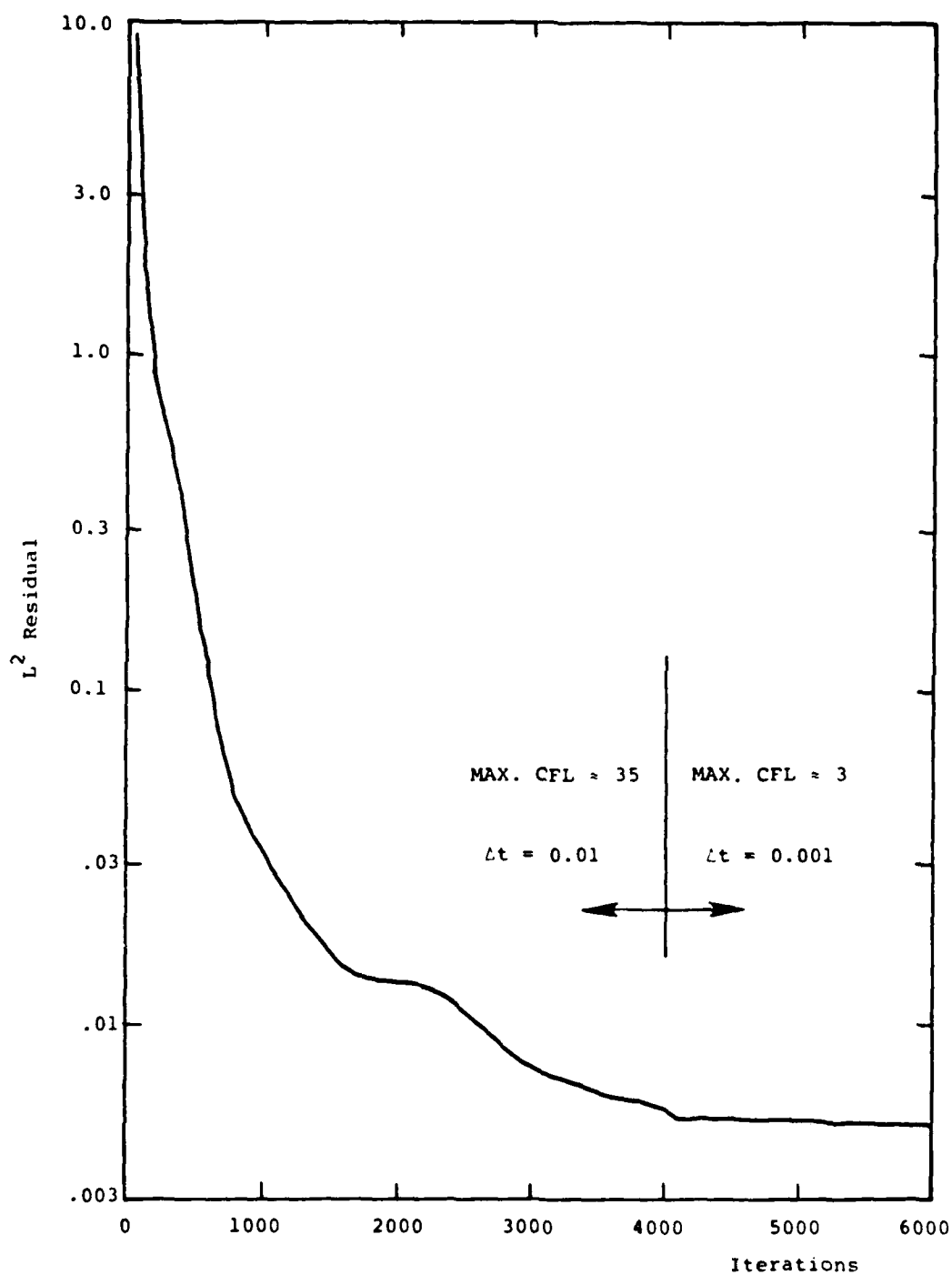


Figure 5. Convergence history - two-dimensional strake
 $M_\infty = 0.5$, $Re = 0.5 \times 10^6$.

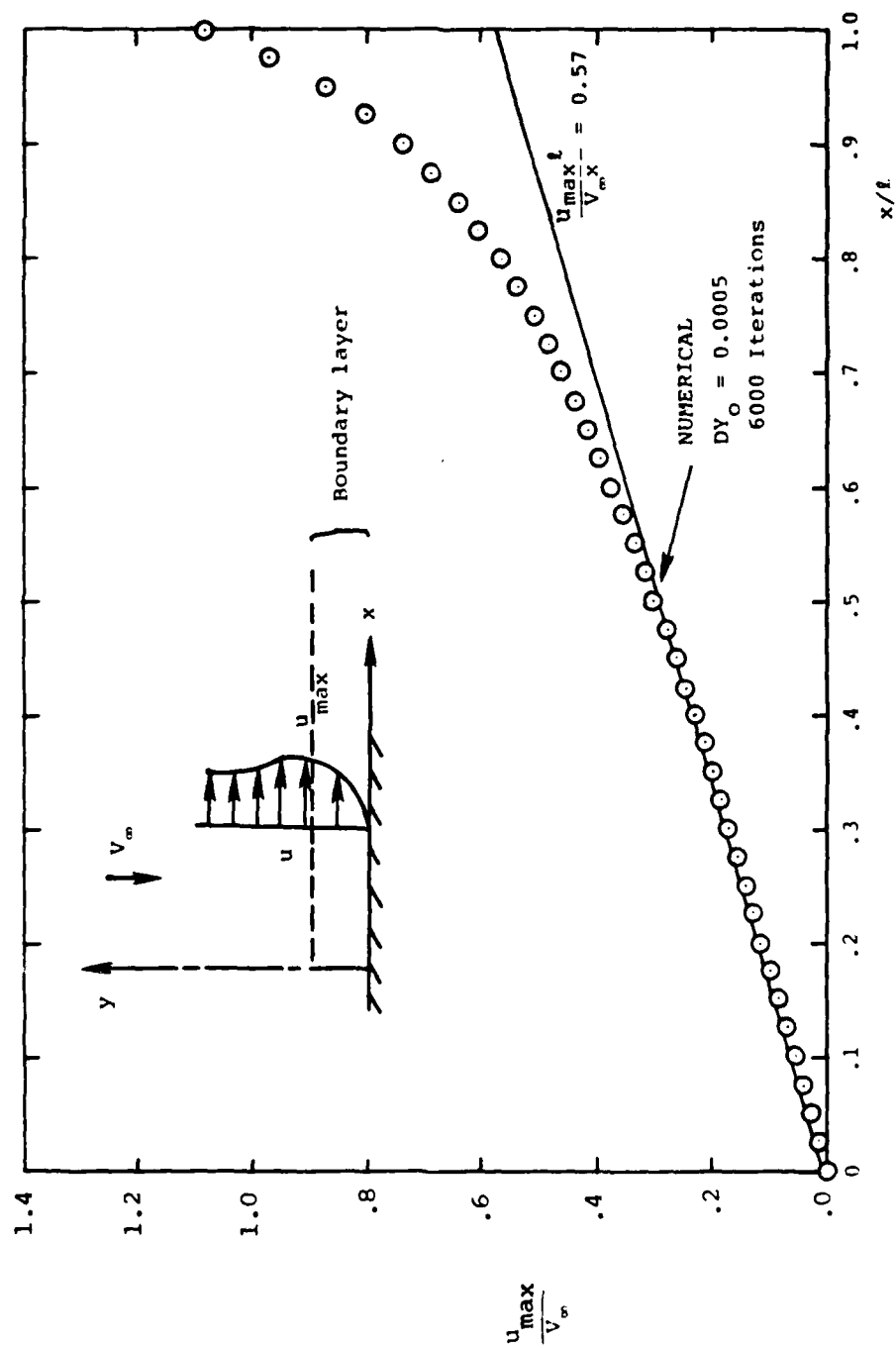


Figure 6. External velocity of stagnation point flows.

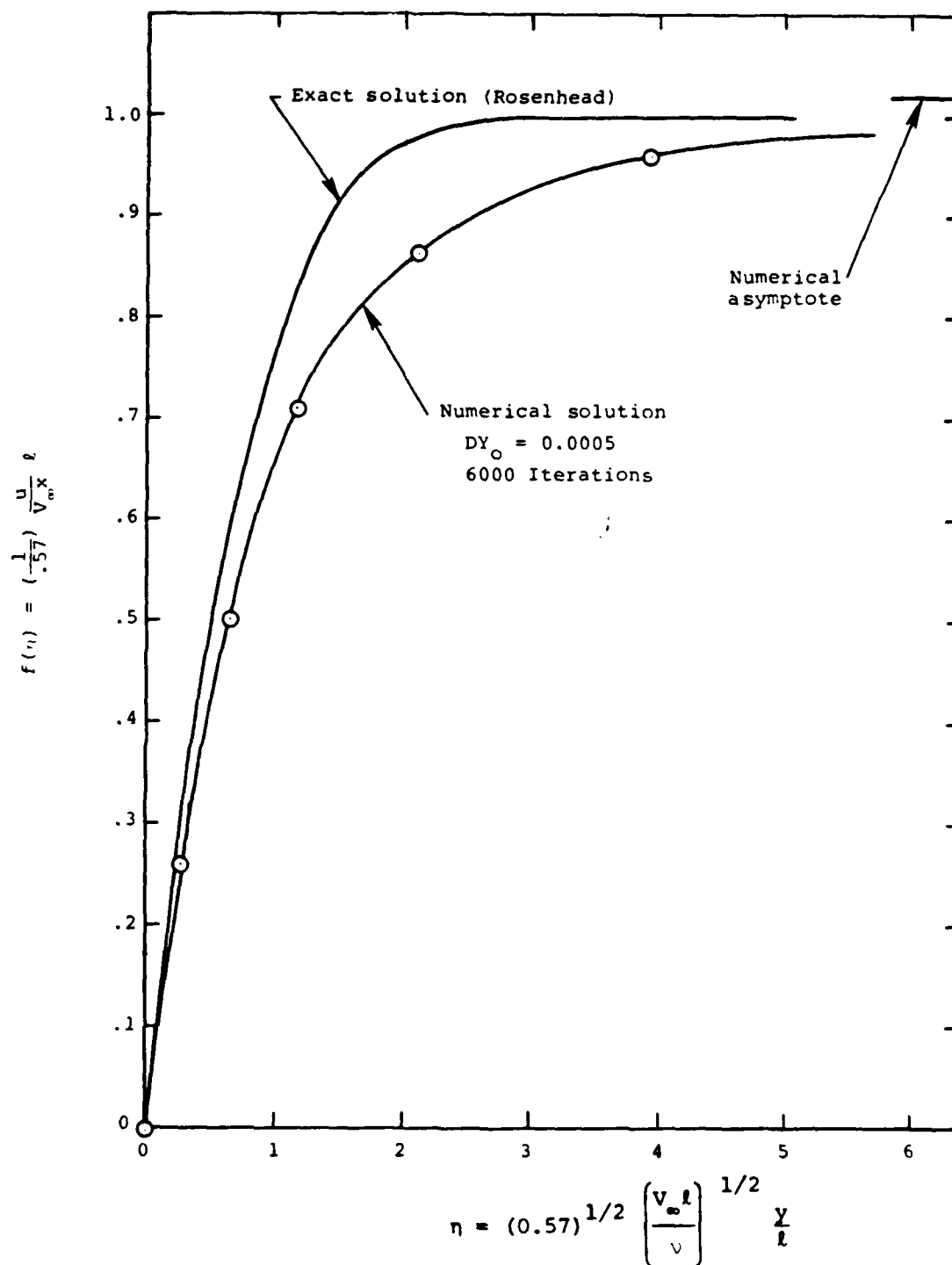


Figure 7. Stagnation point boundary layer velocity profiles.

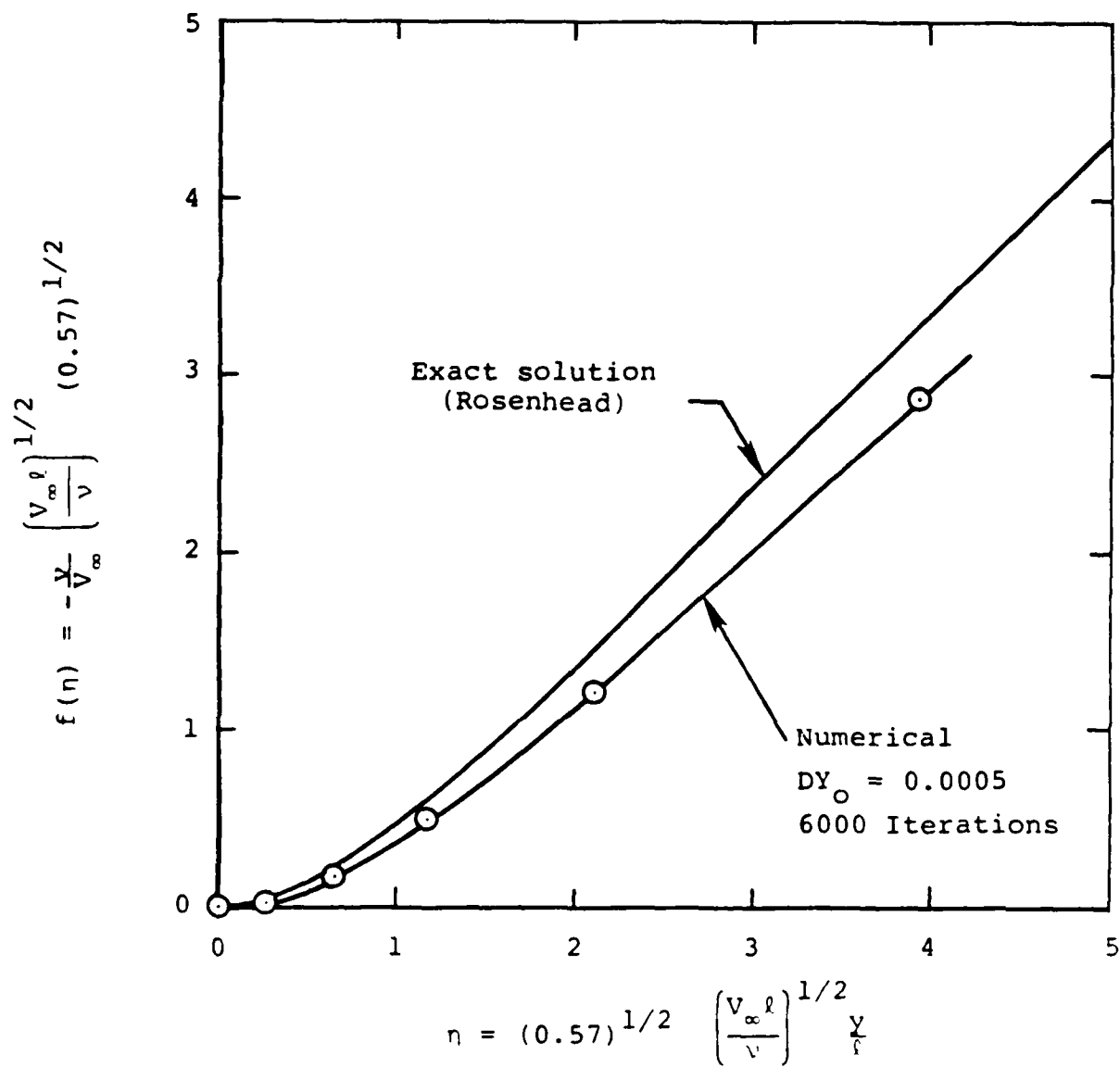
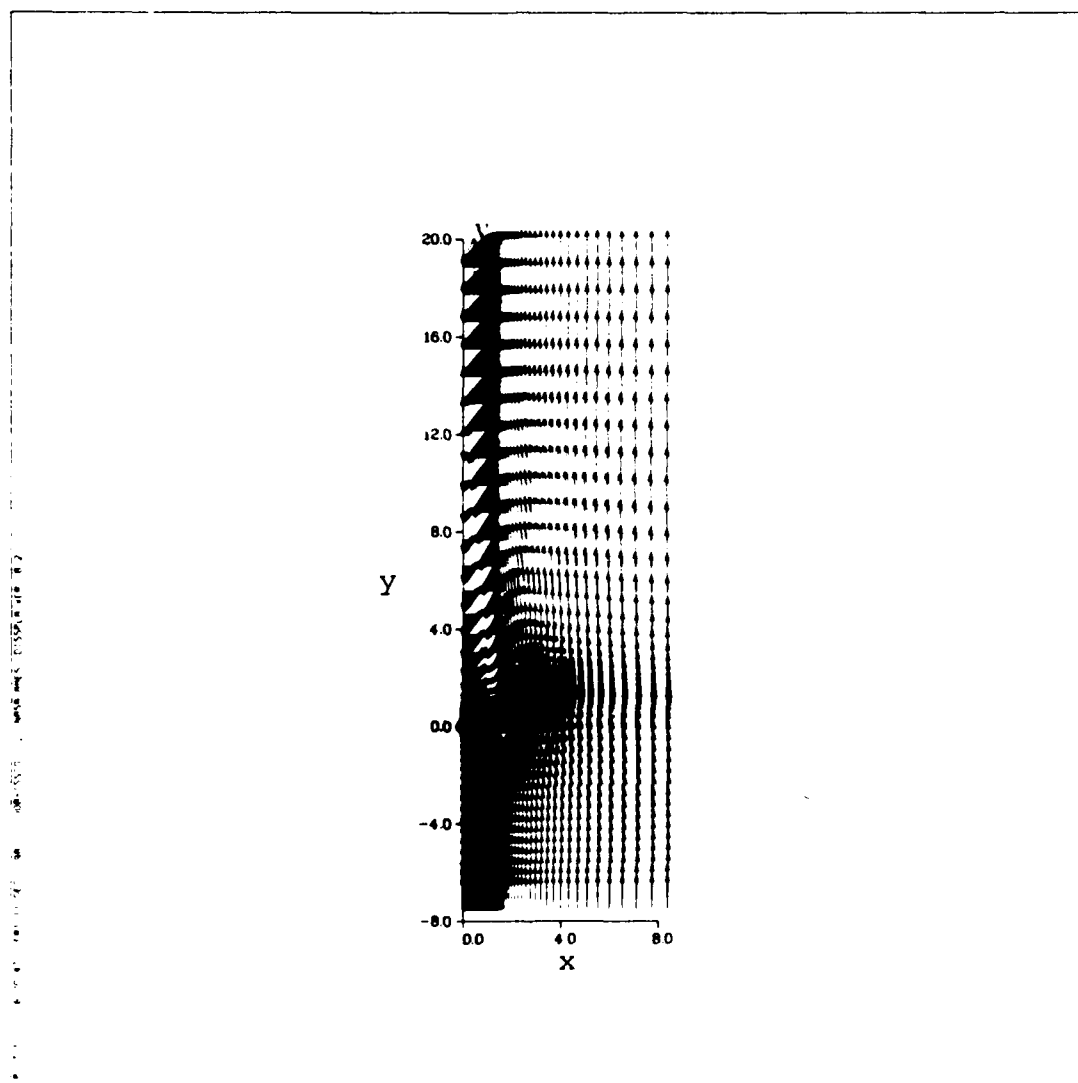
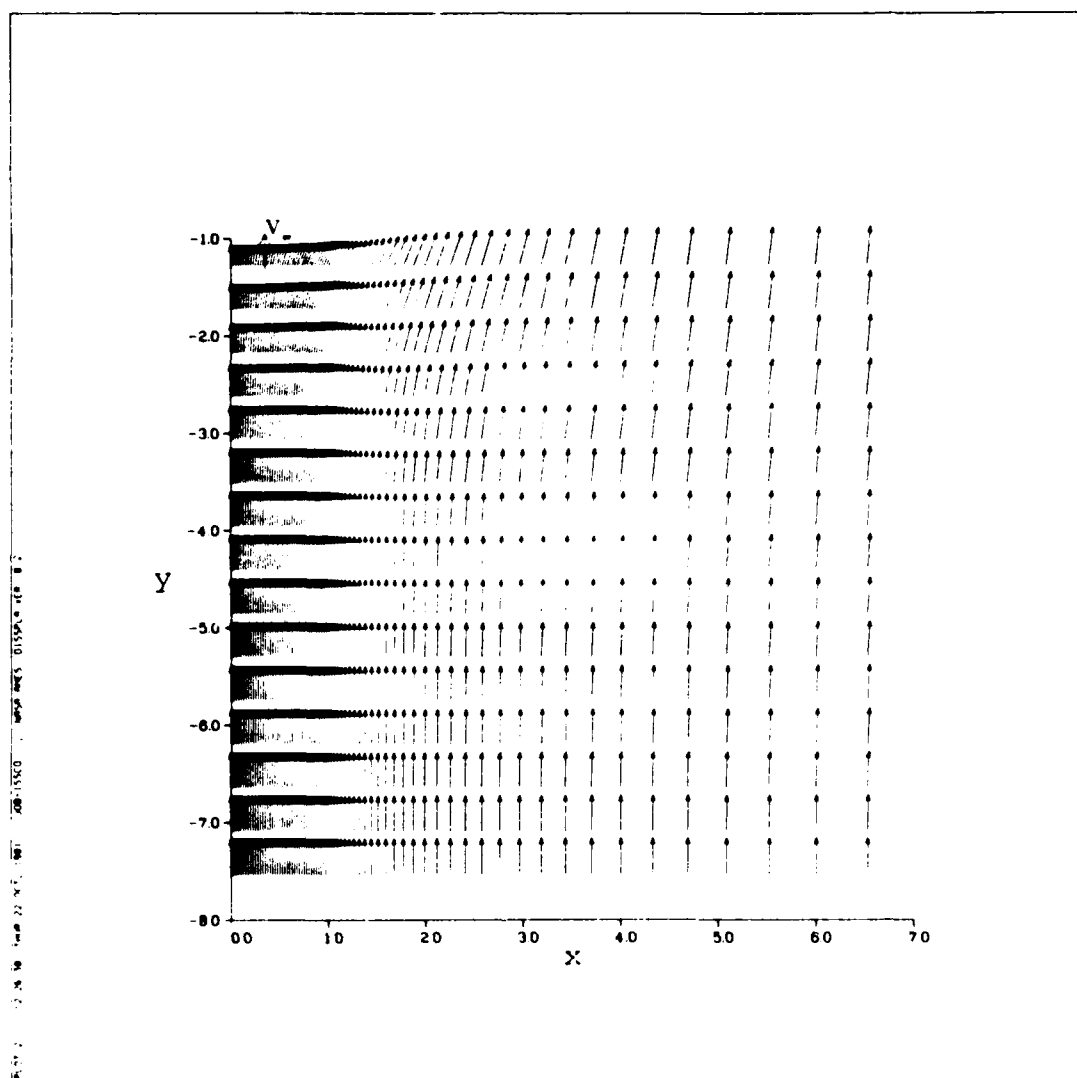


Figure 8. Stagnation point boundary layer velocity profiles.

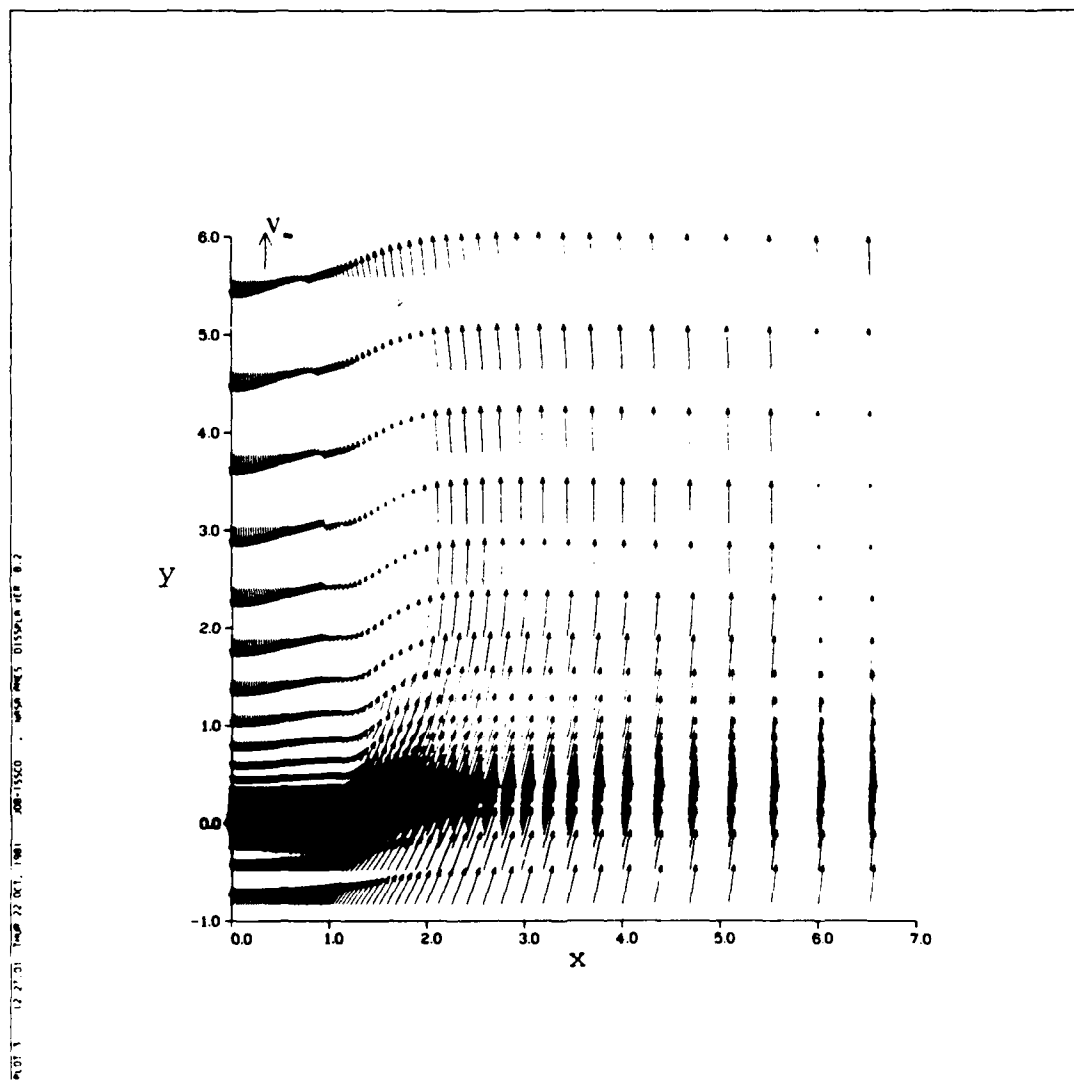


(a) Entire flow domain

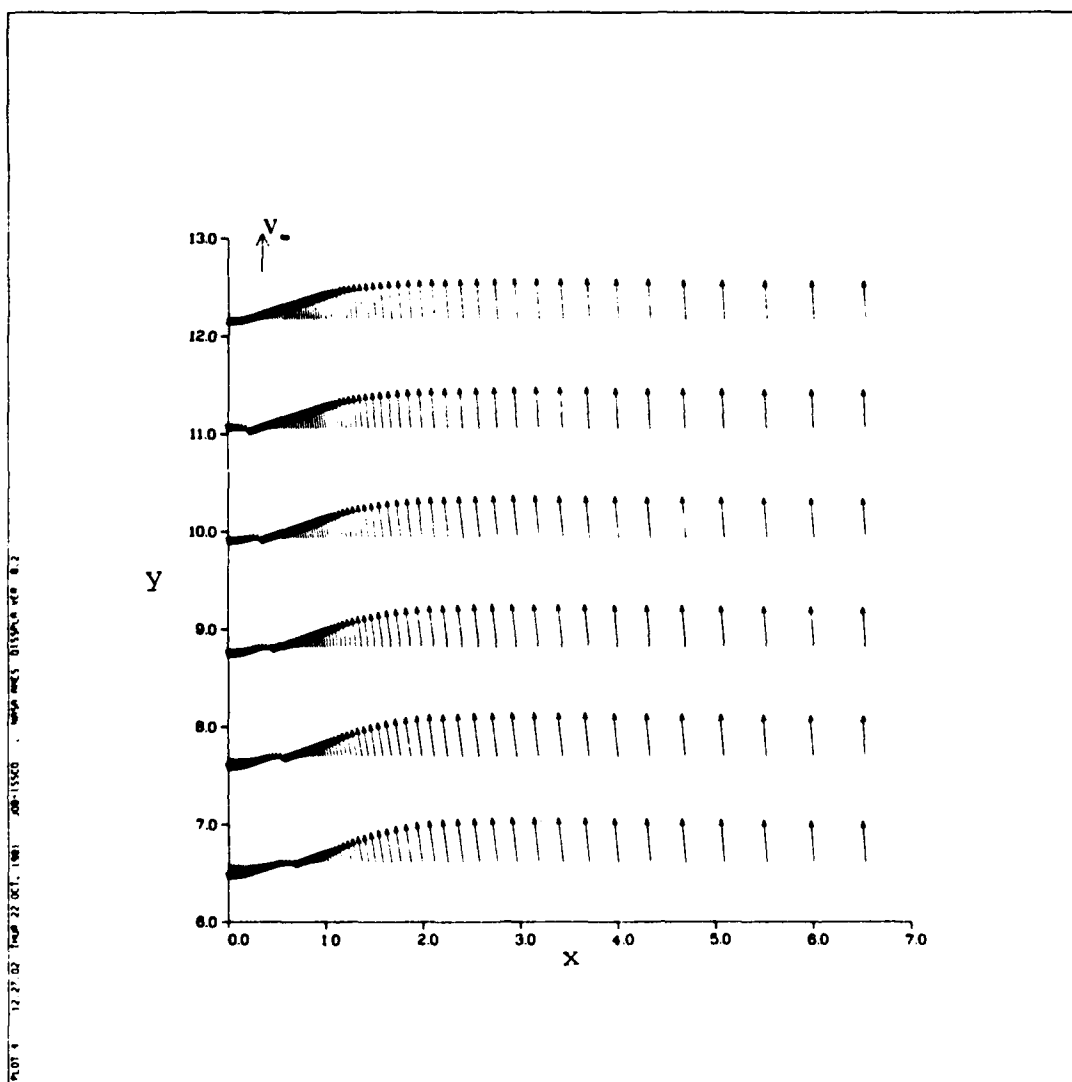
Figure 9. Velocity vector plot.



(b) Flow detail upstream of plate
Figure 9. (Continued).

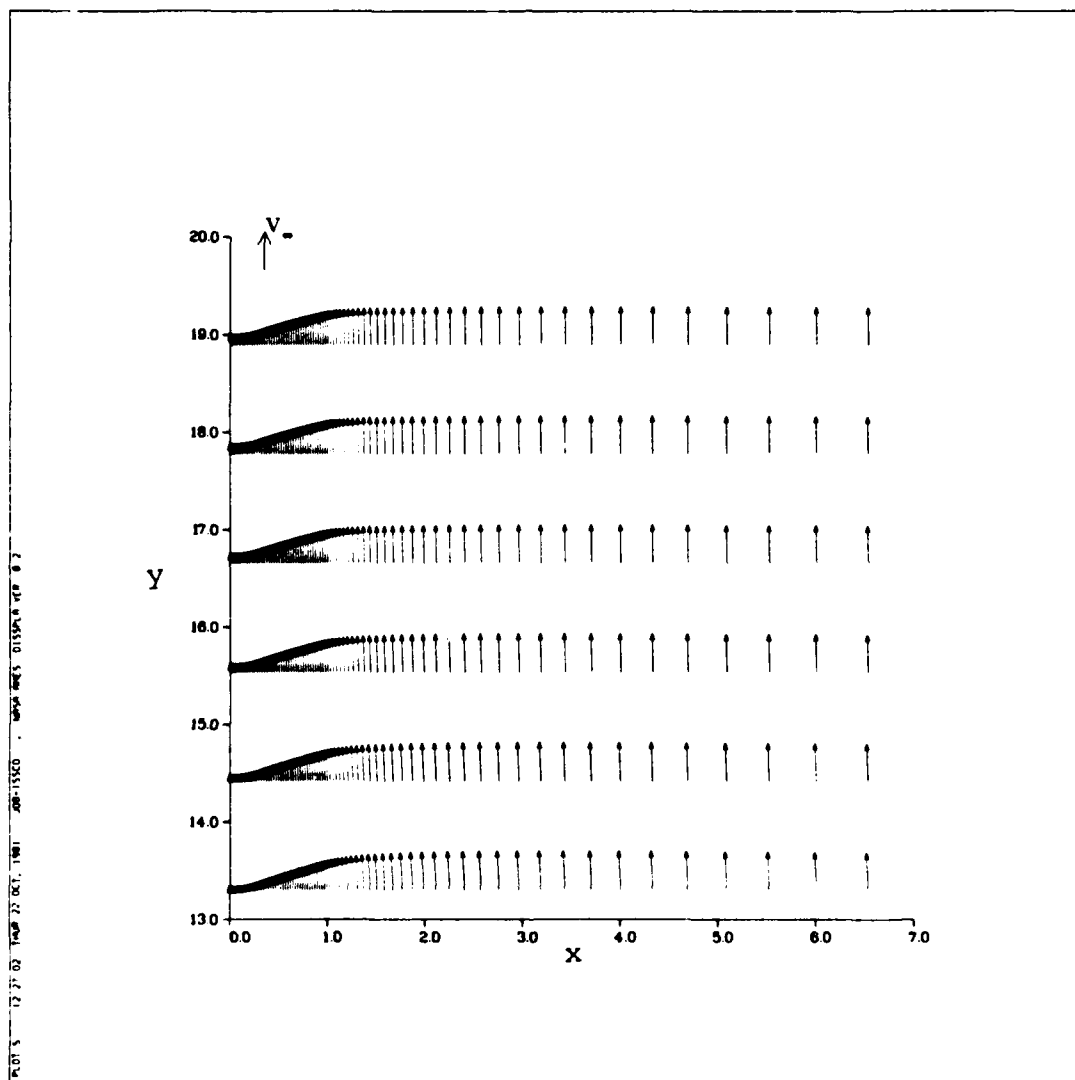


(c) Flow detail just downstream of plate
Figure 9. (Continued).



(d) Flow detail near aft end of separation bubble

Figure 9. (Continued).



(e) Flow detail well downstream of plate
Figure 9. (Concluded).

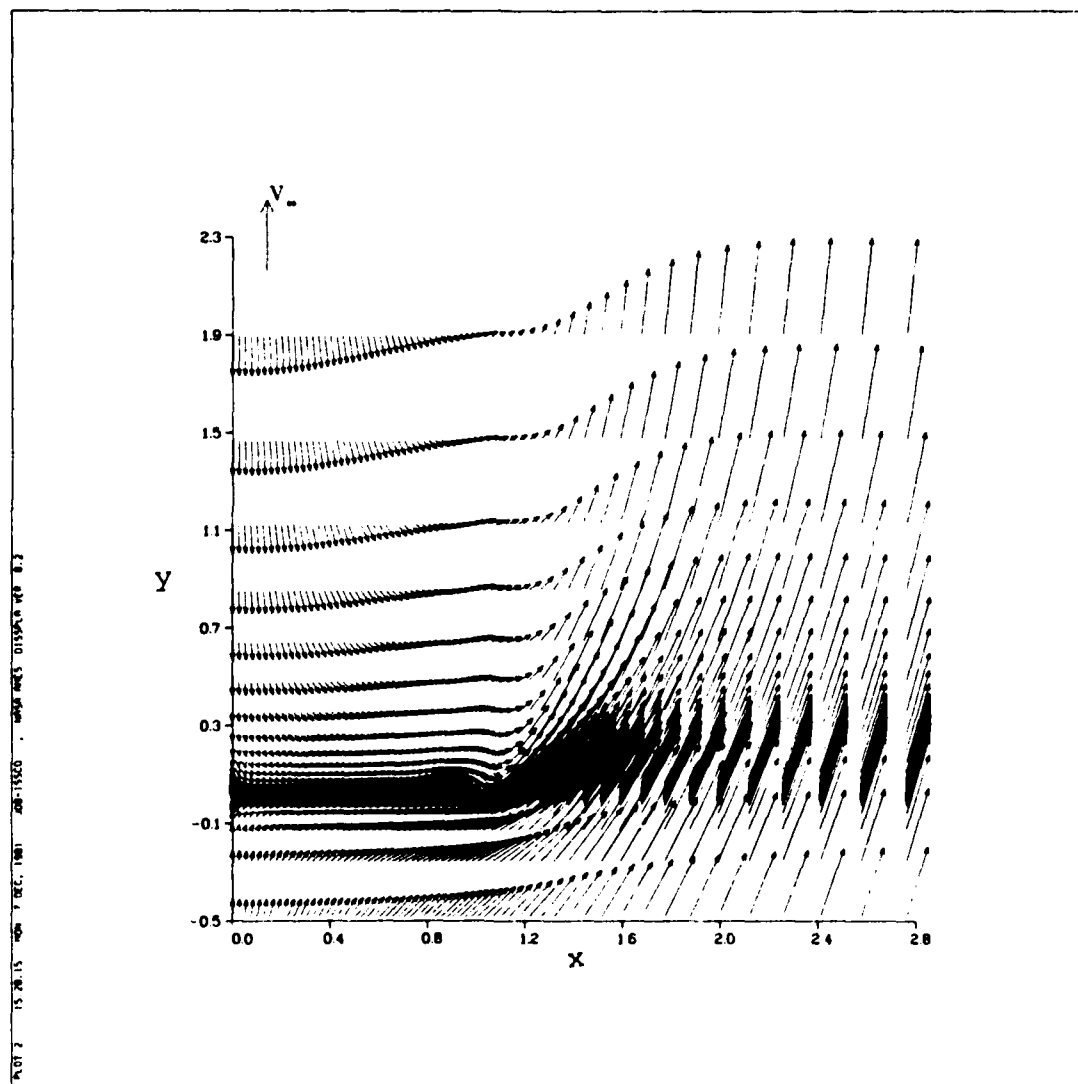
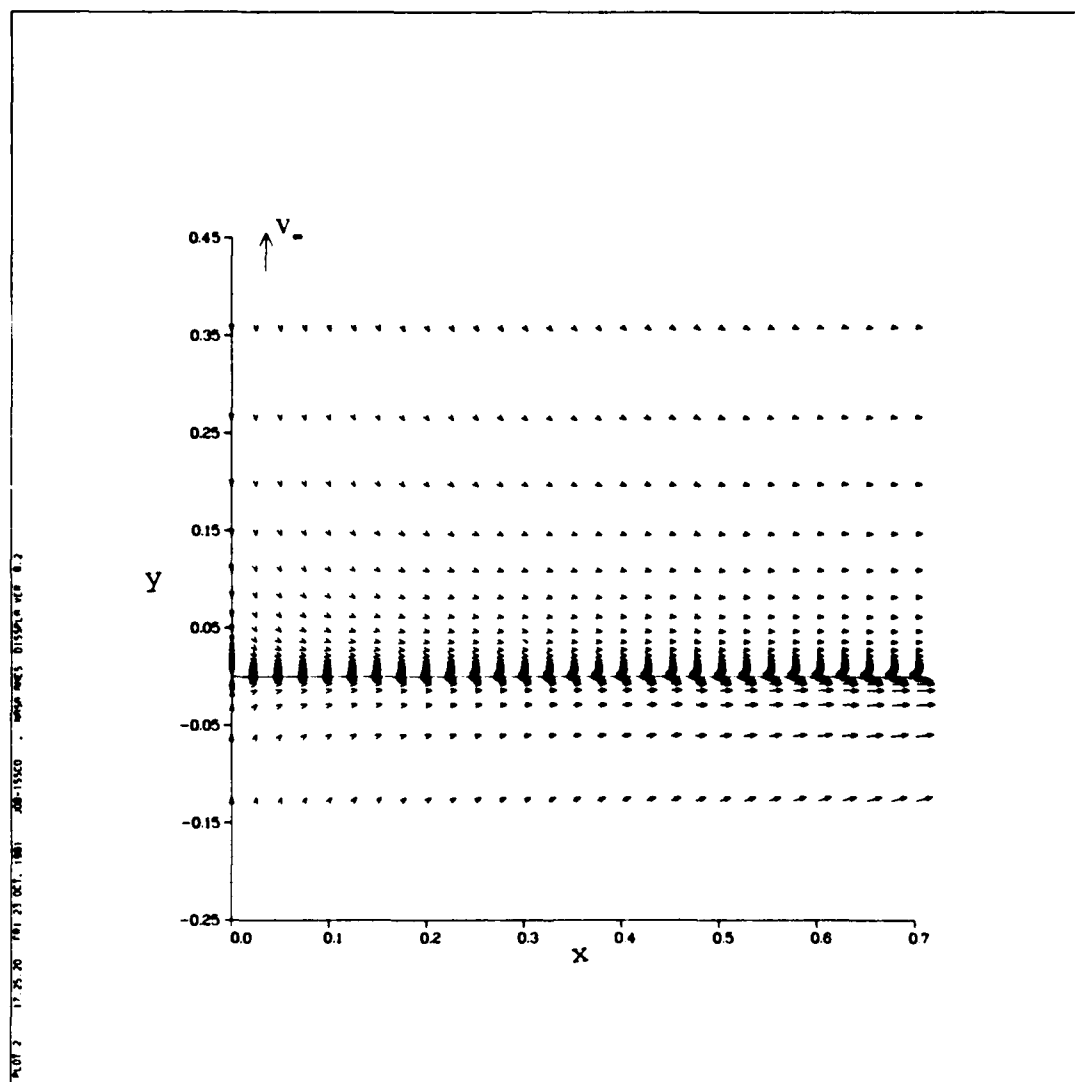
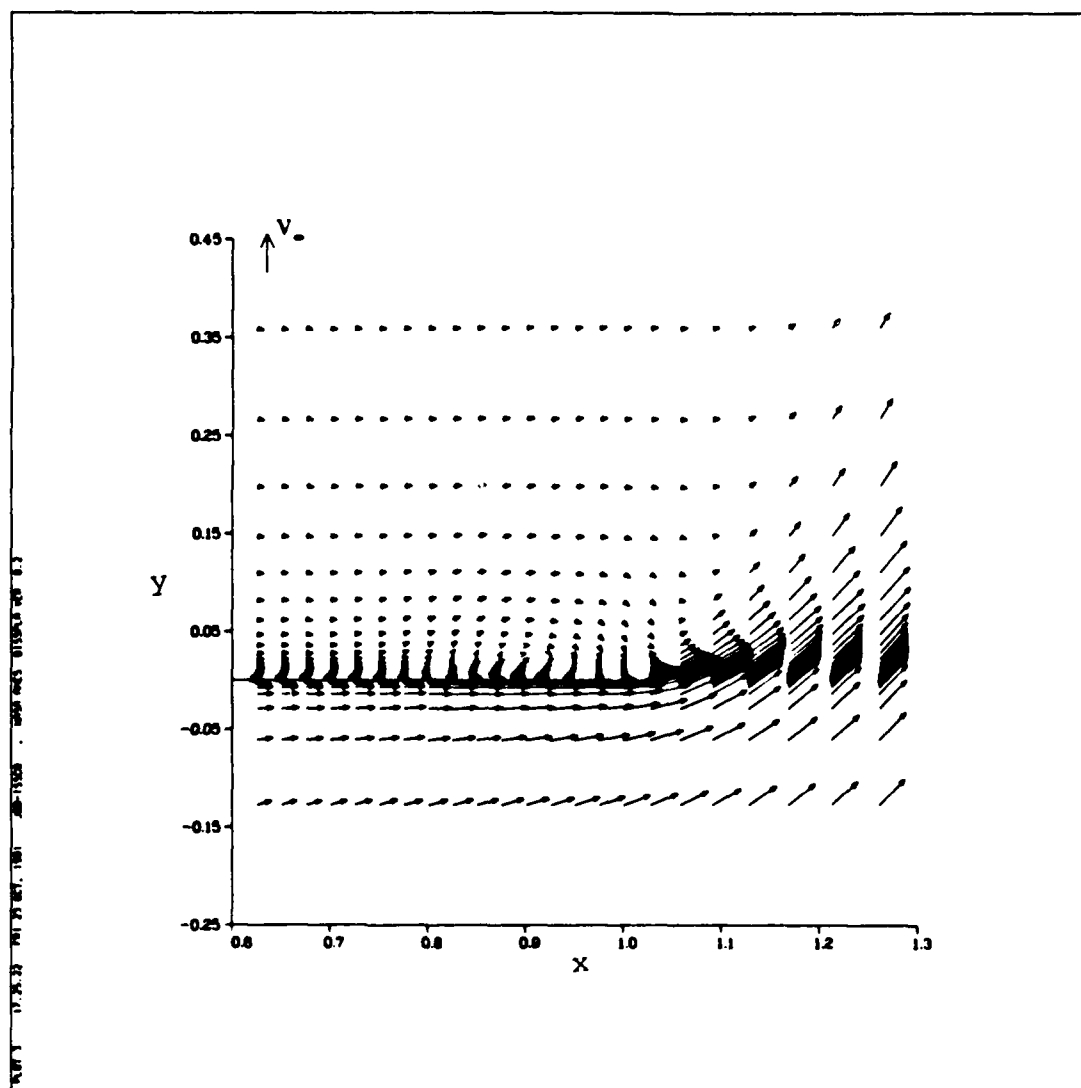


Figure 10. Detail of velocity vector plot.



(a) Inner part of plate

Figure 11. Detailed velocity vector plot of the flat plate boundary layer.



(b) Region near plate edge
Figure 11. (Concluded).

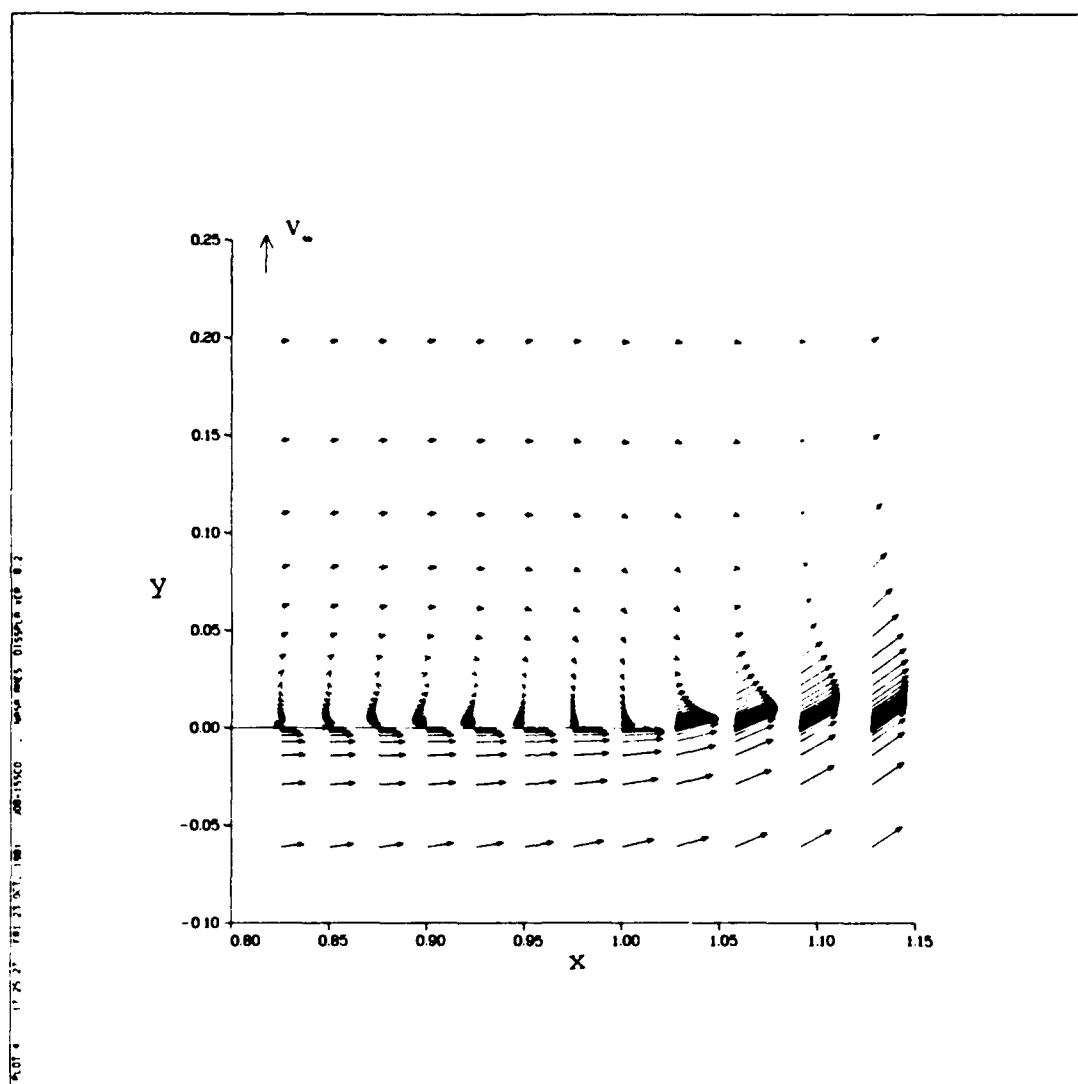


Figure 12. Detailed velocity vector plot of secondary separation bubble and shear surface

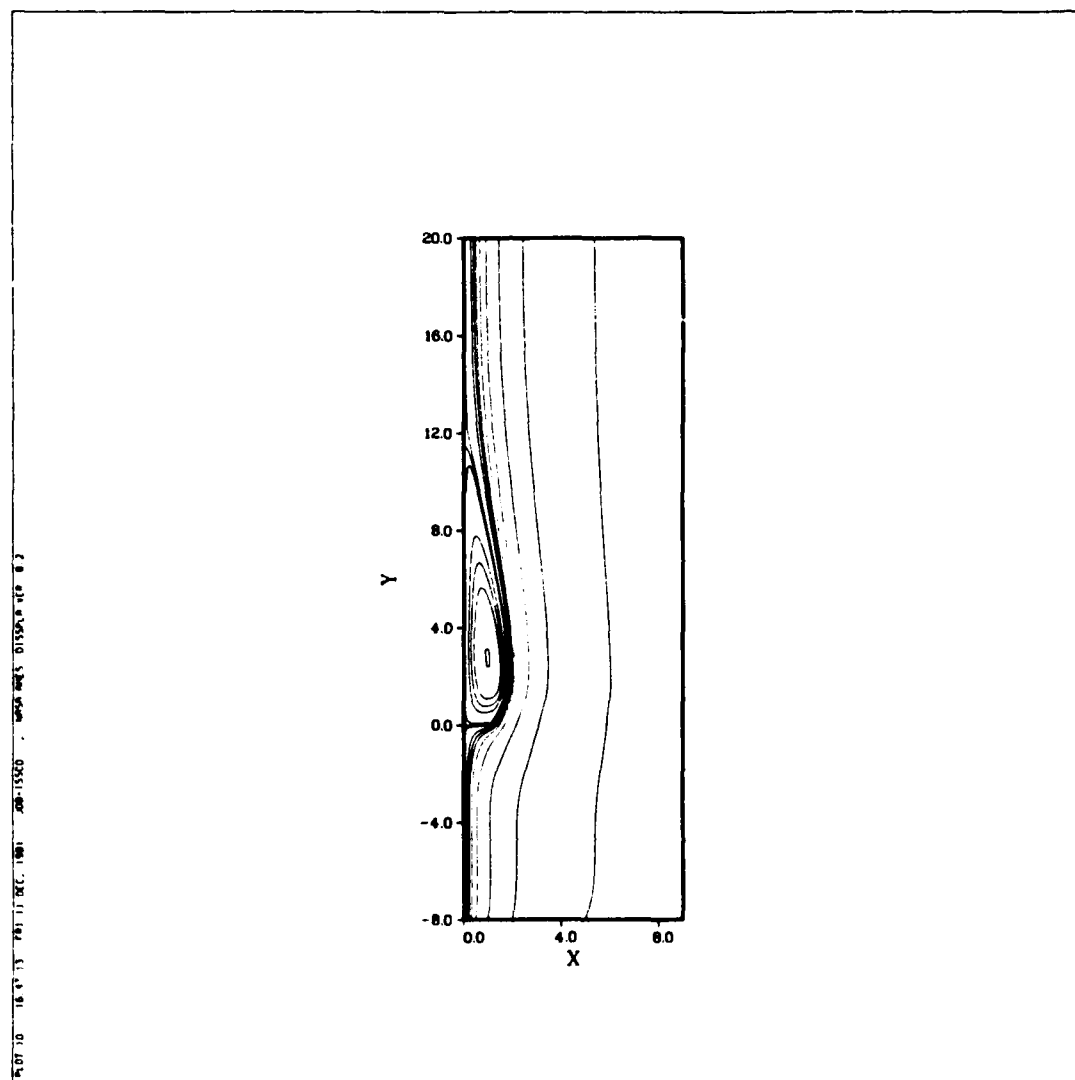


Figure 13. Stream function contour of entire domain.

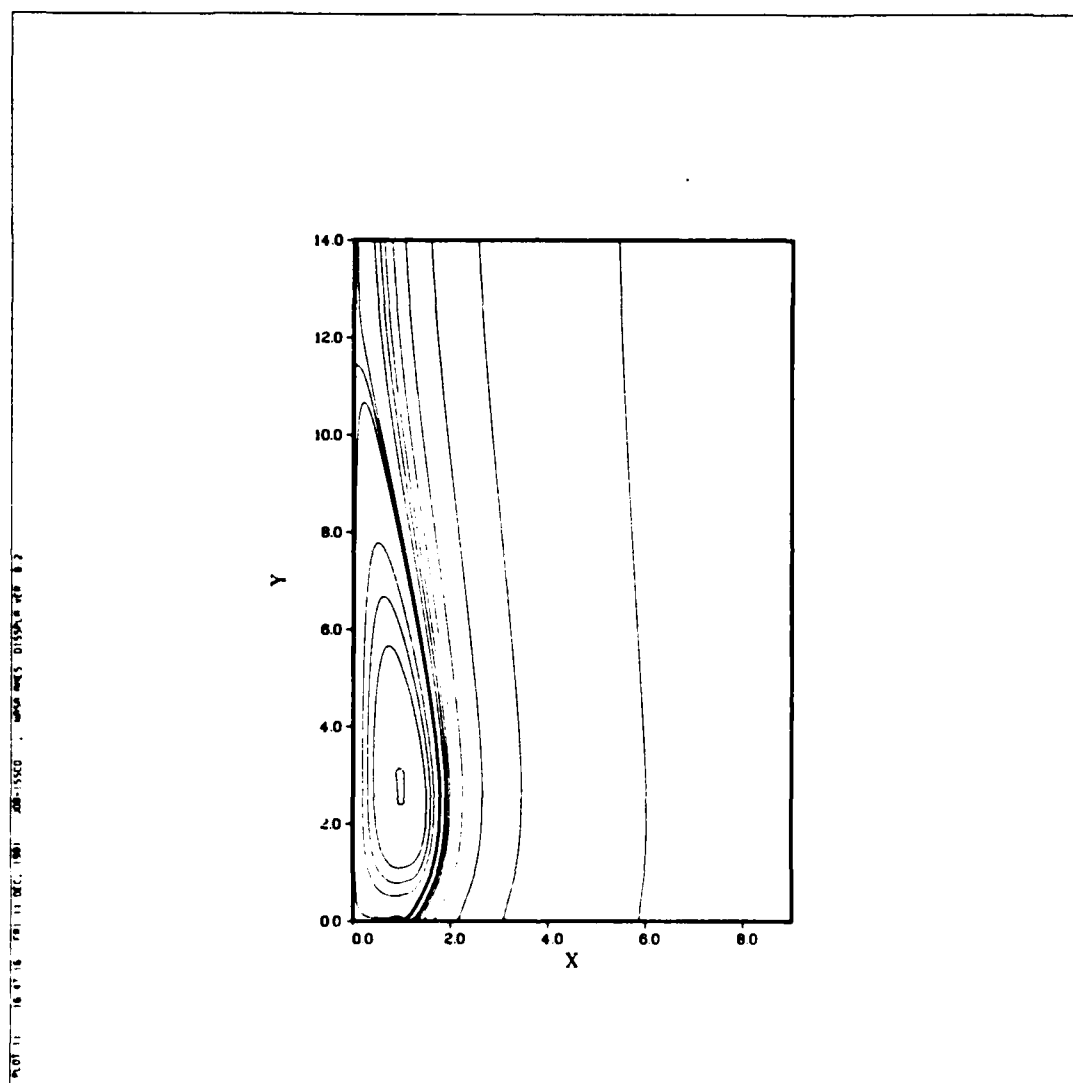


Figure 14. Stream function contours
of leeside of the plate.

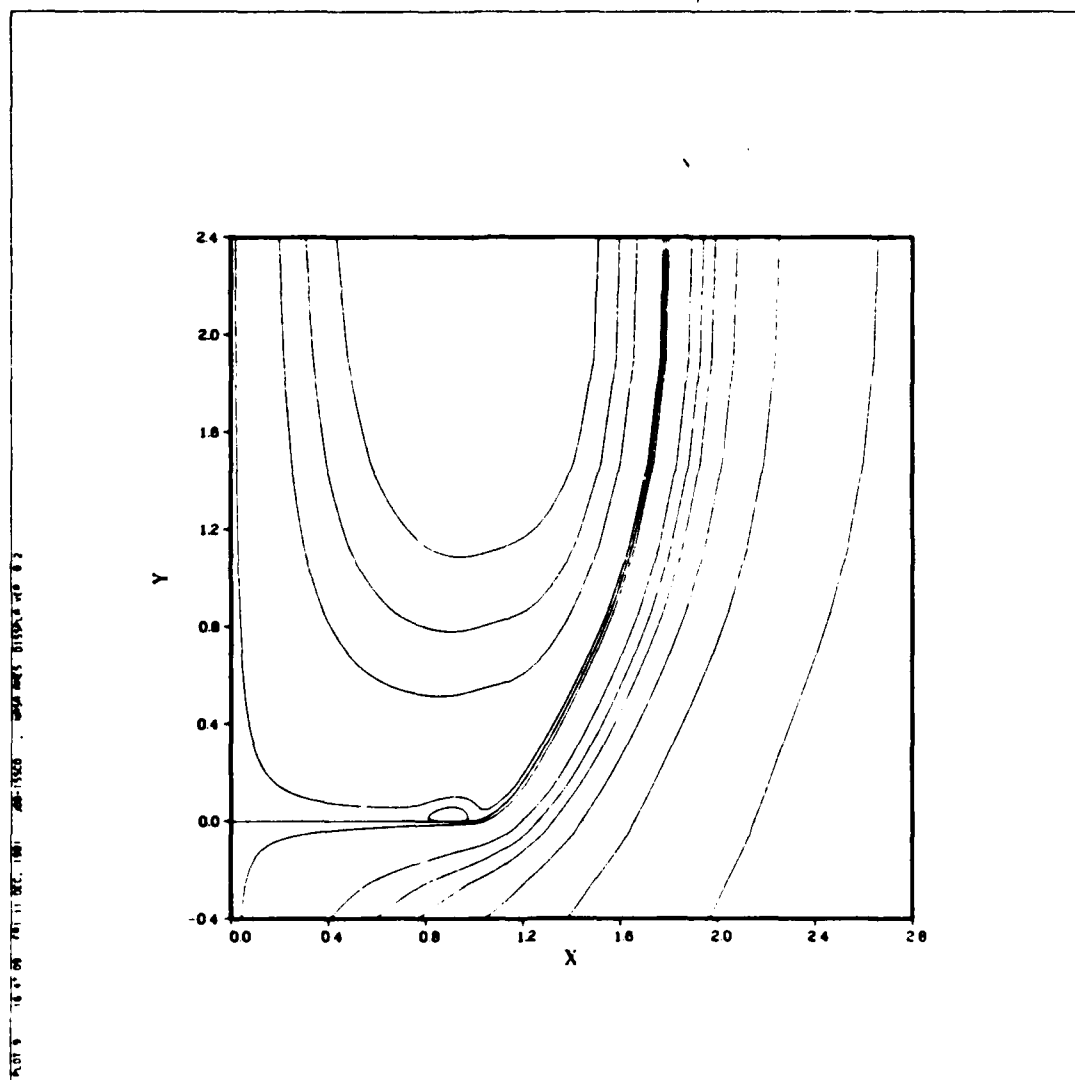


Figure 15. Stream function contours of secondary separation bubble and shear surface.

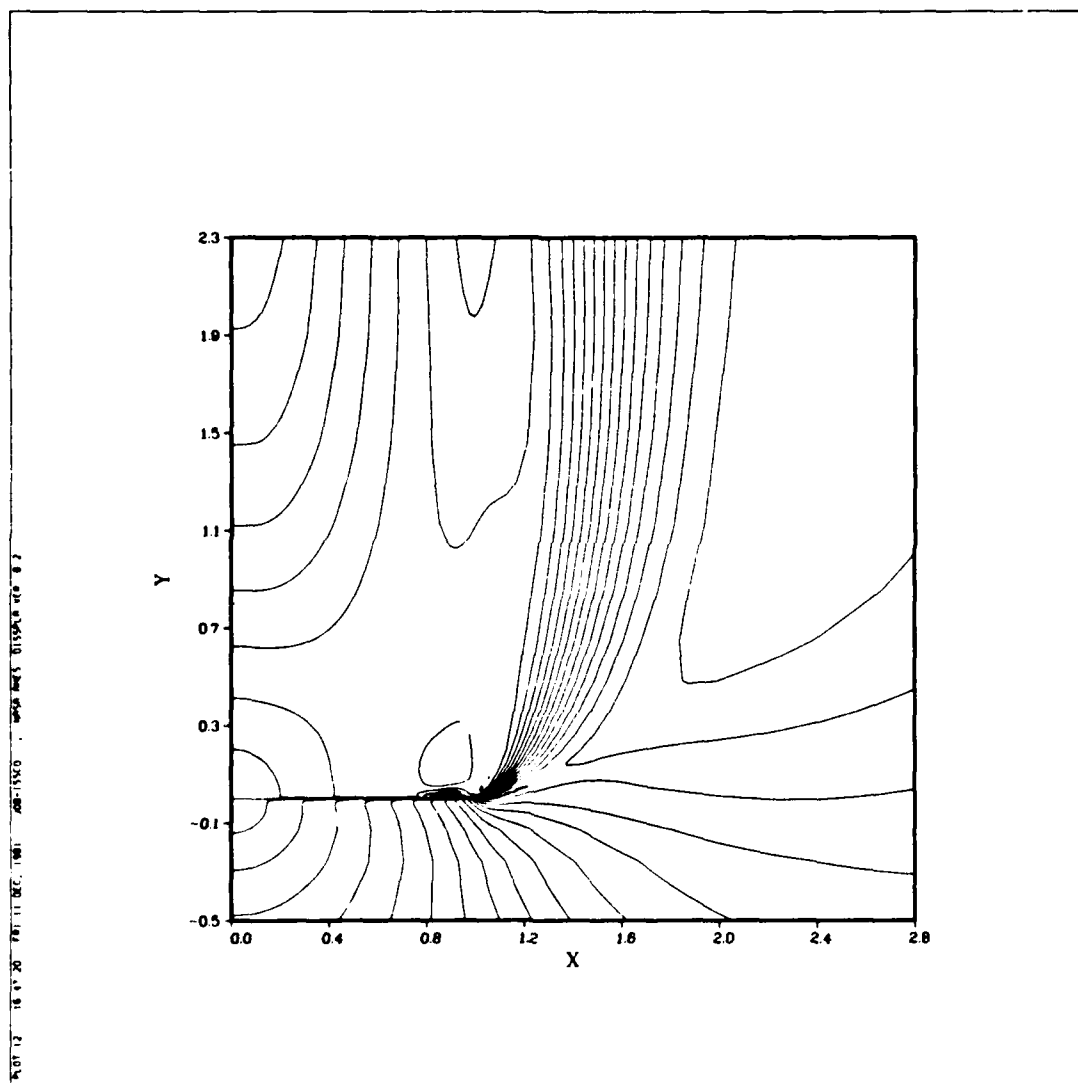


Figure 16. Mach number contours of flow over plate
at $M_\infty = 0.5$ and $Re = 0.5 \times 10^6$.

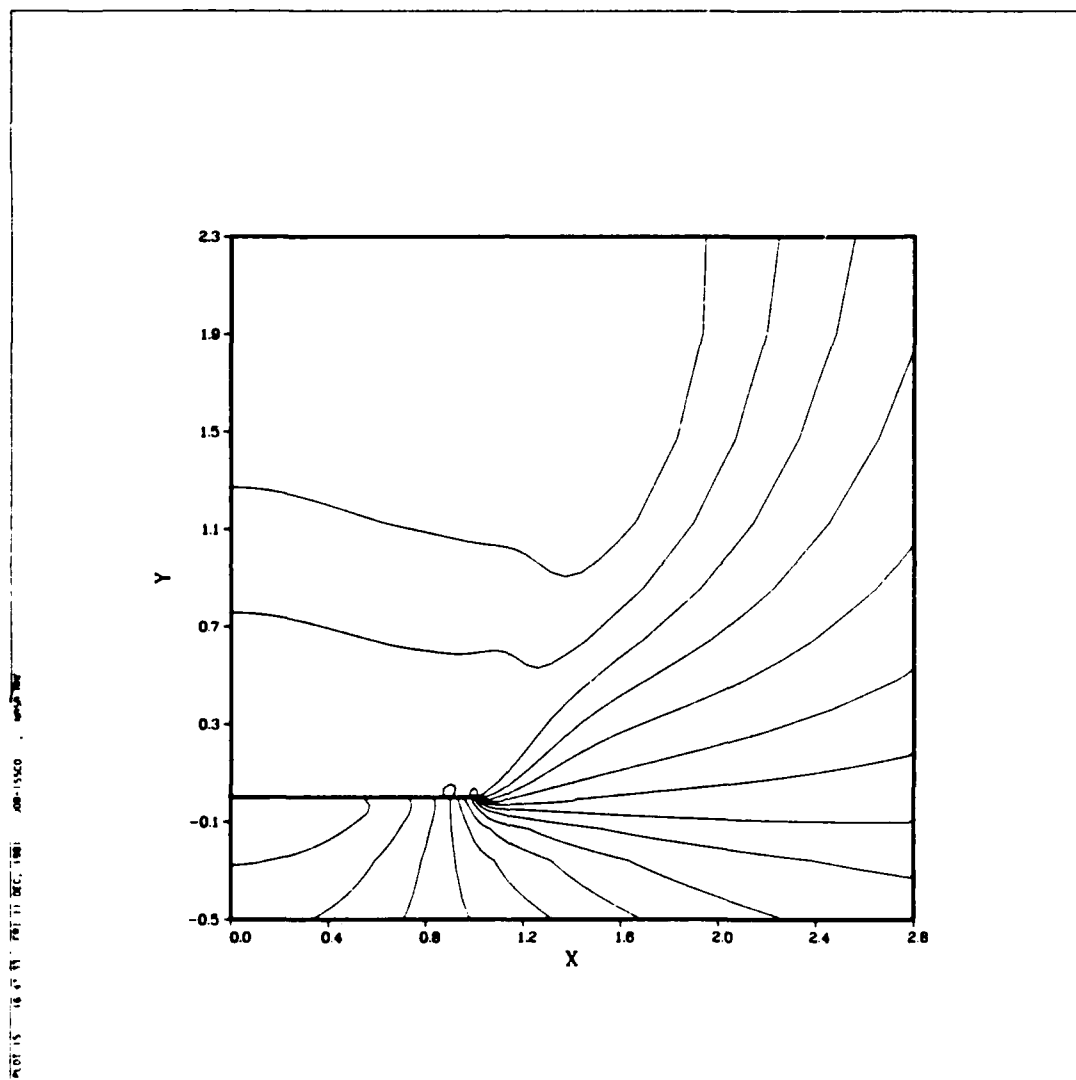


Figure 17. Pressure contours of flow over plate at $M_\infty = 0.5$ and $Re = 0.5 \times 10^6$.

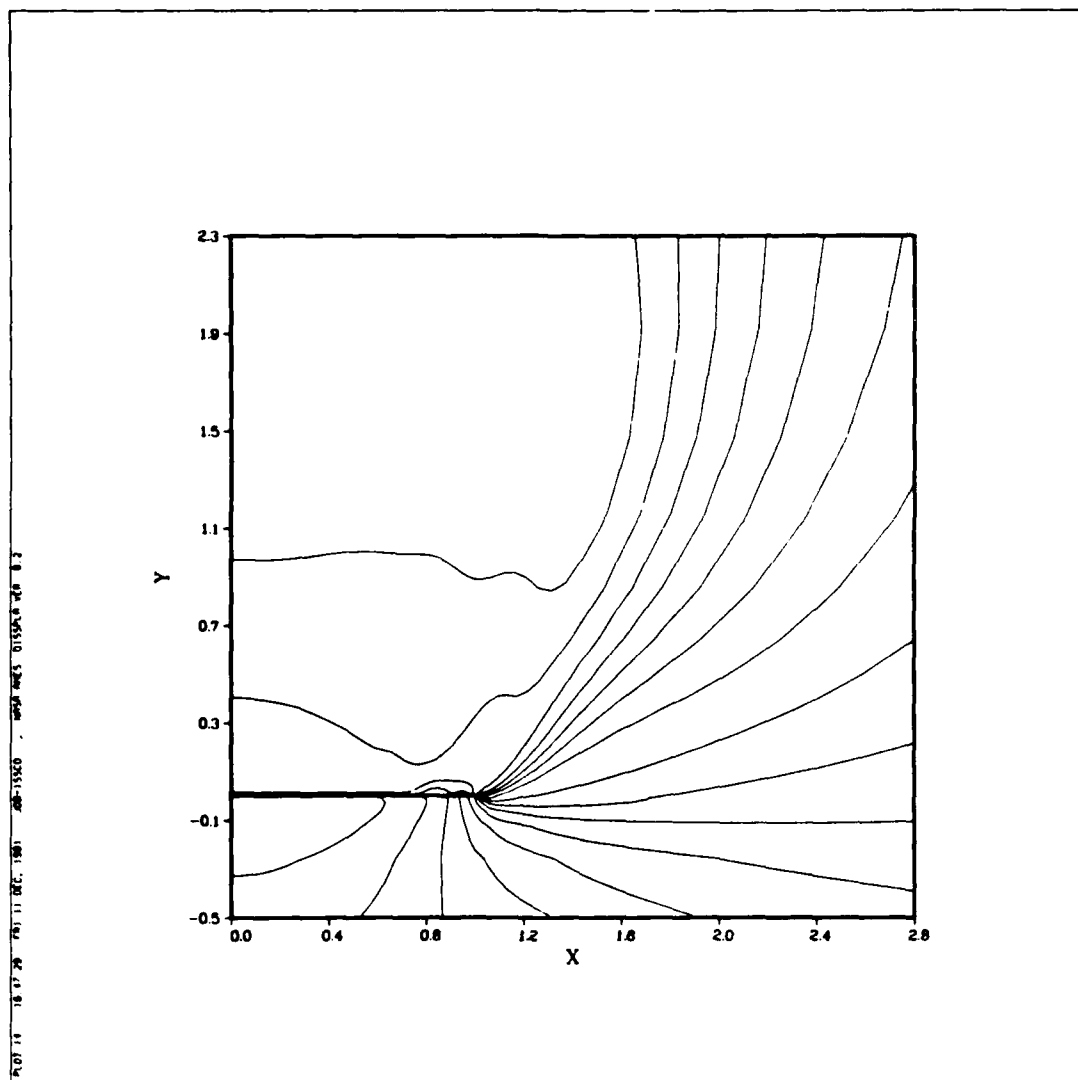


Figure 18. Density contours of flow over plate
at $M_{\infty} = 0.5$ and $Re = 0.5 \times 10^6$.

Stagnation Line Pressure

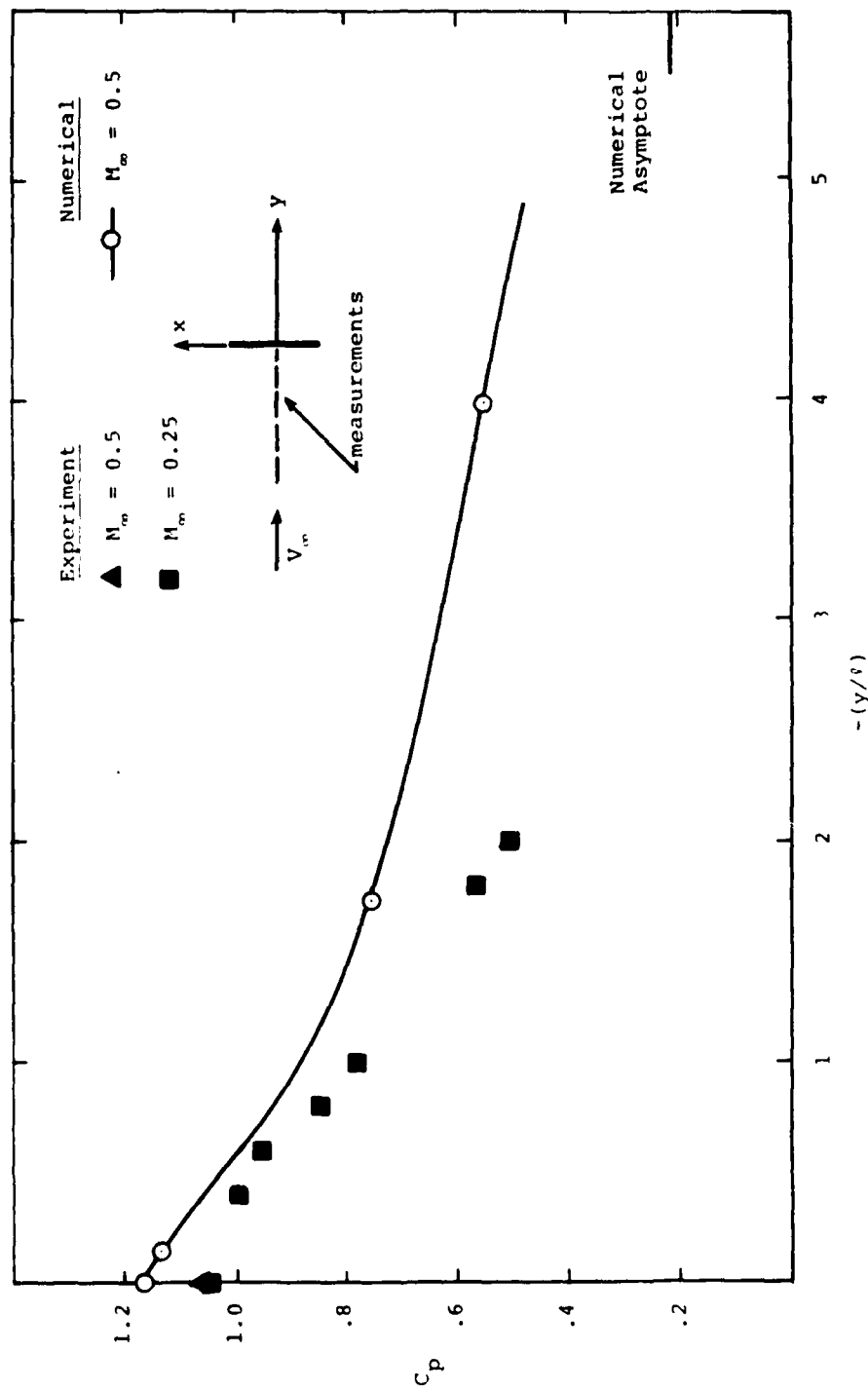


Figure 19. Windward stagnation line static pressure coefficient ($x/l = 0$).

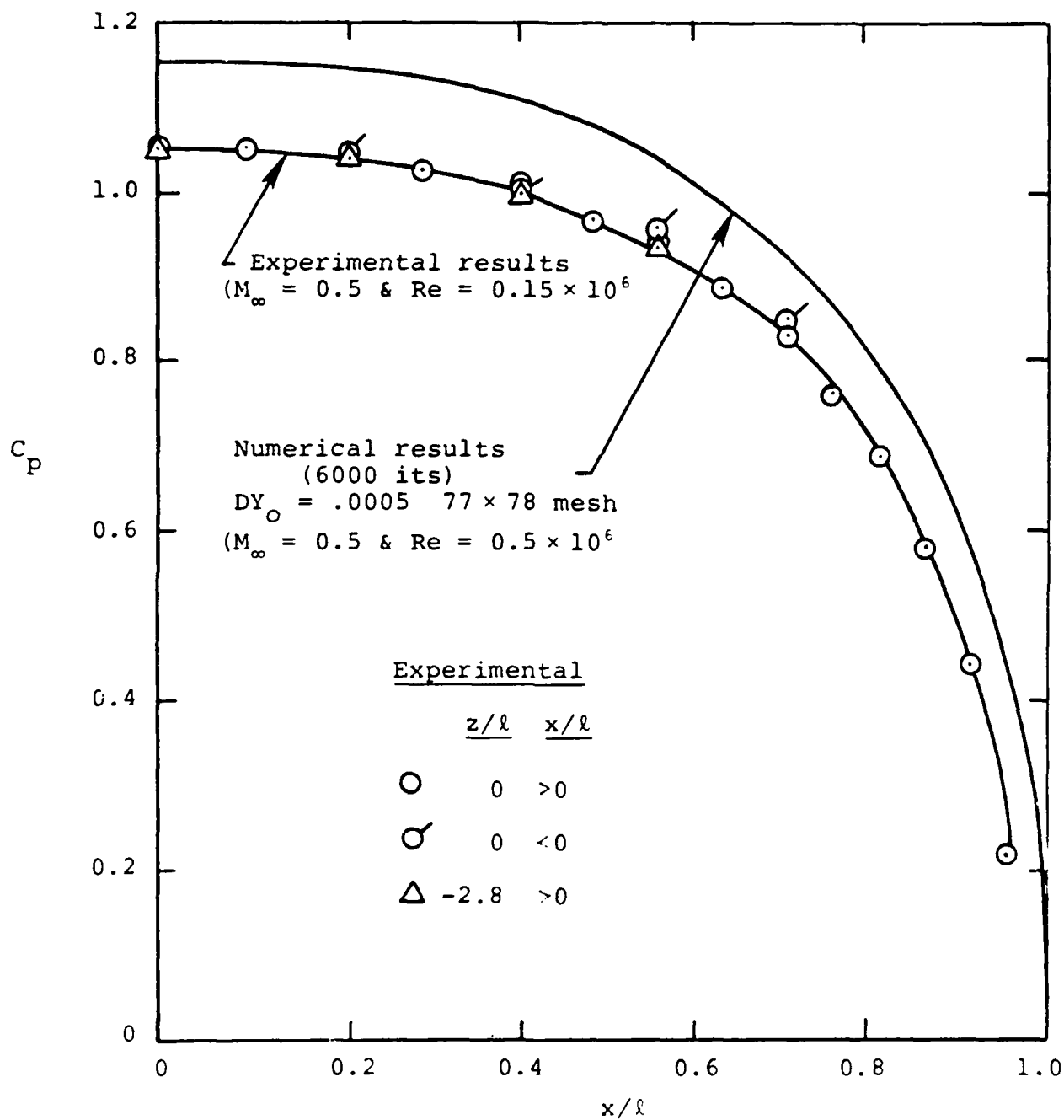


Figure 20. Static pressure on windward side of the plate.

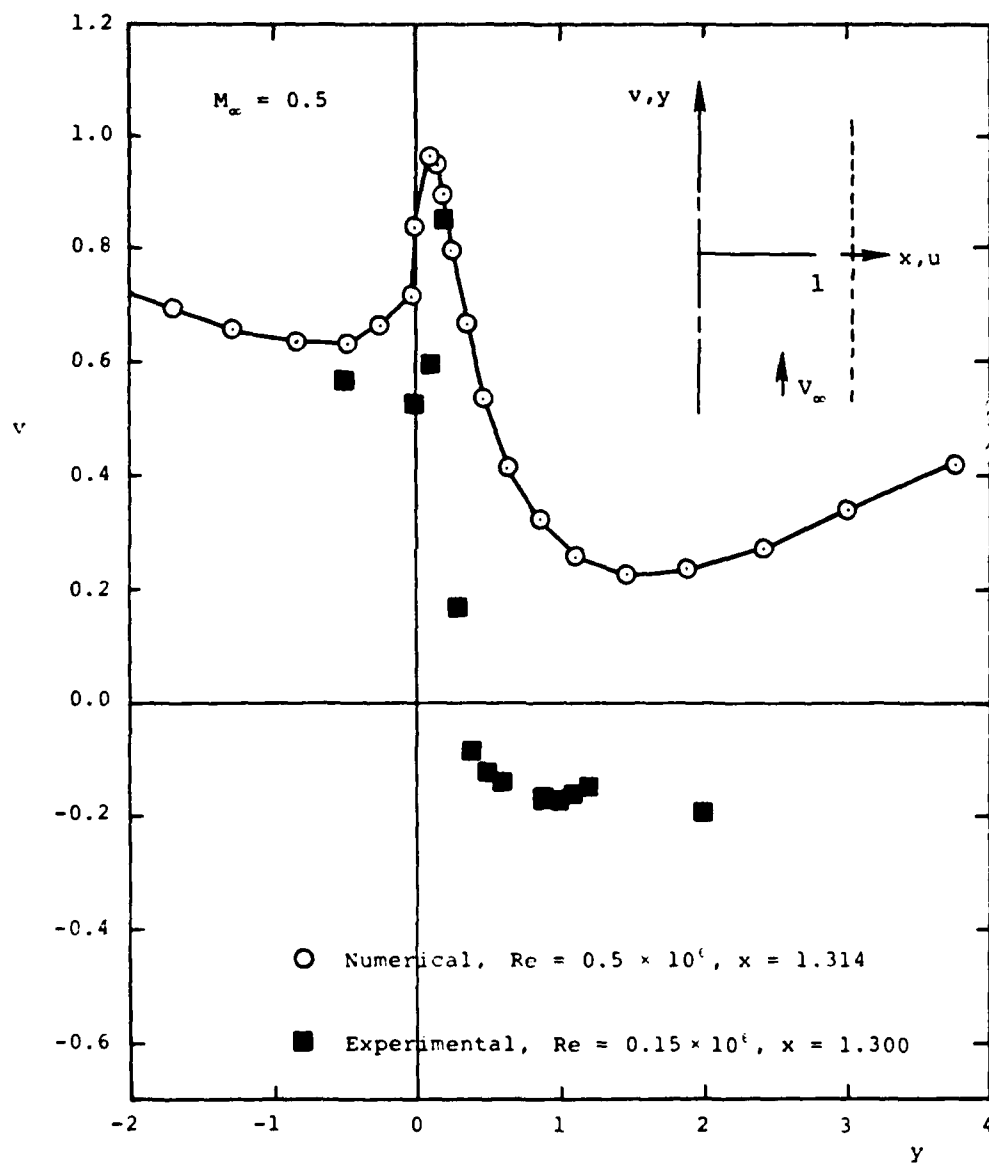


Figure 21. Axial variation of axial velocity at $x \approx 1.3$.

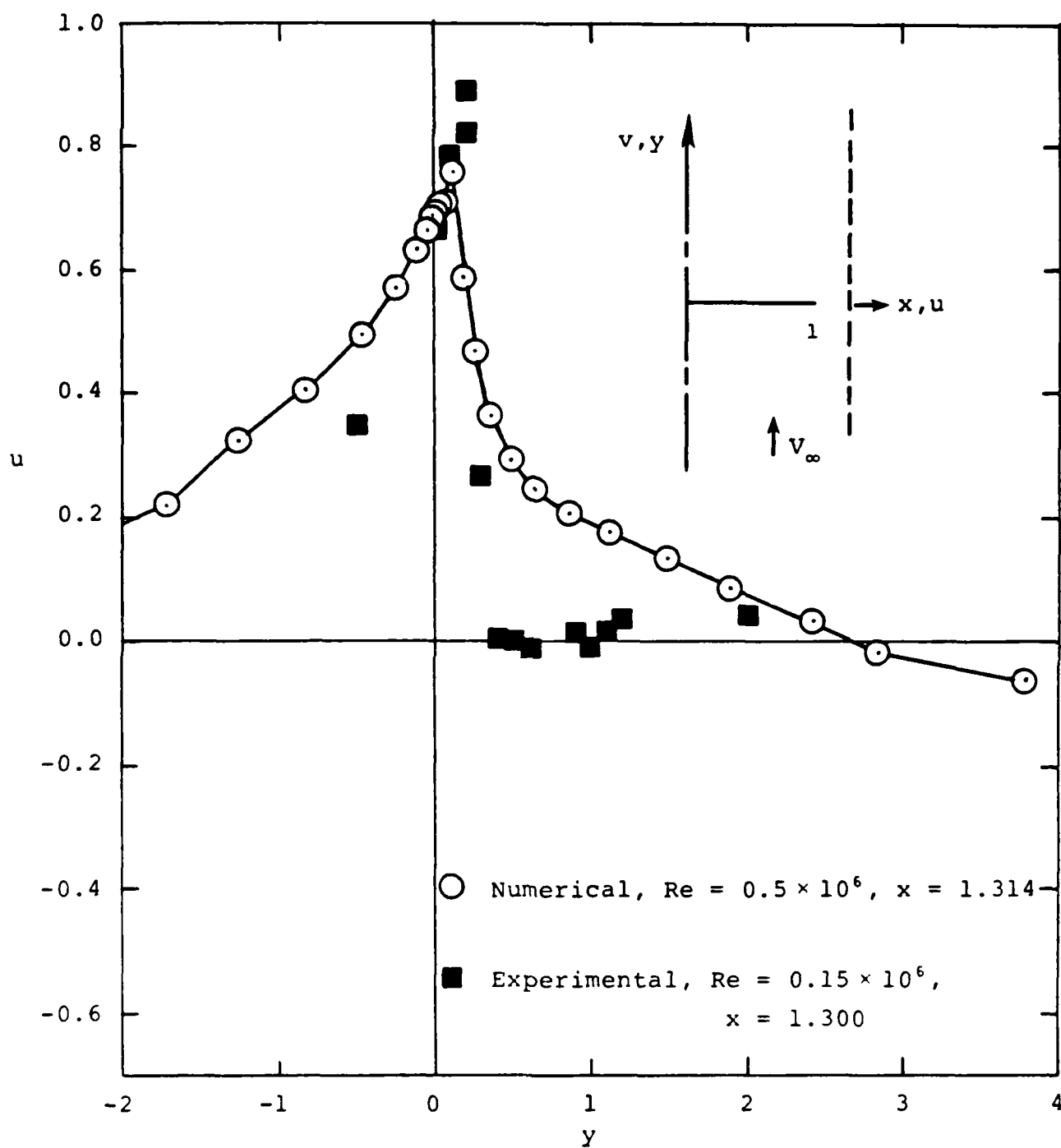


Figure 22. Axial variation of spanwise velocity at $x \approx 1.3$.

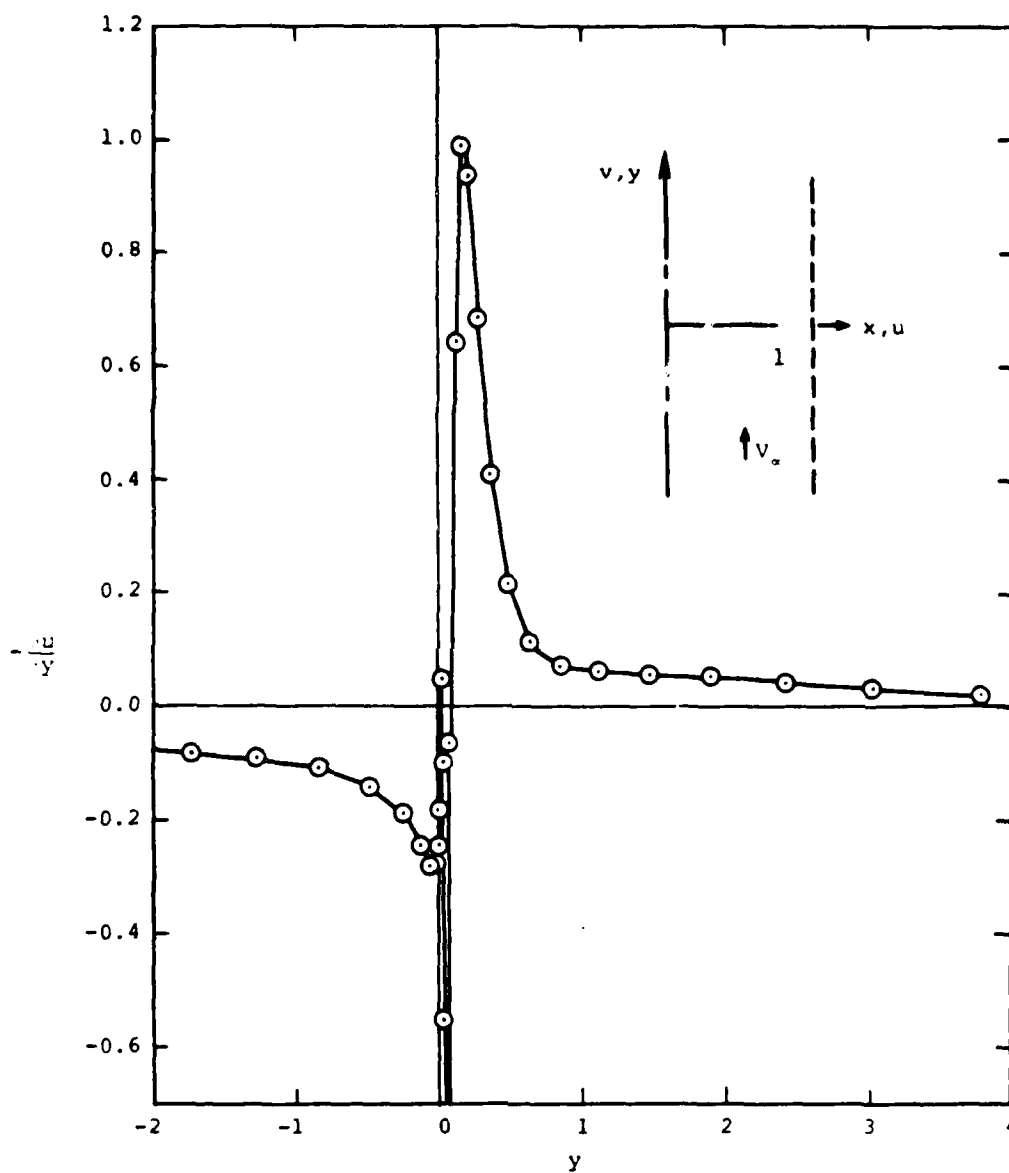


Figure 23. Axial gradient of spanwise velocity at $x = 1.3$.

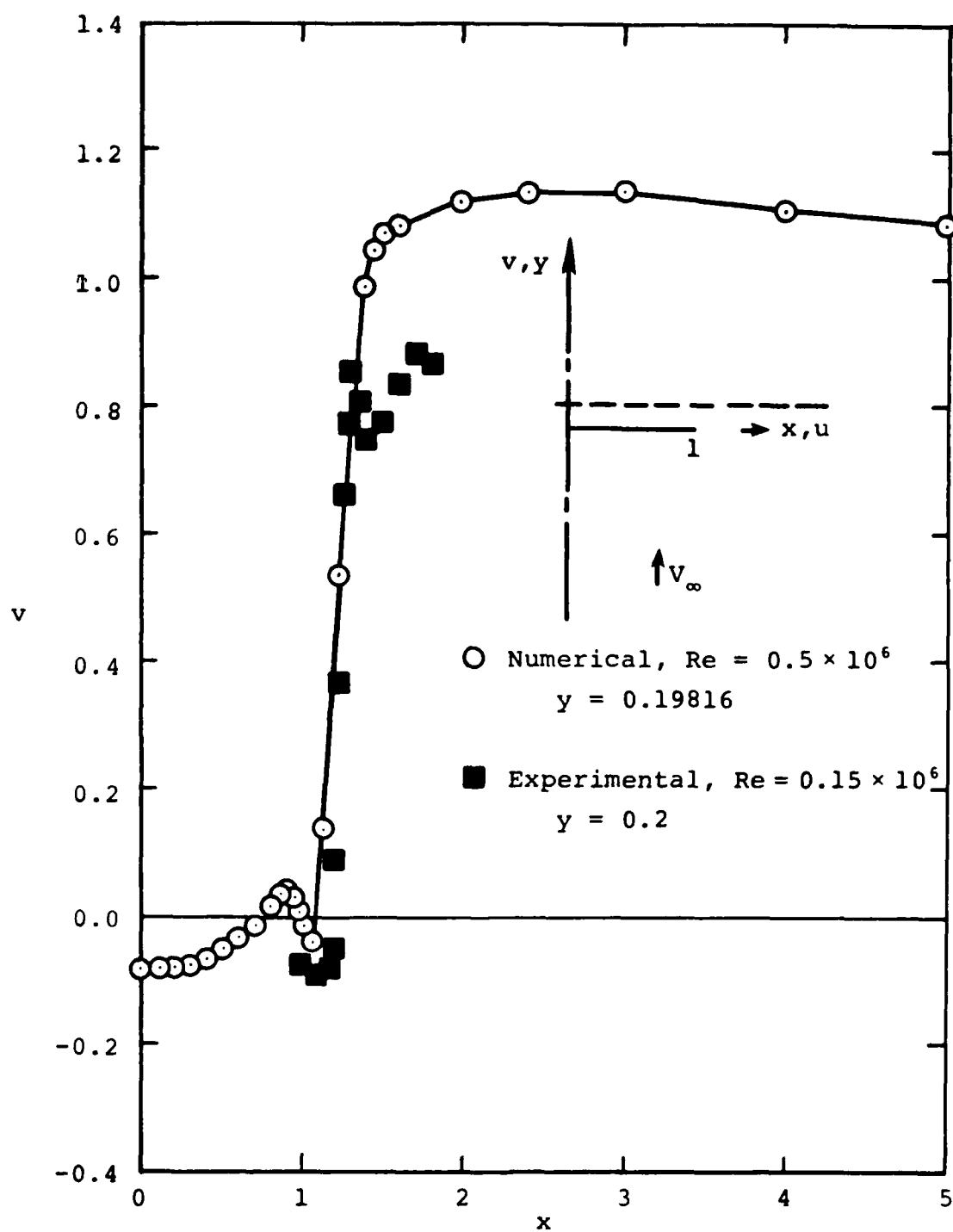


Figure 24. Spanwise variation of axial velocity at $y \approx 0.2$.

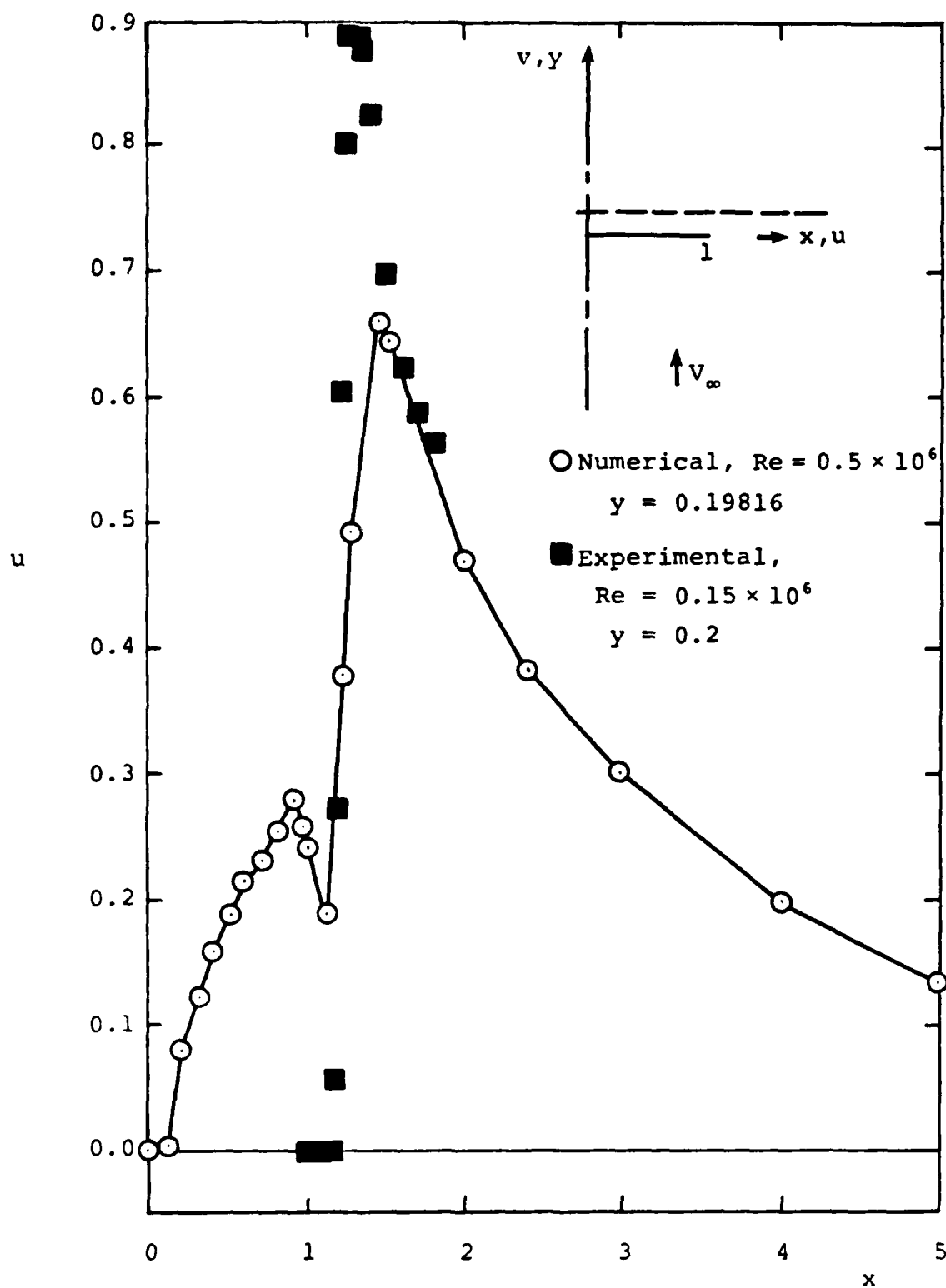


Figure 25. Spanwise variation of spanwise velocity at $y = 0.2$.

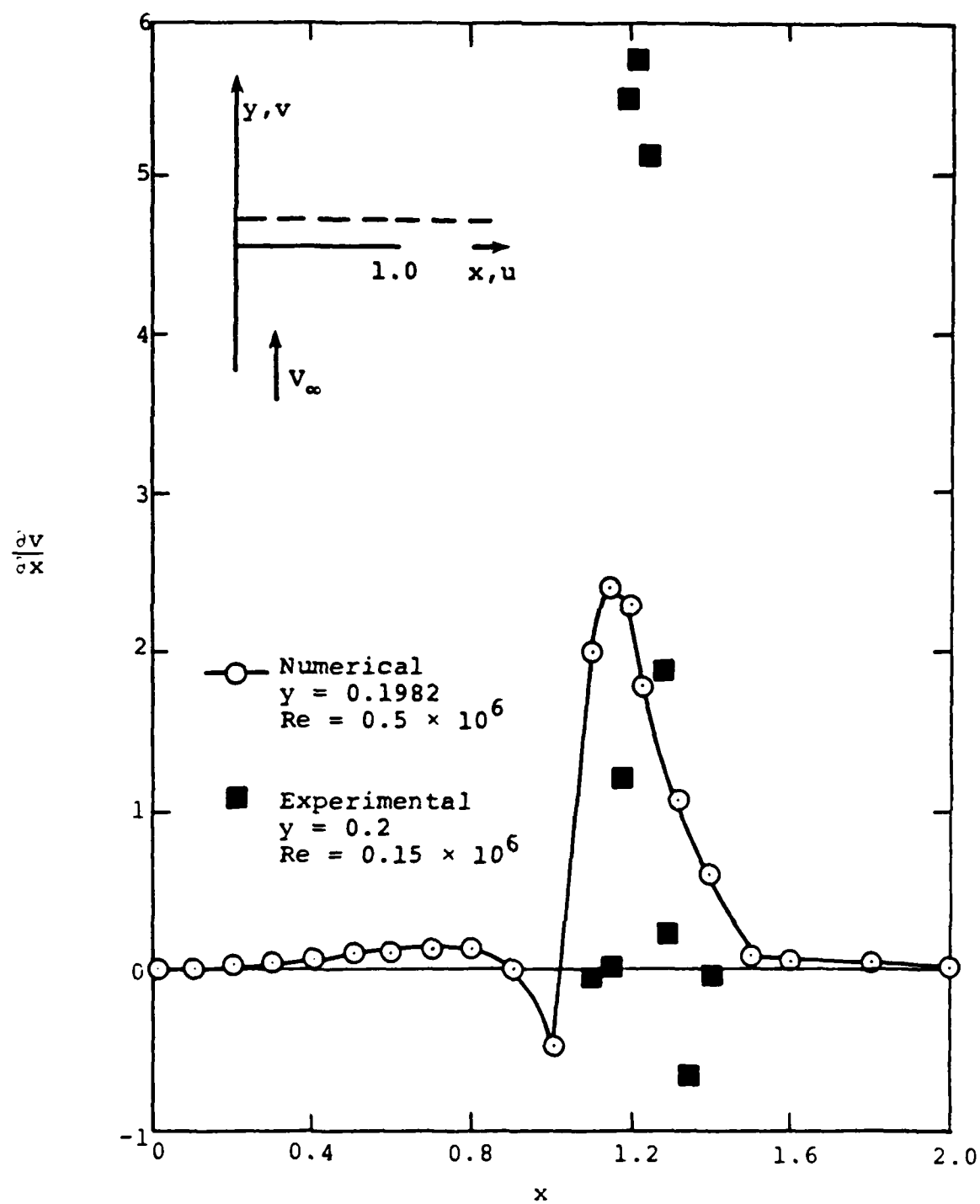


Figure 26. Spanwise gradient of axial velocity.

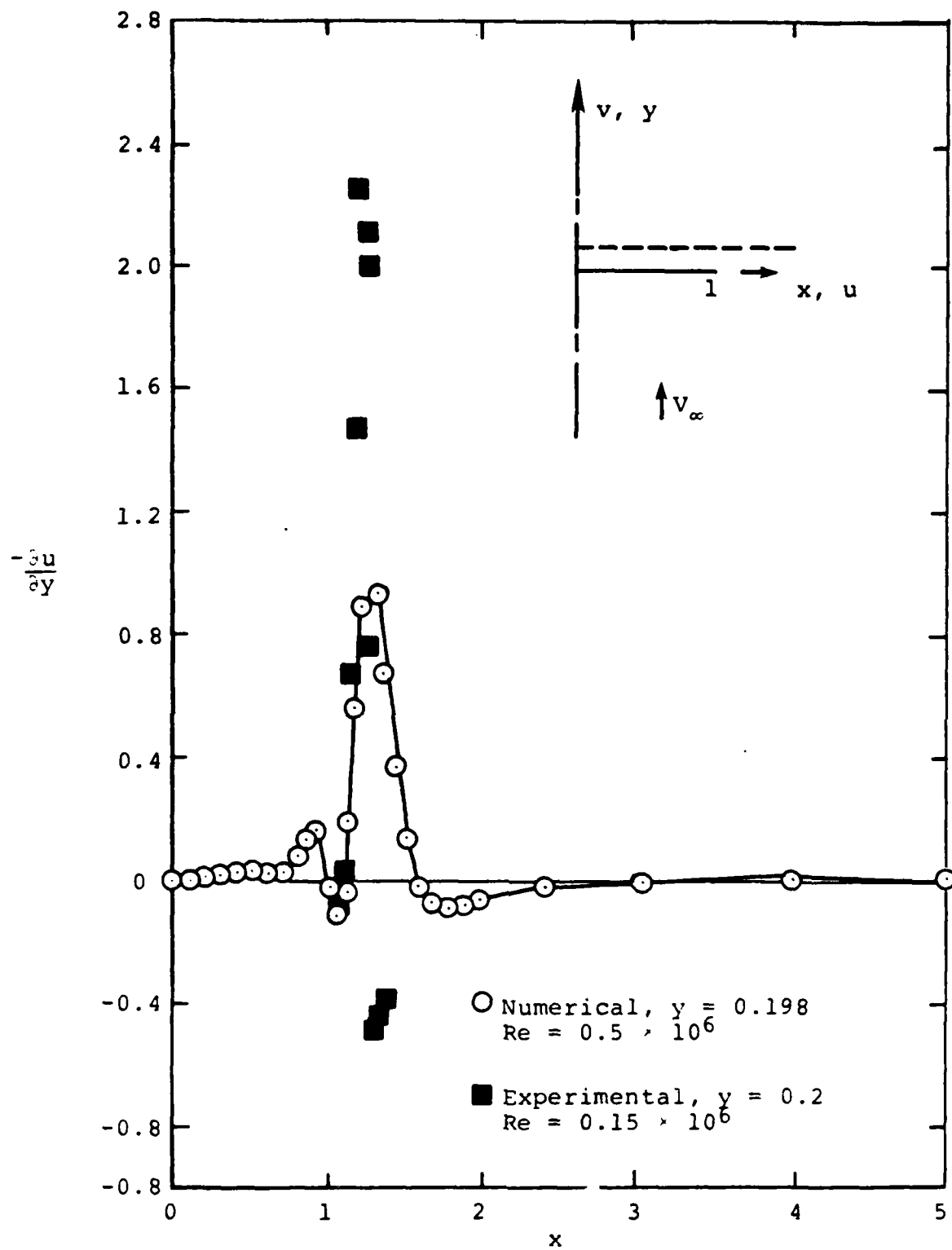


Figure 27. Axial gradient of spanwise velocity at $y \approx 0.2$.

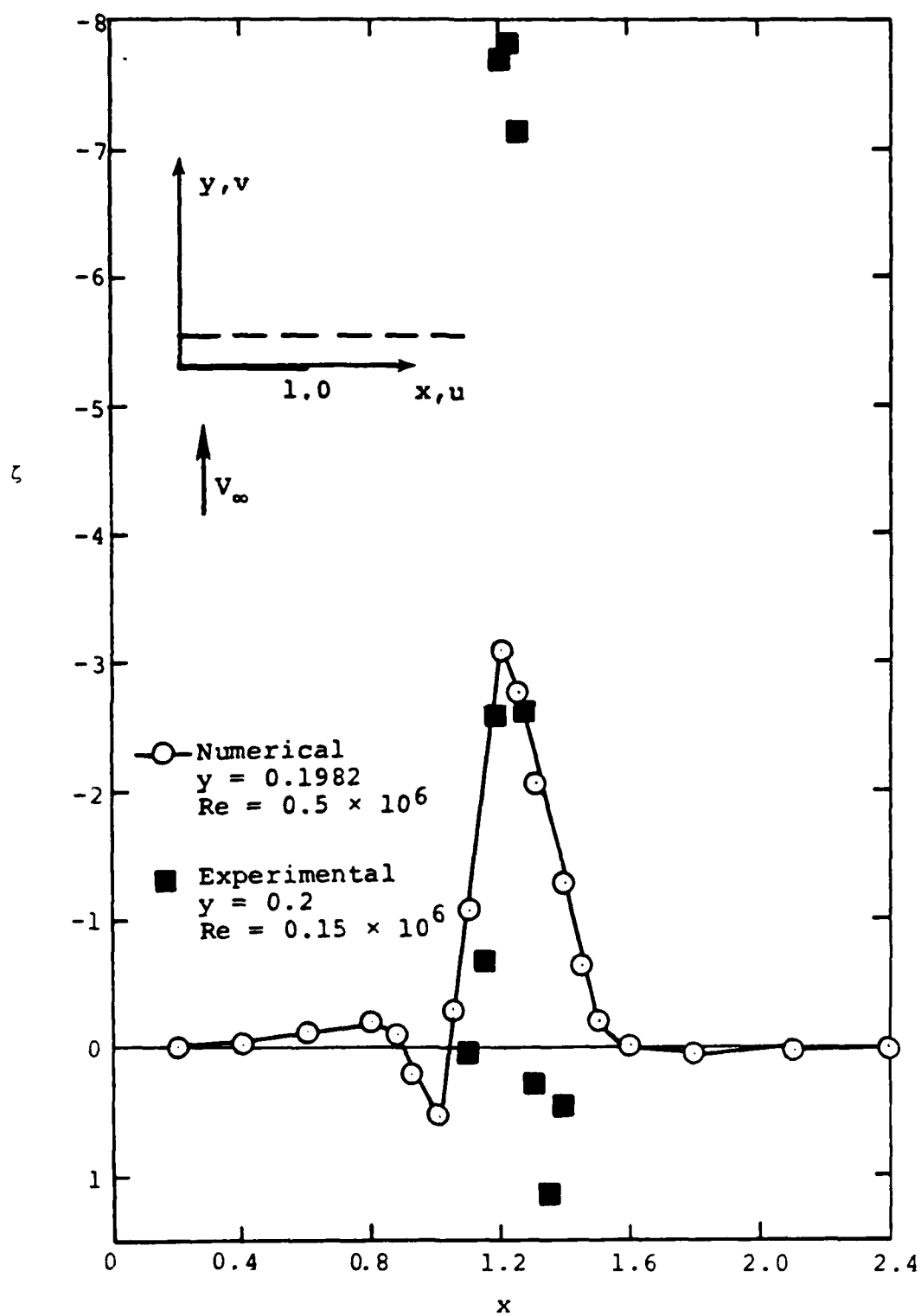


Figure 28. Spanwise variation of vorticity at $y \approx 0.2$.

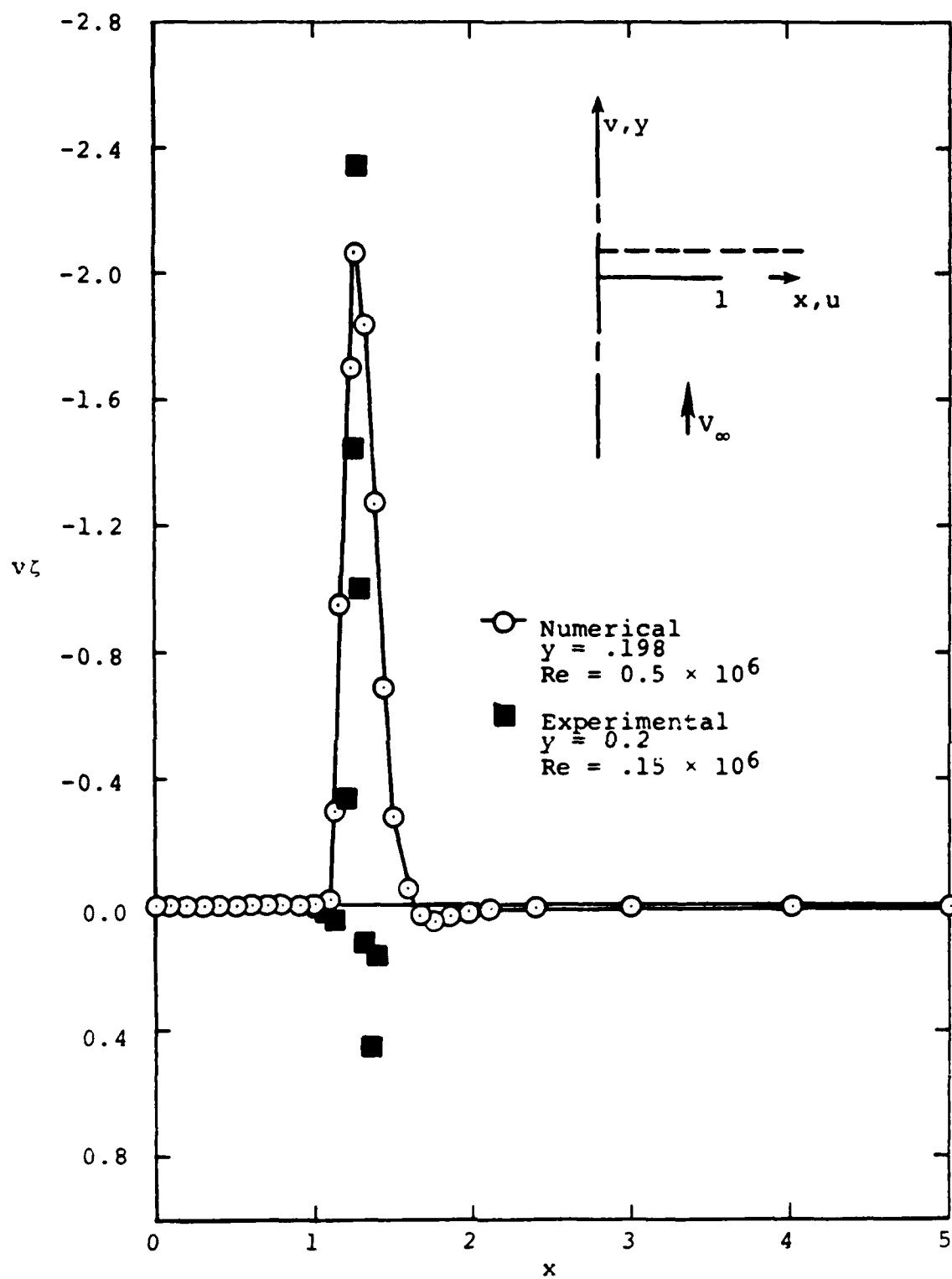


Figure 29. Vorticity transport rate at $y \approx 0.2$.

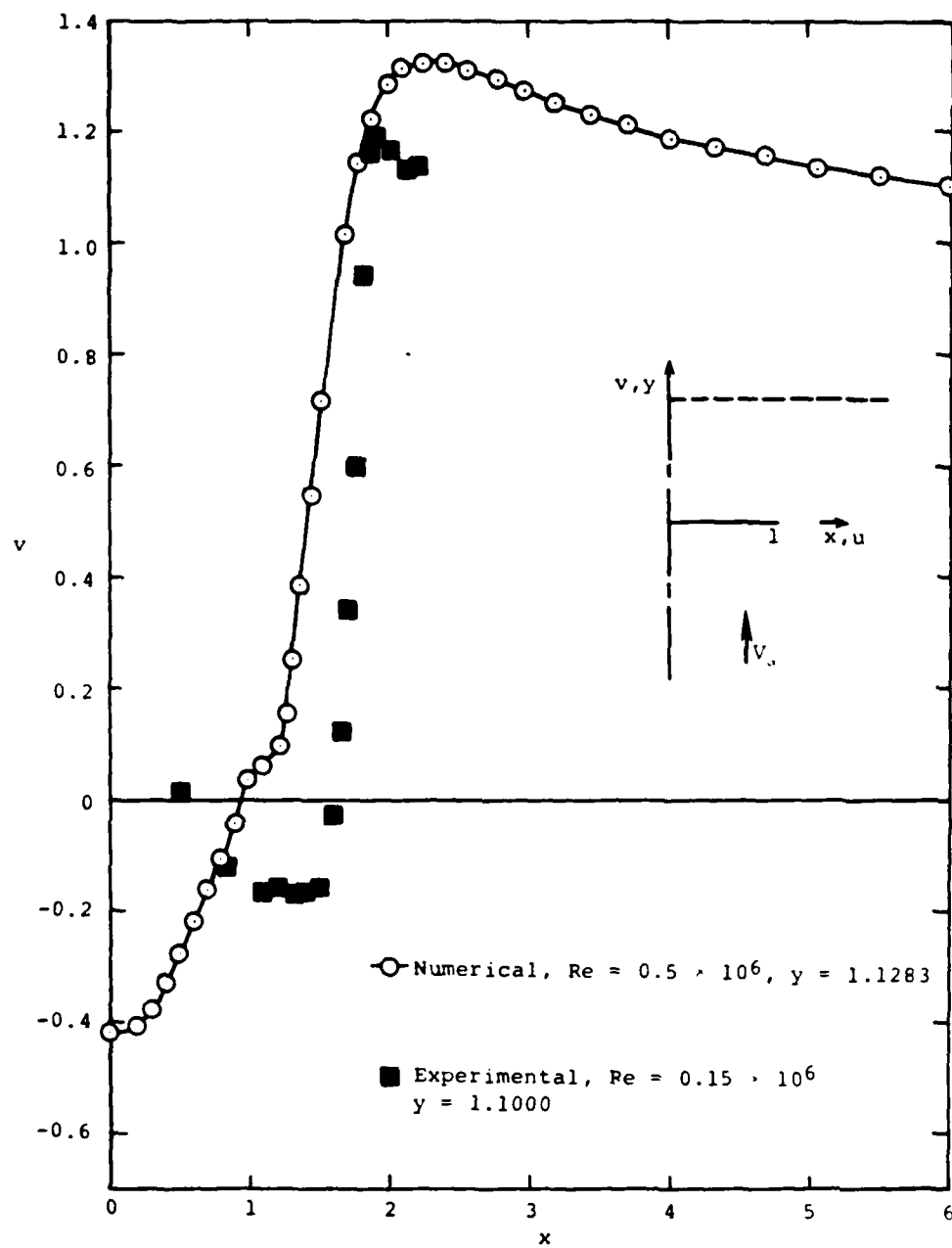


Figure 30. Axial velocity profile at $y = 1.1$.

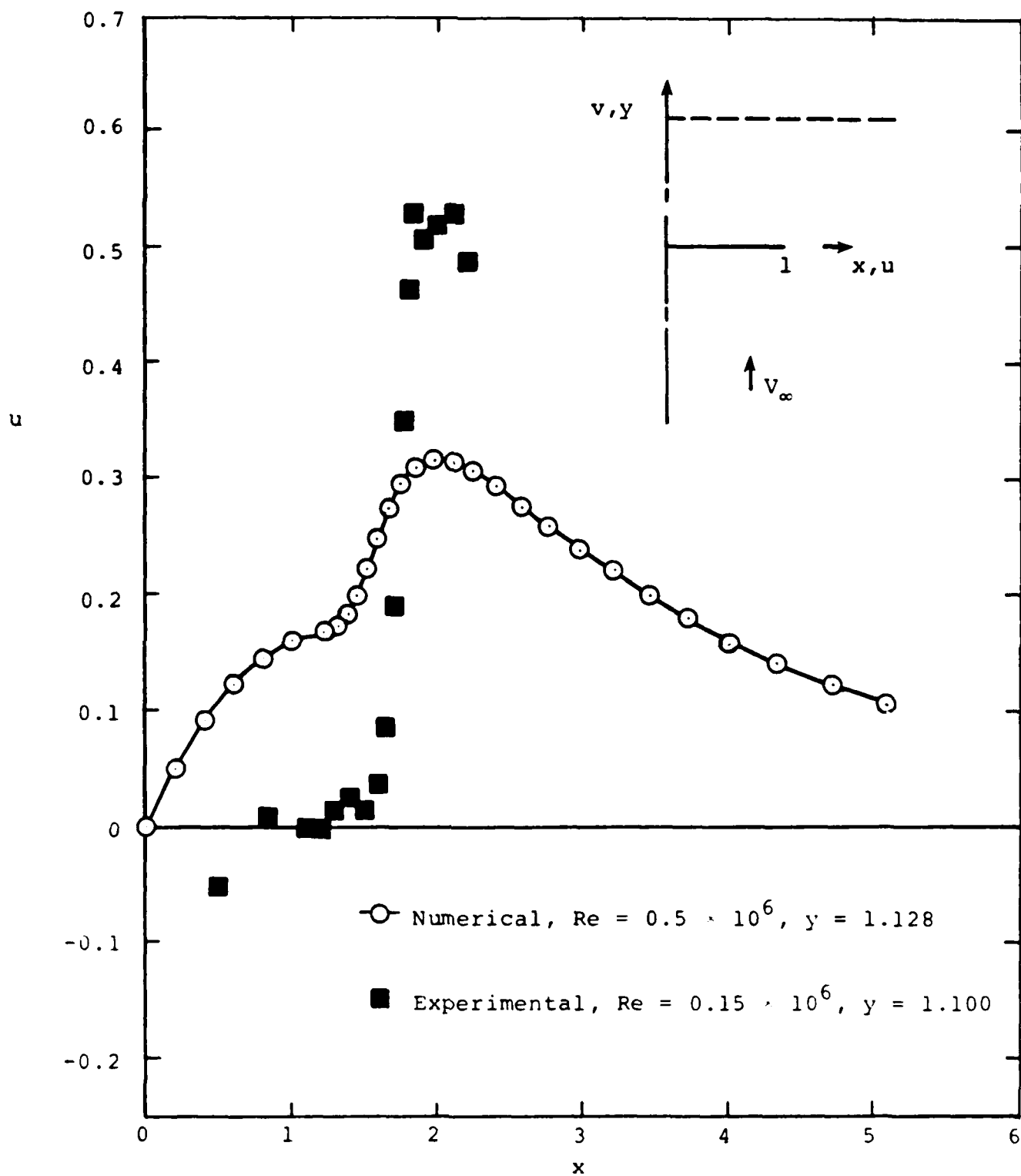


Figure 31. Spanwise velocity profile at $y \approx 1.1$.

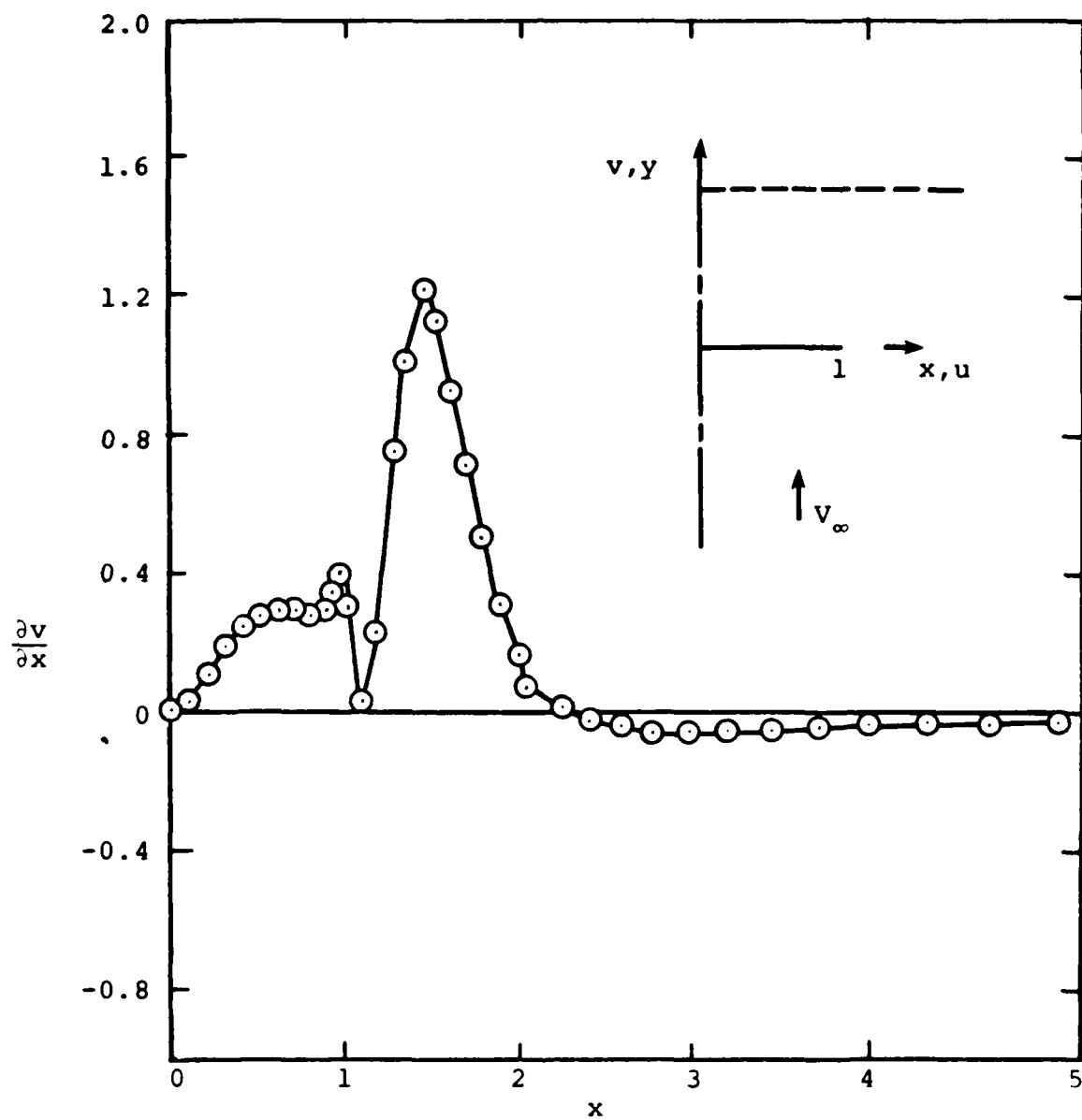


Figure 32. Axial velocity gradient at $y = 1.128$.

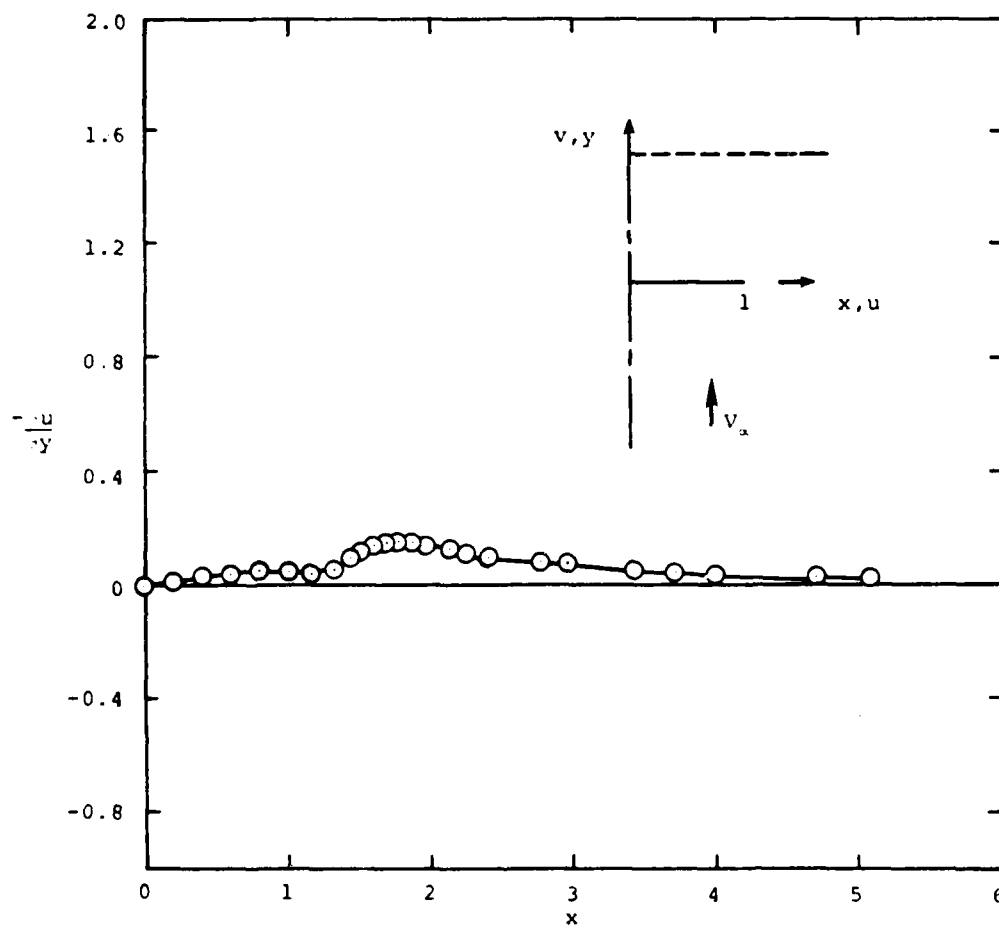


Figure 33. Spanwise velocity gradient at $y = 1.128$.

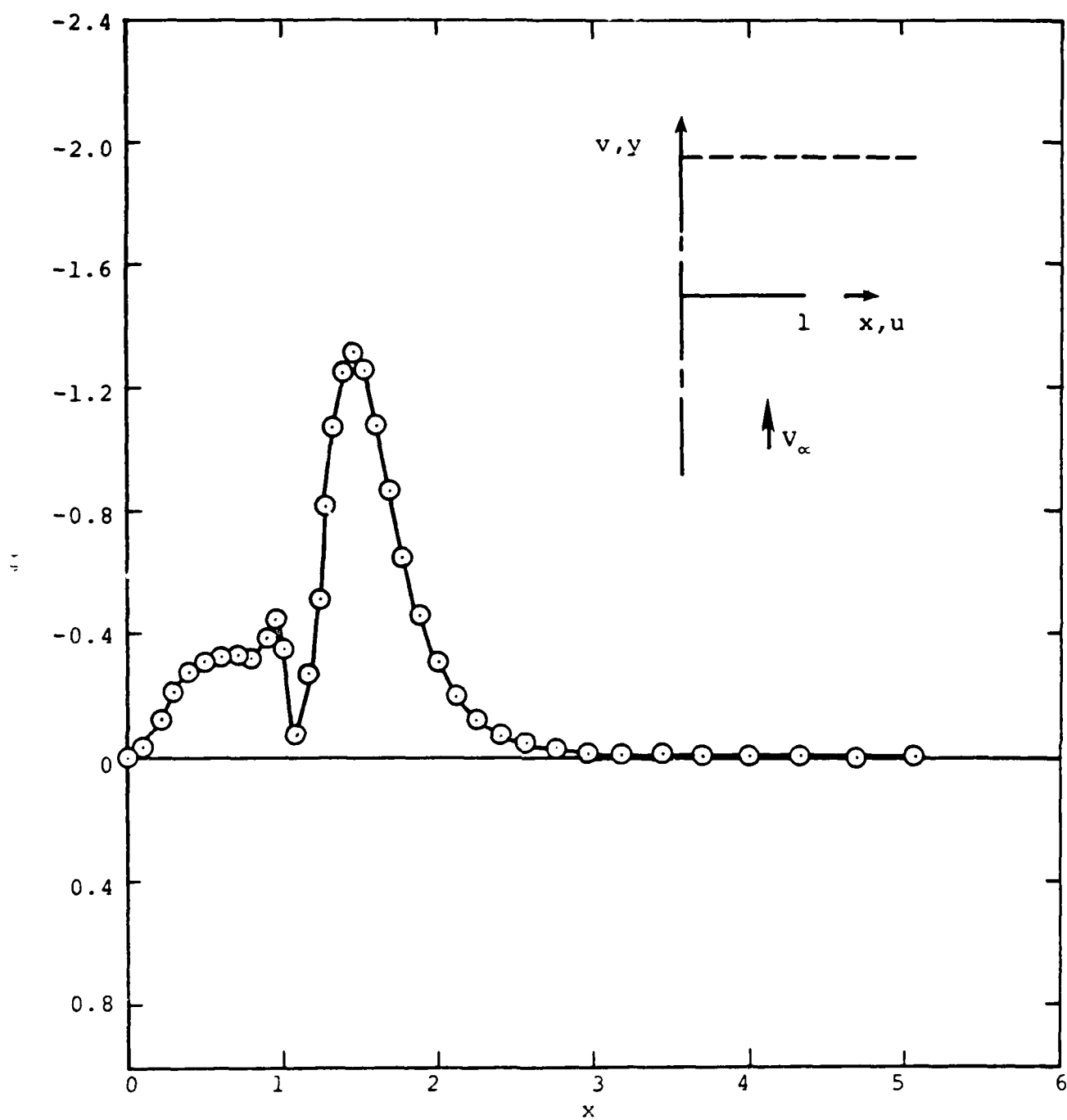


Figure 34. Spanwise variation of vorticity at $y = 1.128$.

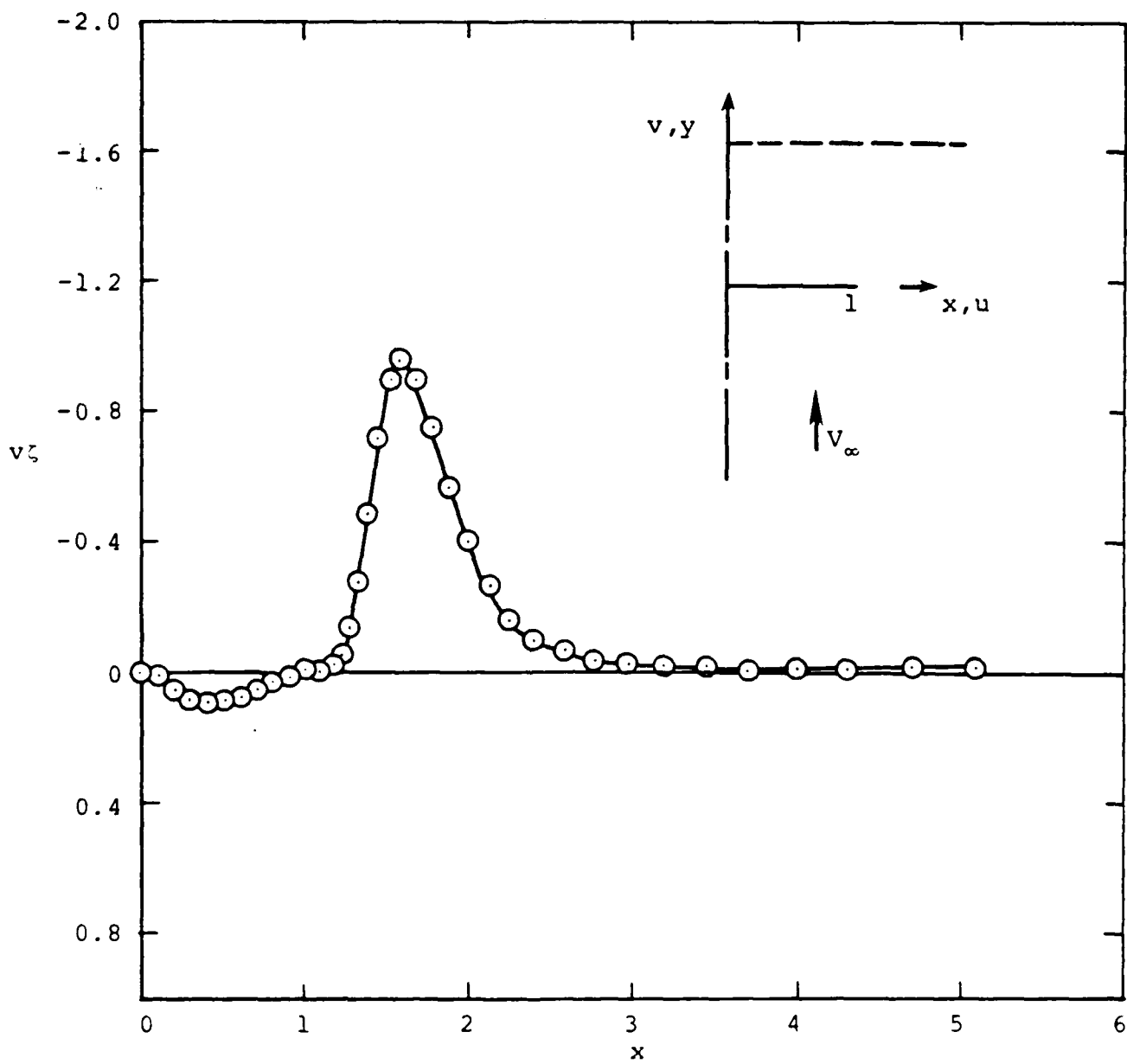


Figure 35. Vorticity transport rate at $y = 1.128$.

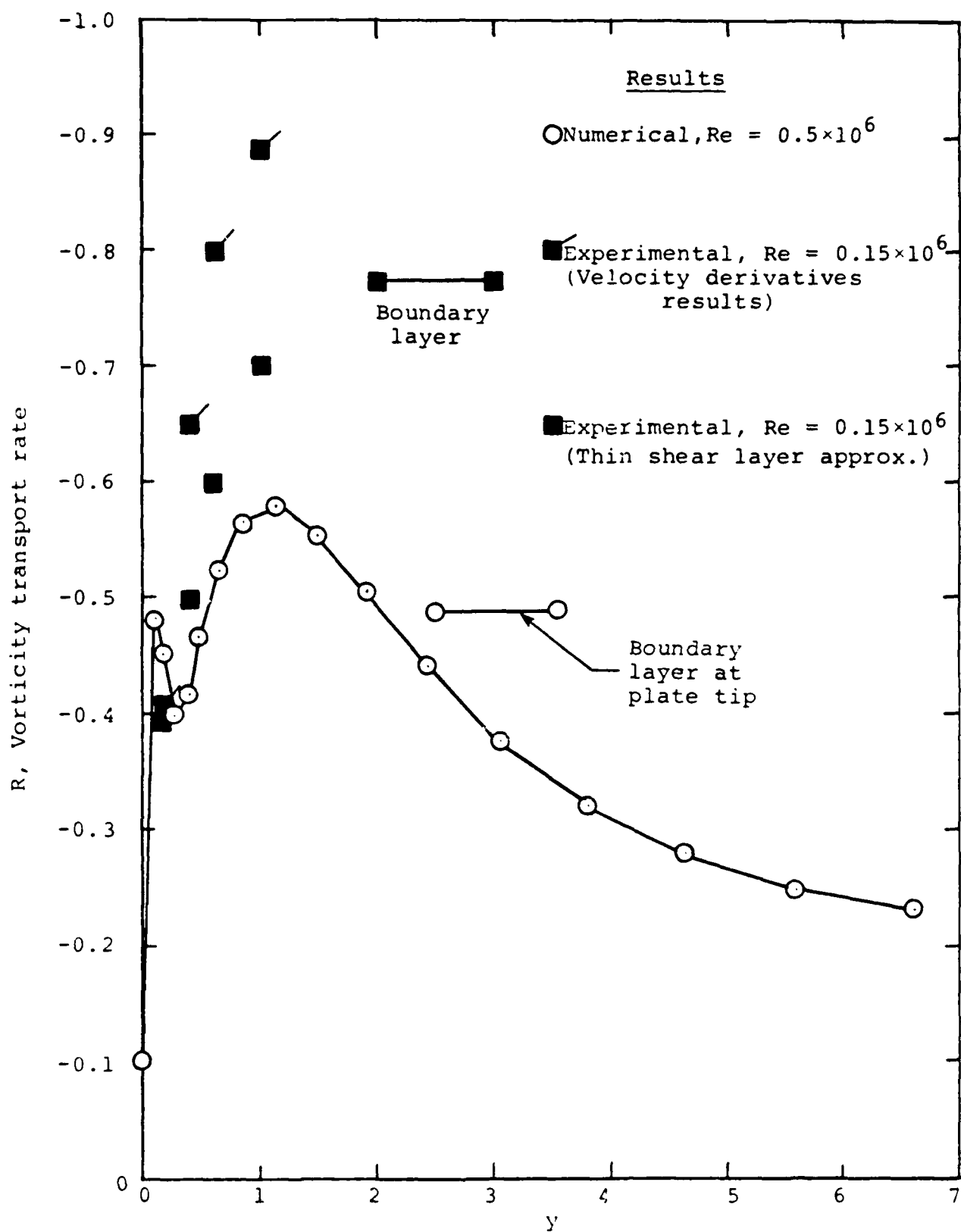


Figure 36. Comparisons of vorticity transport rates.

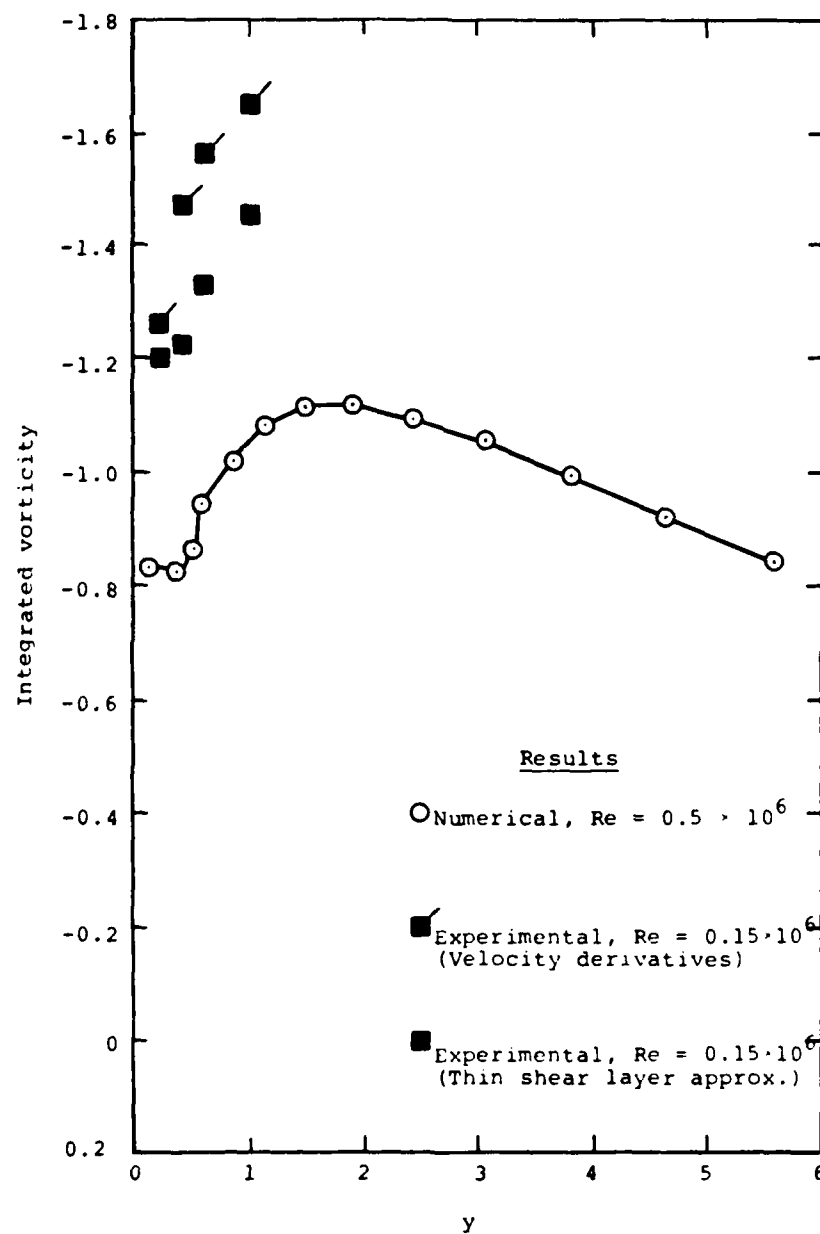


Figure 37. Spanwise integrated vorticity.

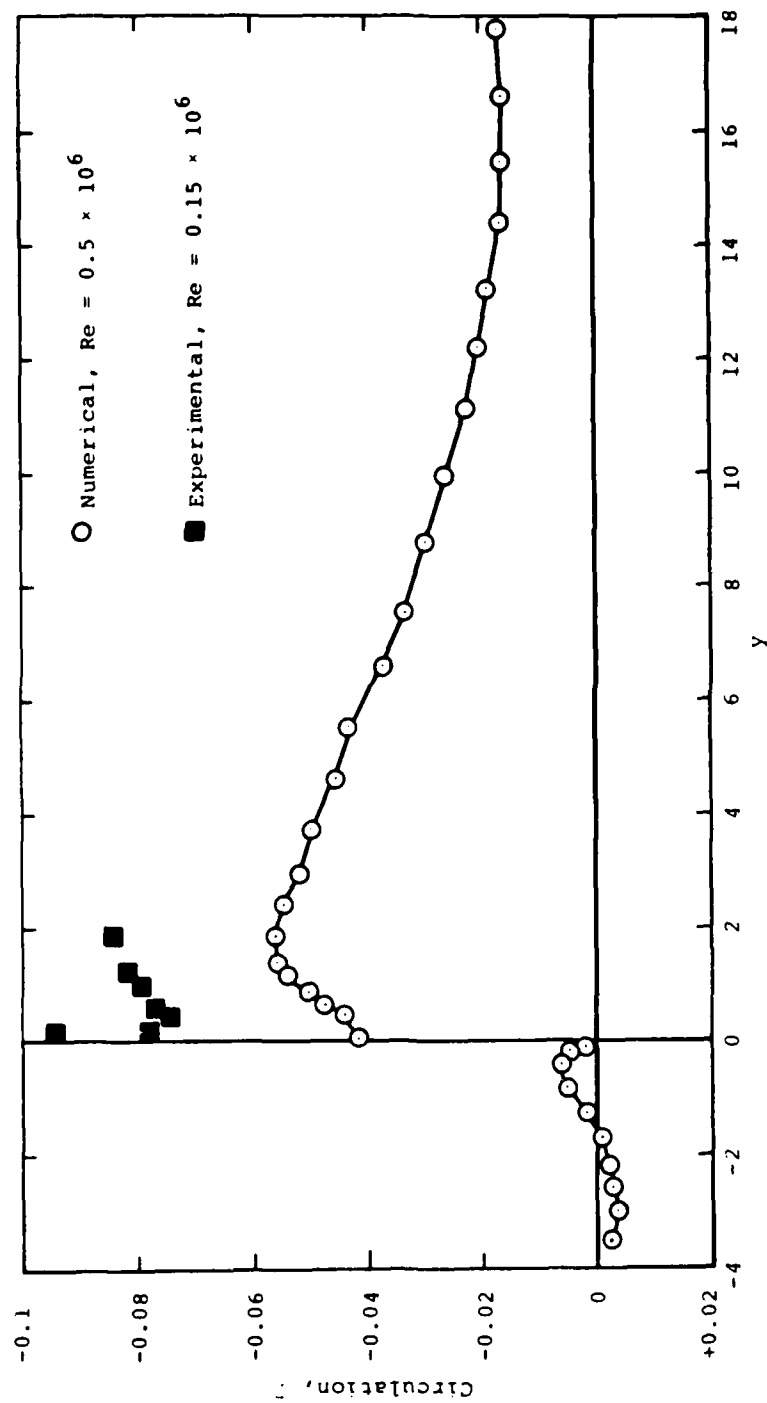


Figure 38. Contour integration results for circulation, $M_\infty = 0.5$.

TWO-DIM STRAKE $M = .5$ $\alpha = 90$

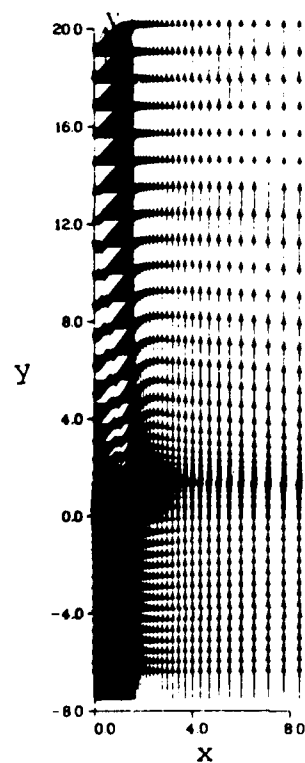


Figure 39. Axial velocity vector plots.

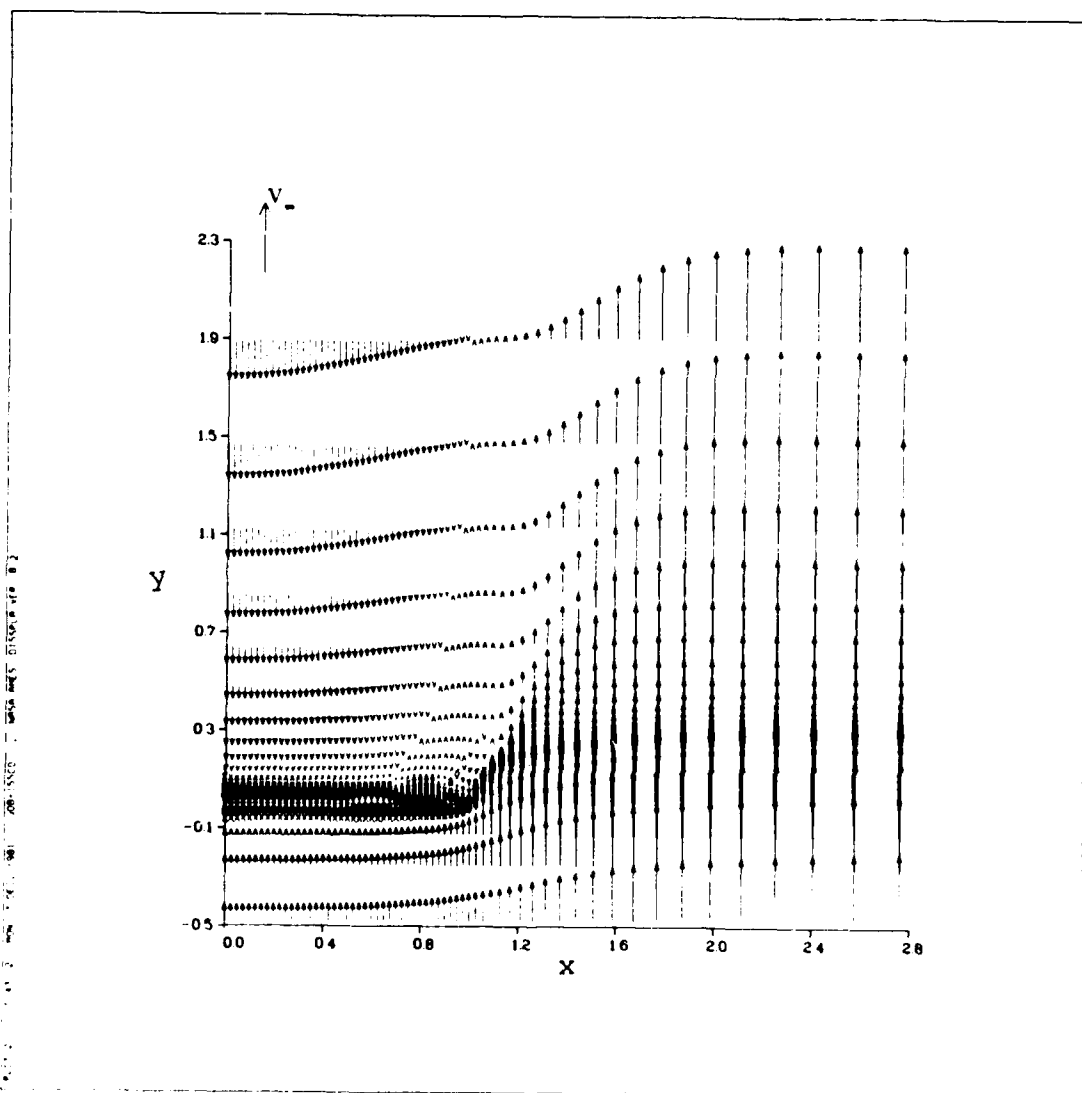


Figure 40. Detail of axial velocity vector plot

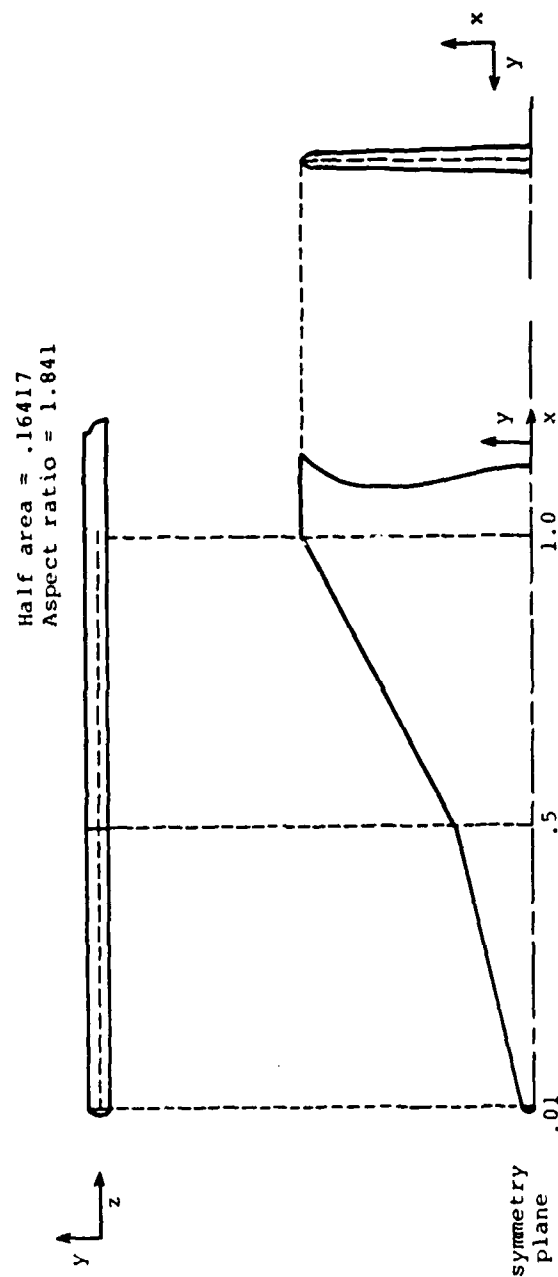


Figure 41. Wing configuration.

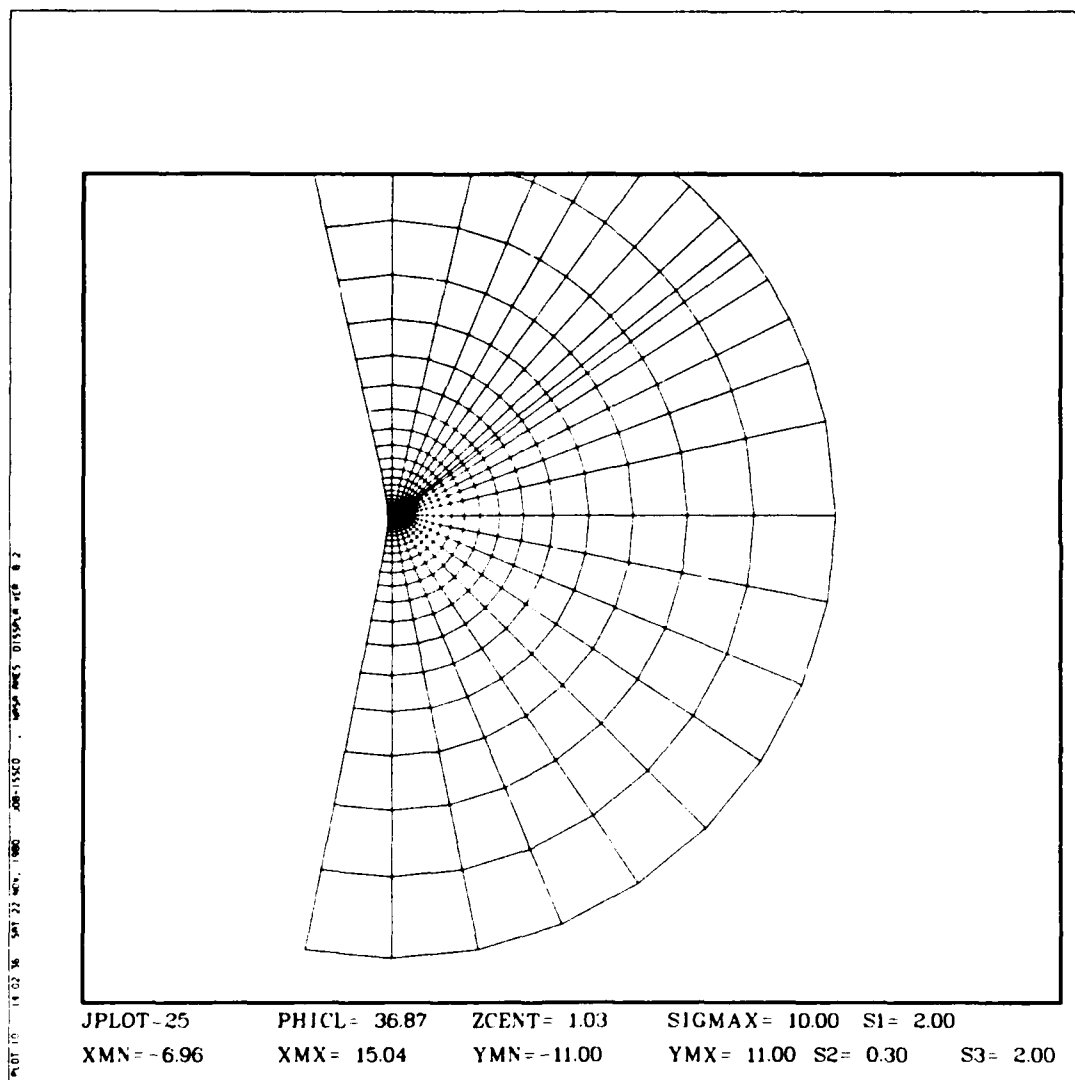


Figure 42. Crossflow plane elliptic coordinates.

Front and rear surfaces
are plane of symmetry

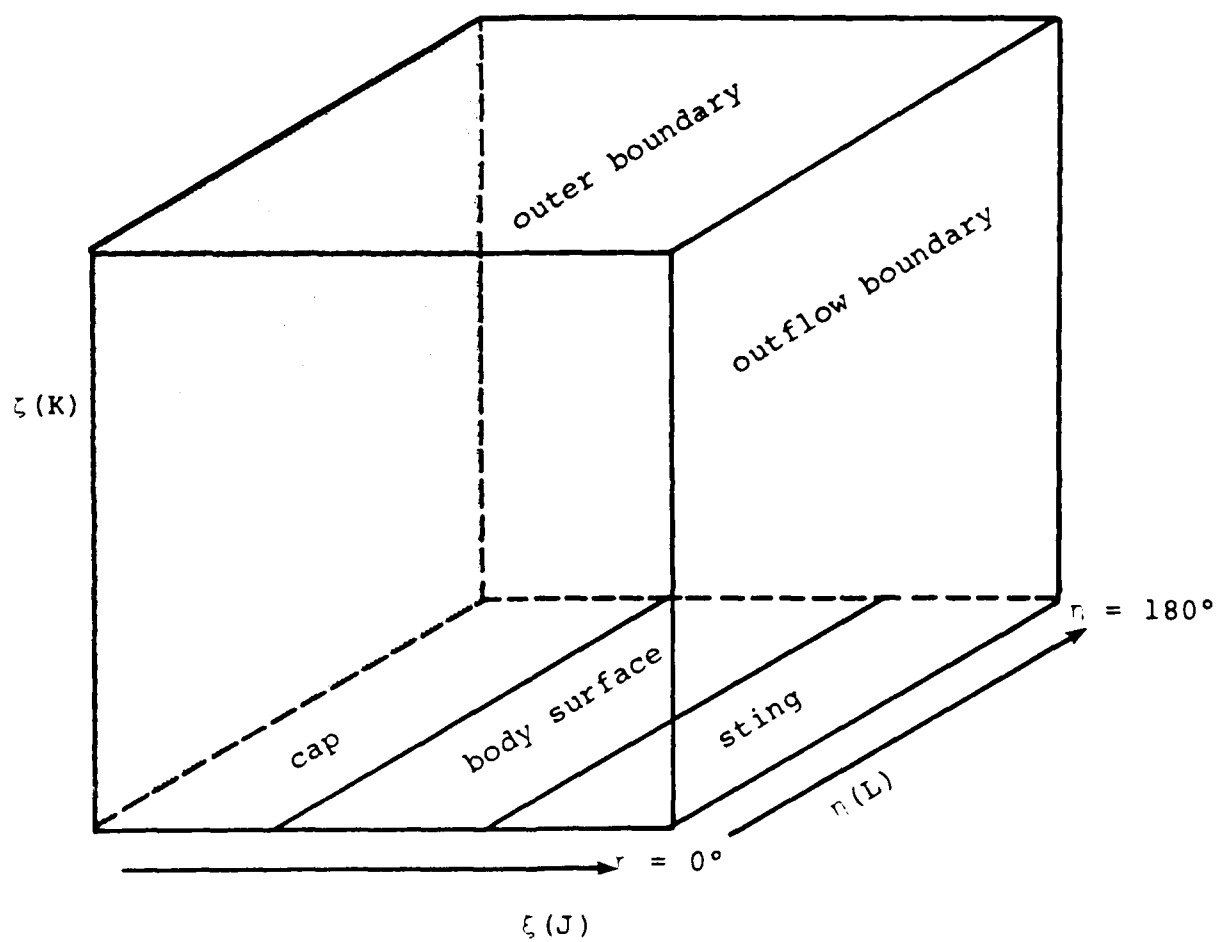


Figure 43.- Computational domain.

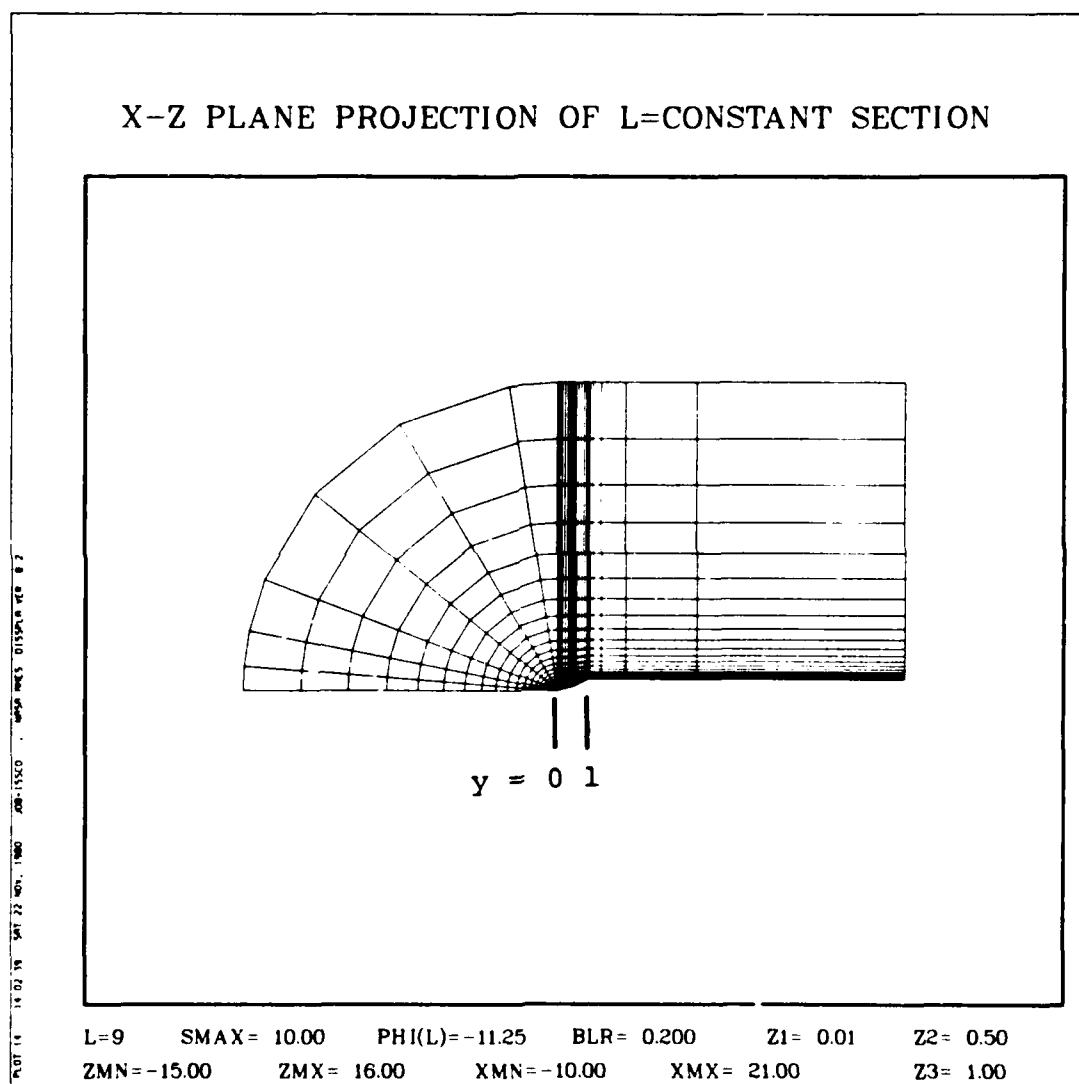


Figure 44. Mesh arrangement in $y = 0$ plane.

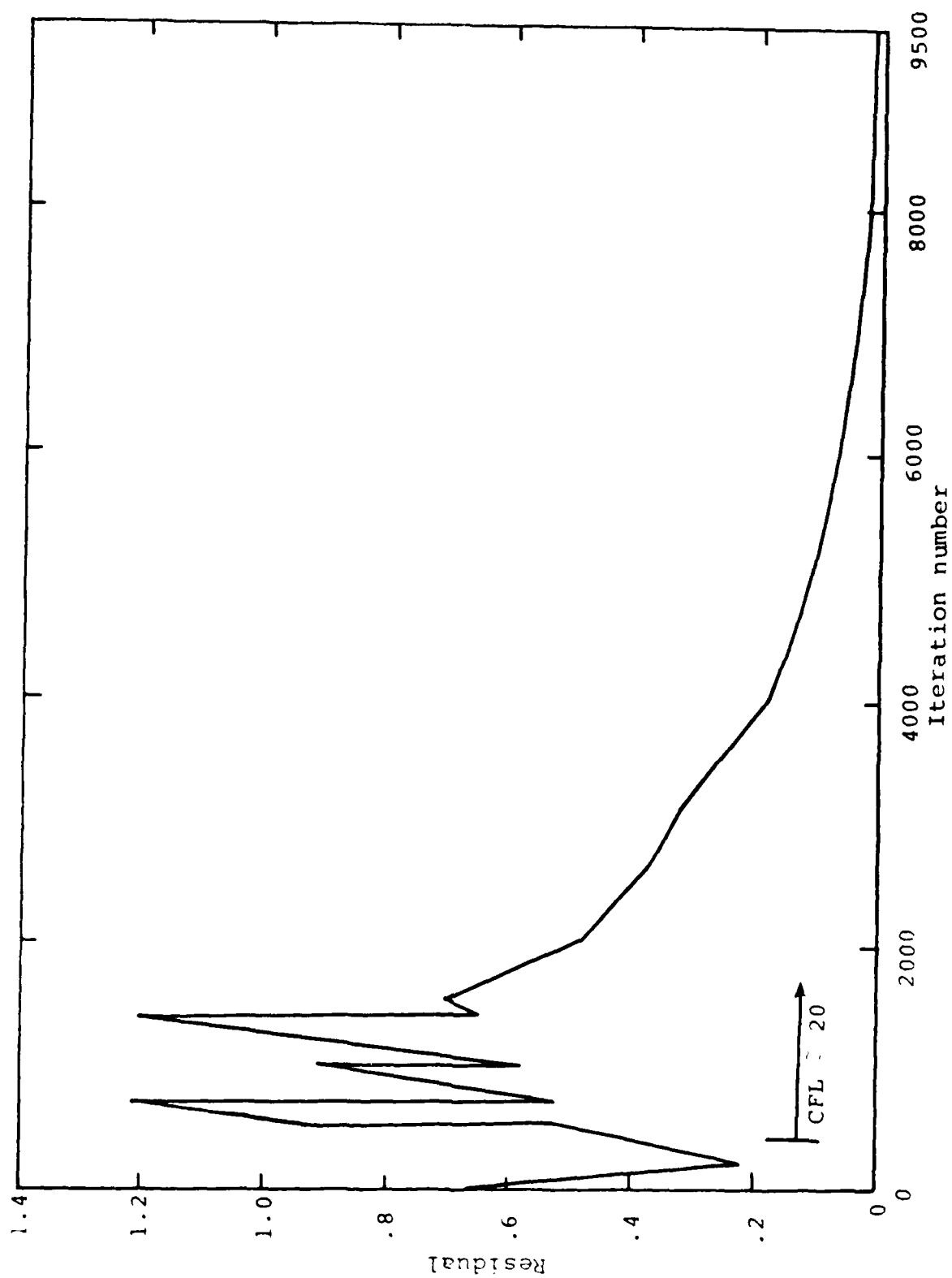


Figure 45. Convergence history.

75°/62° DOUBLE-DELTA

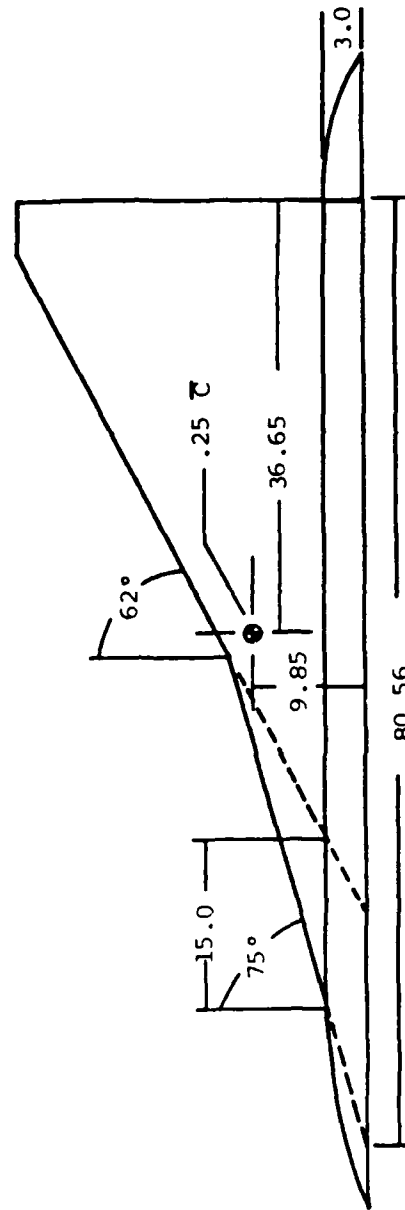
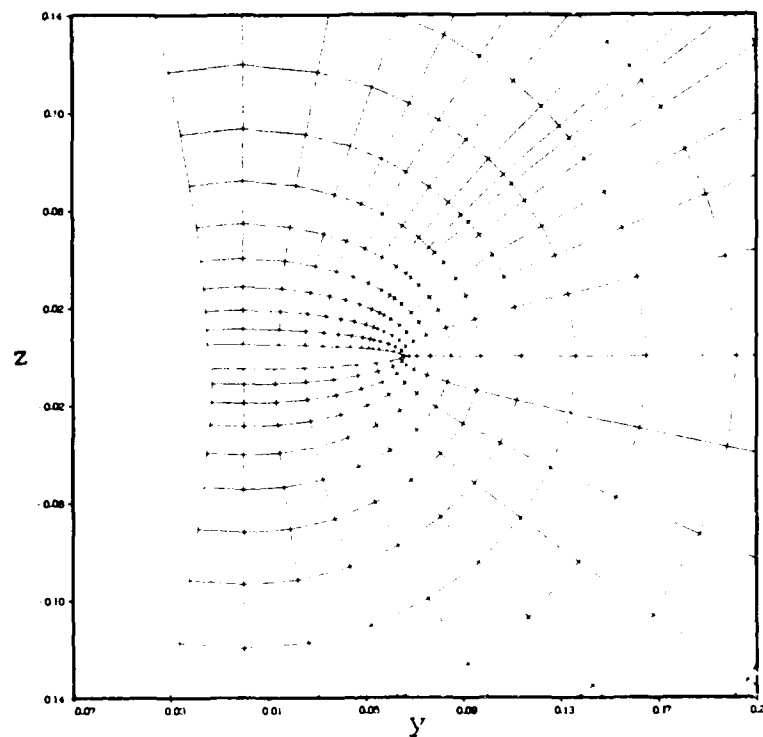


Figure 46.- Model configuration tested by Wentz and McMahon.

75 63 DOUBLE DELTA J=12 Z=.2496 B=.0669



(a) Grid plot

Figure 47. Crossflow plane characteristics at $x = .25$.

AD-A125 882

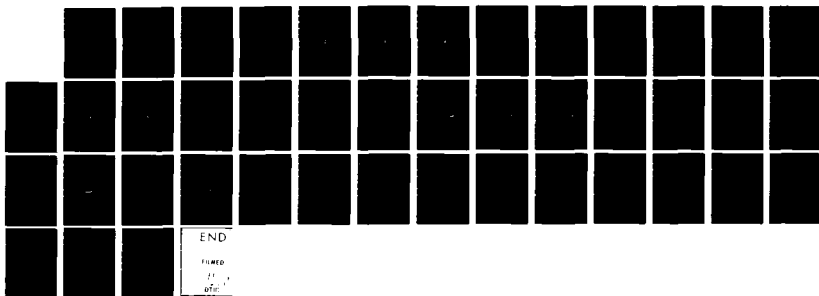
A NUMERICAL STUDY OF STRAKE AERODYNAMICS(U) NIELSEN
ENGINEERING AND RESEARCH INC MOUNTAIN VIEW CA
G D KERLICK ET AL. JUL 82 NEAR-TR-270 N00014-78-C-0388

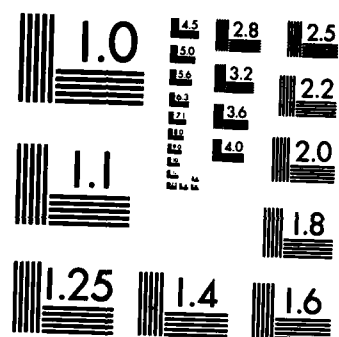
2/2

UNCLASSIFIED

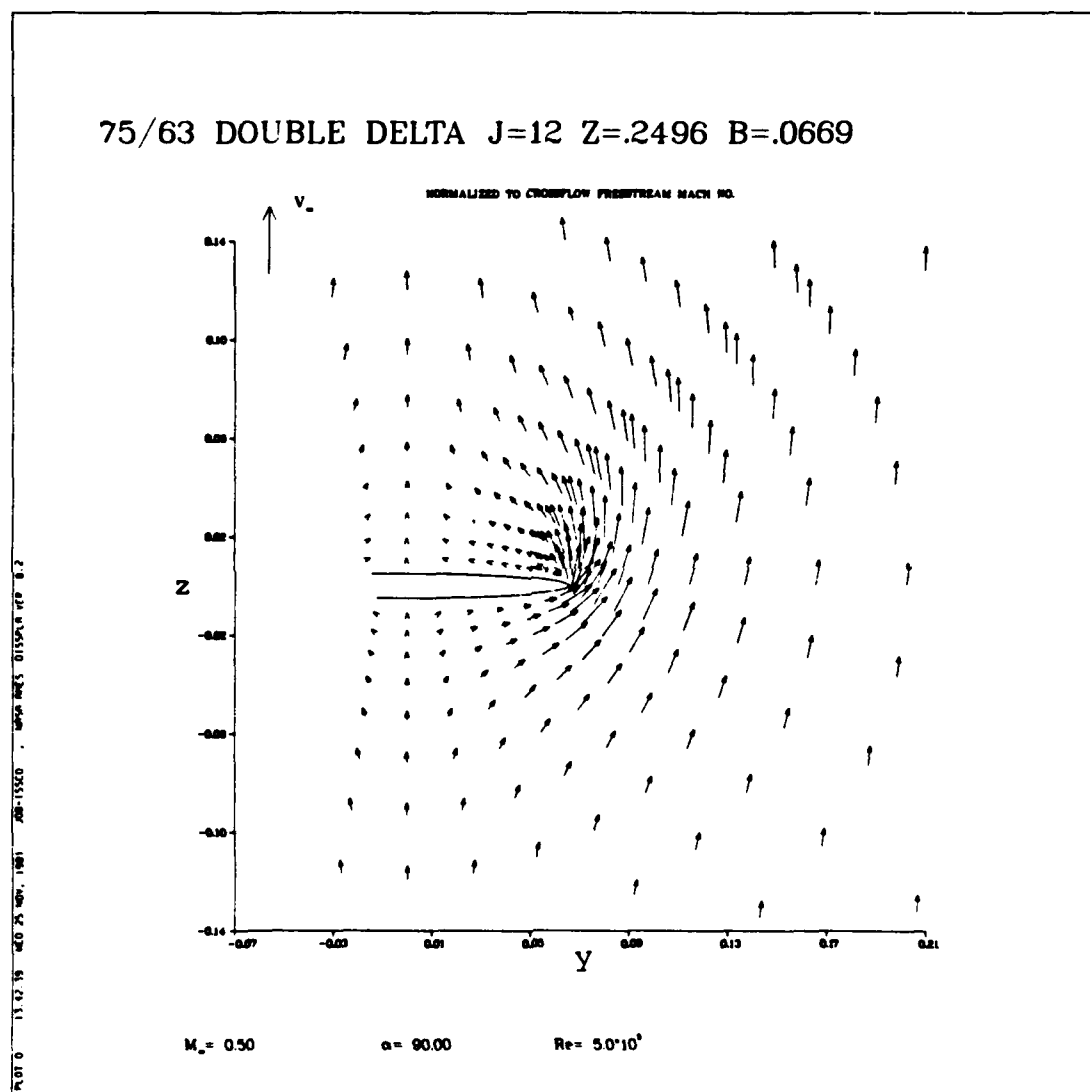
F/G 20/4

NL



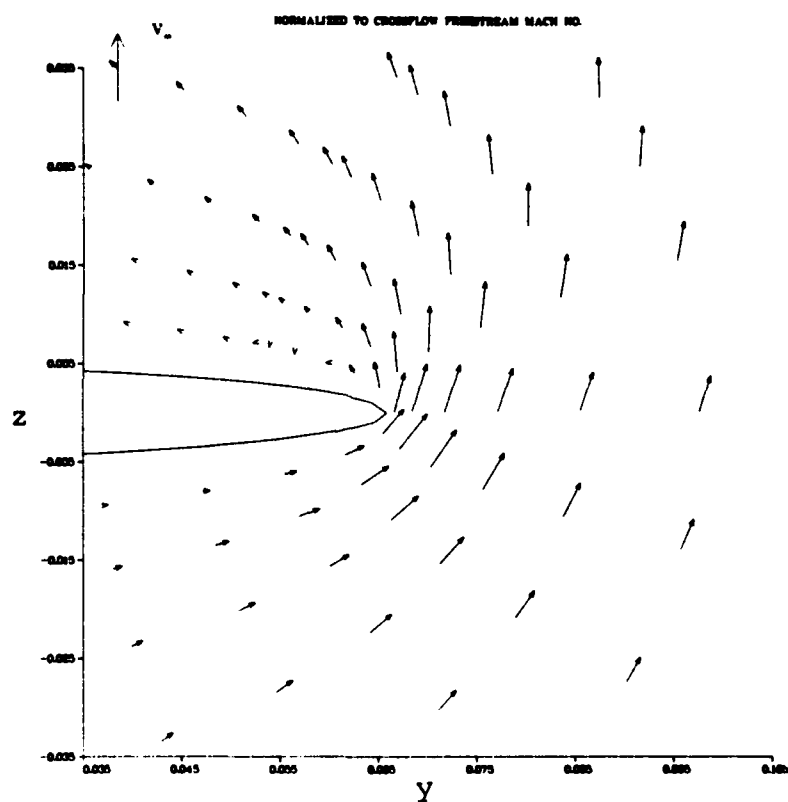


MICROCOPY RESOLUTION TEST CHART
NATIONAL BUREAU OF STANDARDS-1963-A



(b) Crossflow plane velocity vectors
Figure 47. (Continued).

75/63 DOUBLE DELTA J=12 Z=.2496 B=.0669

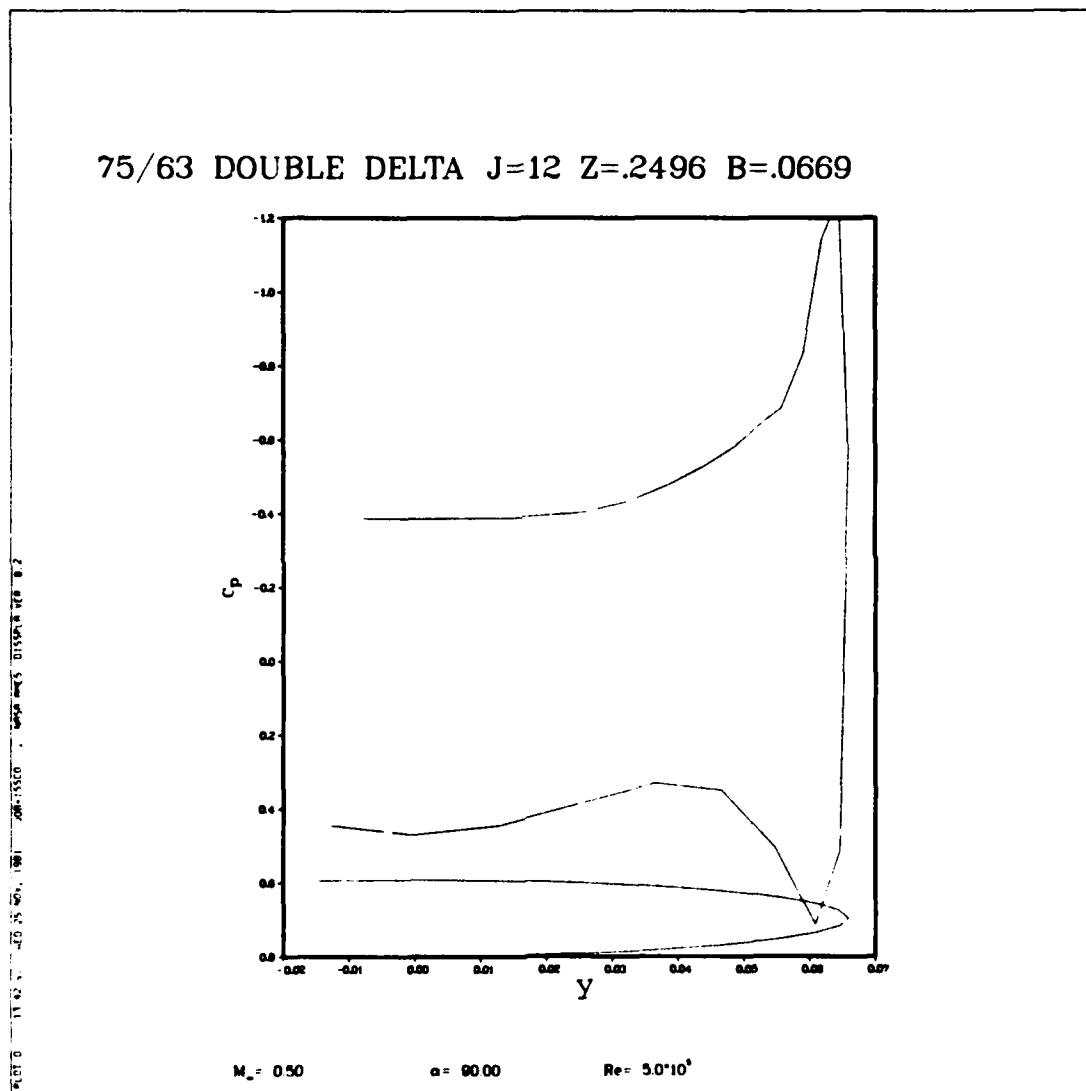


$M_\infty = 0.50$

$\alpha = 90.00$

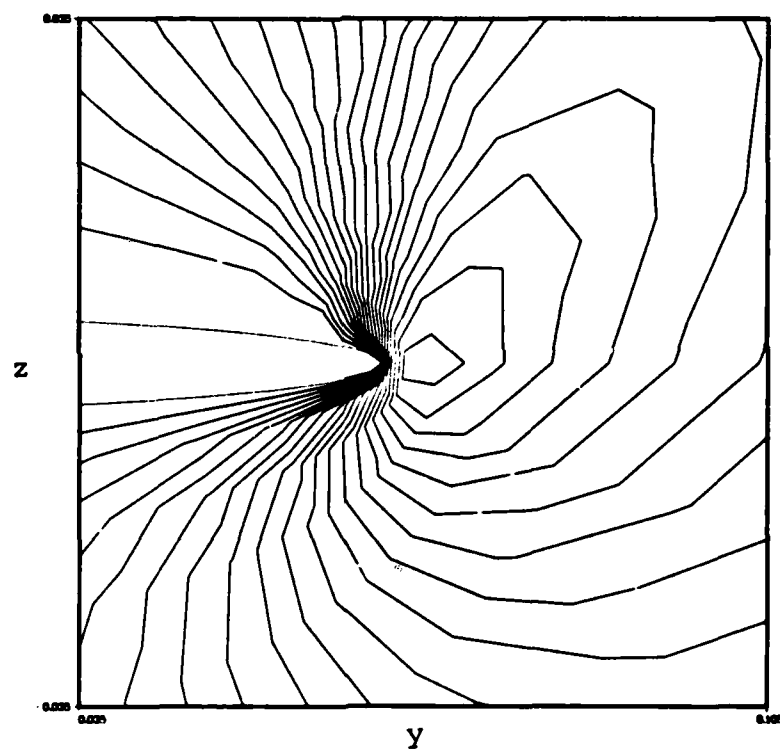
$Re = 5.0 \cdot 10^5$

(c) Crossflow plane velocity vectors
Figure 47. (Continued).



(d) Plot of C_p
Figure 47. (Continued).

75/63 DOUBLE DELTA J=12 Z=.2496 B=.0669



$M_\infty = 0.50$

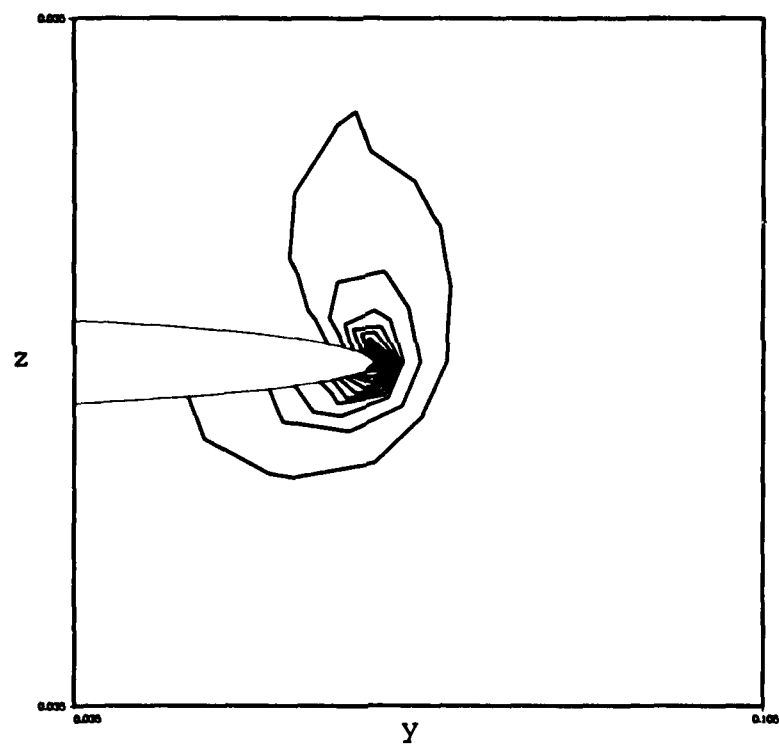
$\alpha = 90.00$

$Re = 5.0 \cdot 10^5$

(e) Crossflow Mach number contours.

Figure 47. (Continued).

75/63 DOUBLE DELTA J=12 Z=.2496 B=.0669



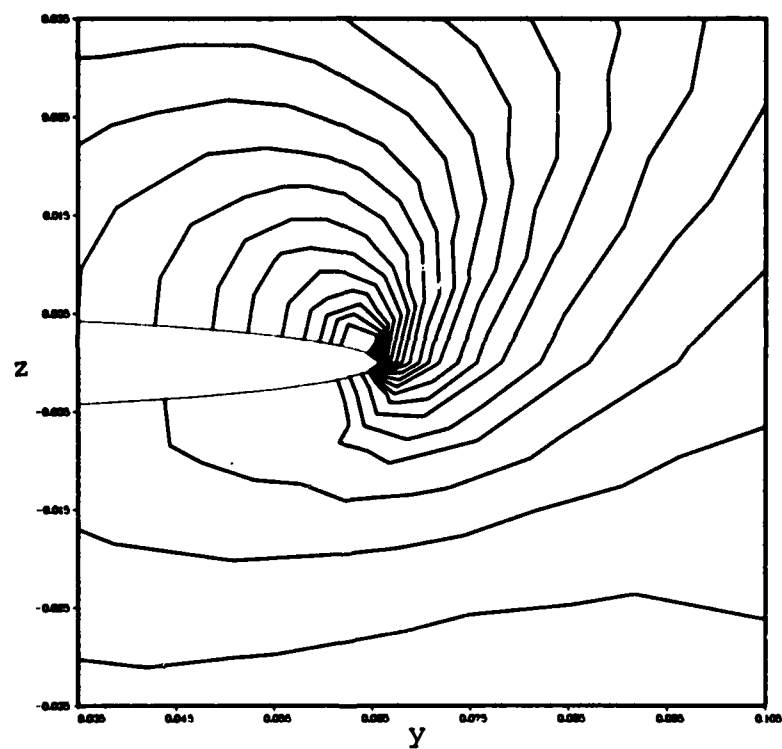
$M_\infty = 0.50$

$\alpha = 90.00$

$Re = 5.0 \cdot 10^4$

(f) Vorticity contours
Figure 47. (Continued).

75/63 DOUBLE DELTA J=12 Z=.2496 B=.0669



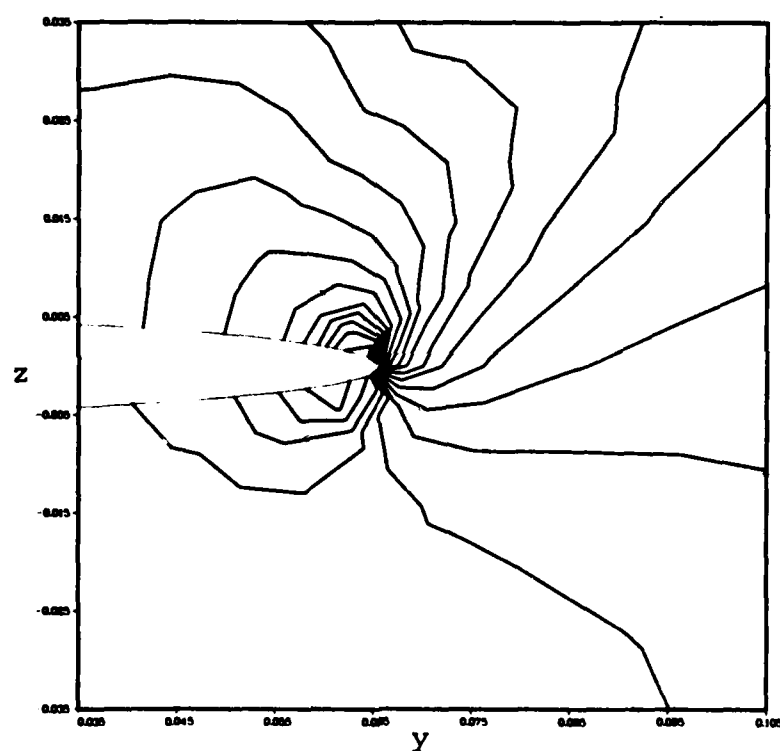
$M_\infty = 0.50$

$\alpha = 90.00$

$Re = 5.0 \cdot 10^5$

(g) Density contours
Figure 47. (Continued).

75/63 DOUBLE DELTA J=12 Z=.2496 B=.0669



$M_\infty = 0.50$

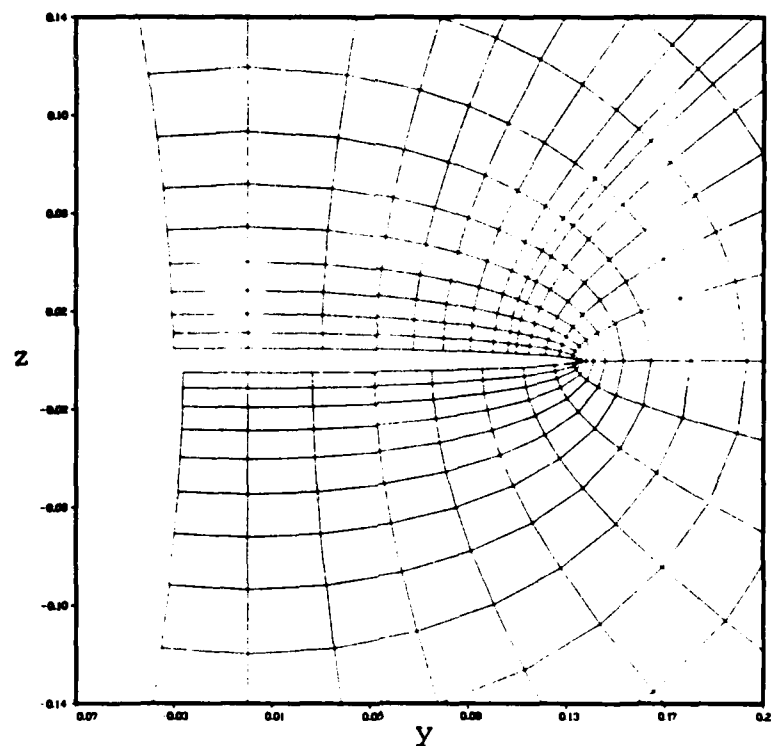
$\alpha = 90.00$

$Re = 5.0 \cdot 10^5$

(h) Pressure contours

Figure 47. (Concluded).

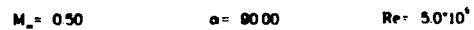
75 63 DOUBLE DELTA J=16 Z=.5025



(a) Grid plot

Figure 48. Crossflow plane characteristics at $x = .503$.

0107 0	16.56.09	1 JUL 5 1961	0351-00	WASH DC	0.2
--------	----------	--------------	---------	---------	-----

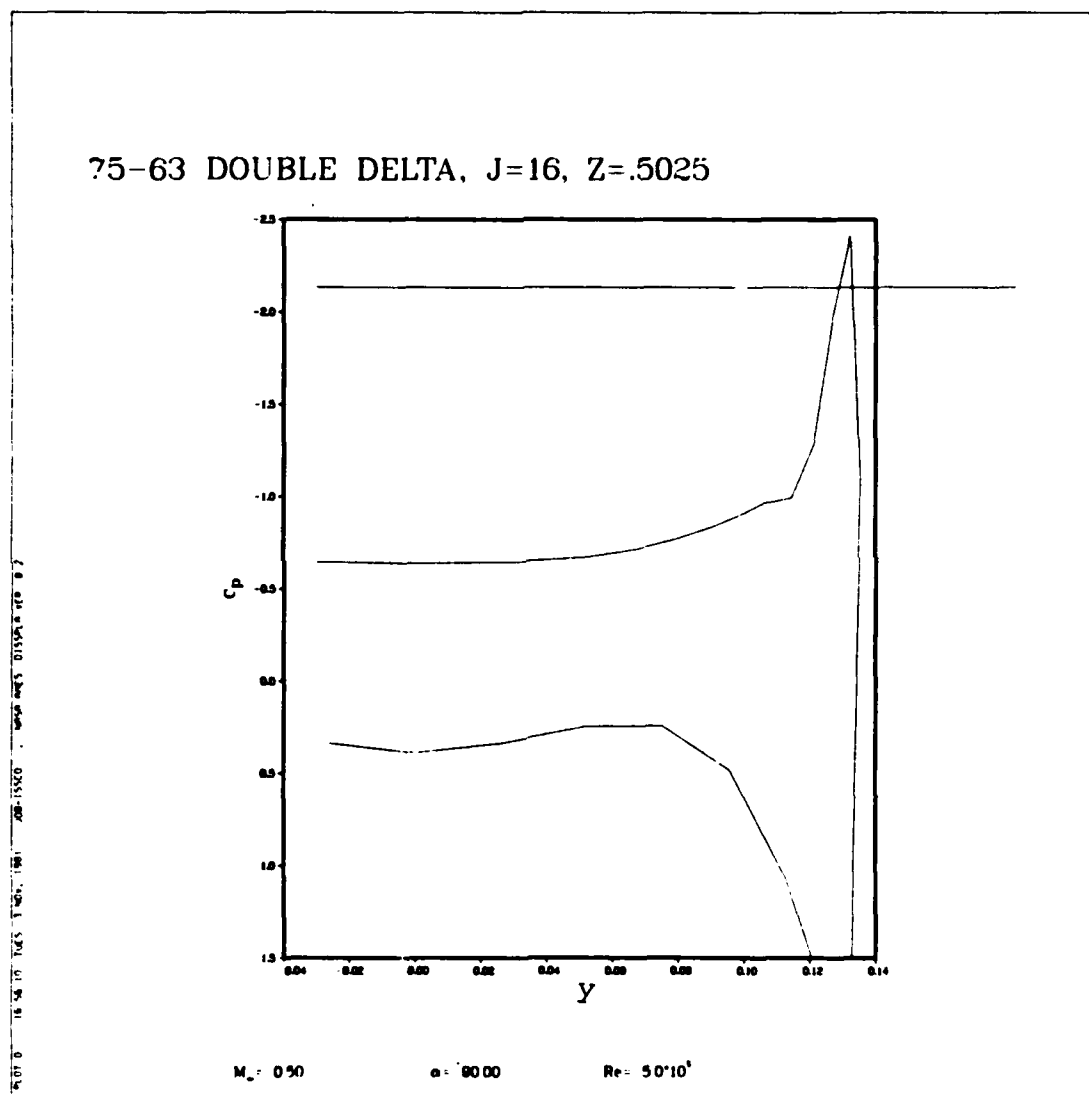


103

01.02.0 16.04.91 7.15.91 1991 00-1500 0354 01554 0.2

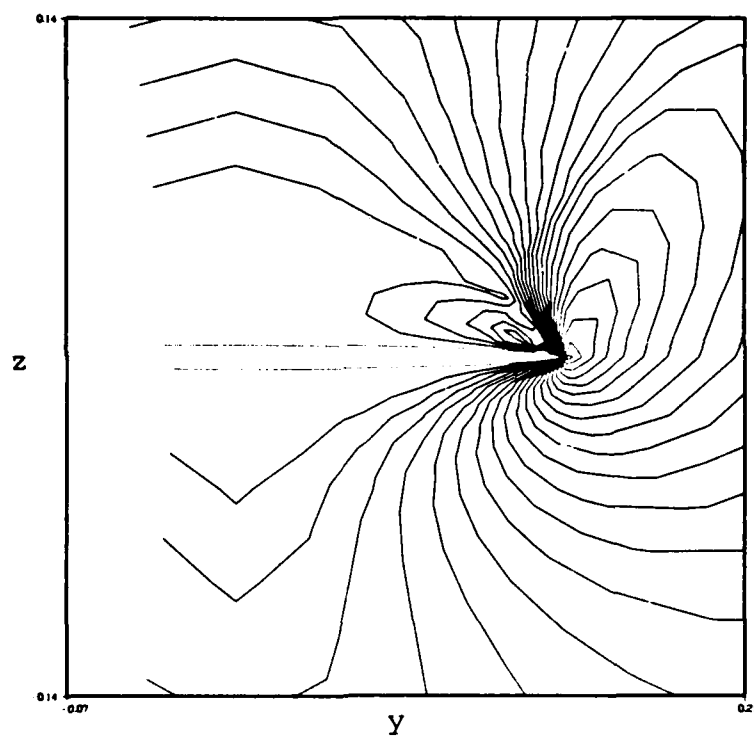


Figure 48. (Continued).



(d) Plot of C_p
Figure 48. (Continued).

75-63 DOUBLE DELTA, $J=16$, $Z=.5025$



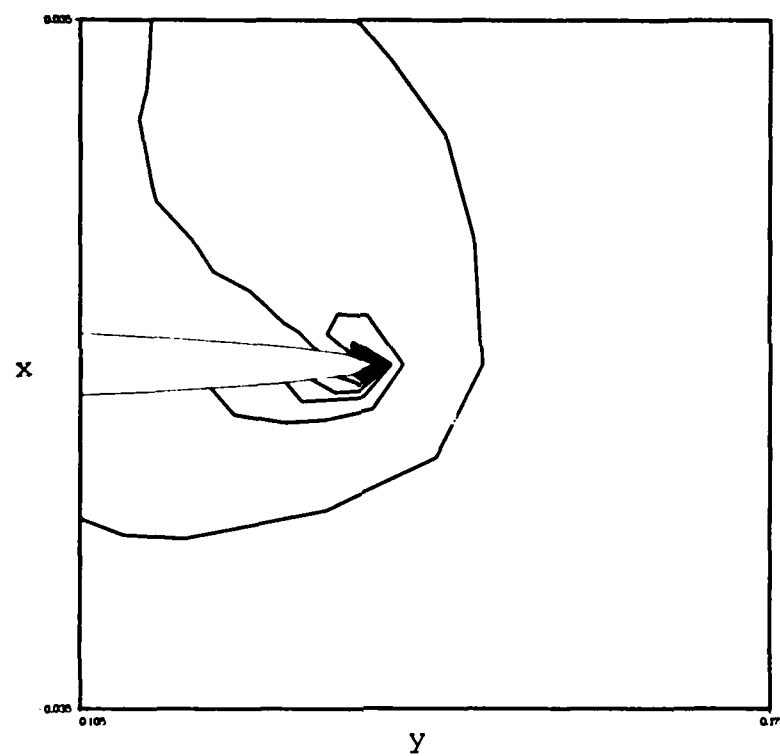
$M_\infty = 0.50$

$\alpha = 90.00$

$Re = 5.0 \times 10^5$

(e) Crossflow Mach number contours
Figure 48. (Continued).

75/63 DOUBLE DELTA J=16 Z=.5025



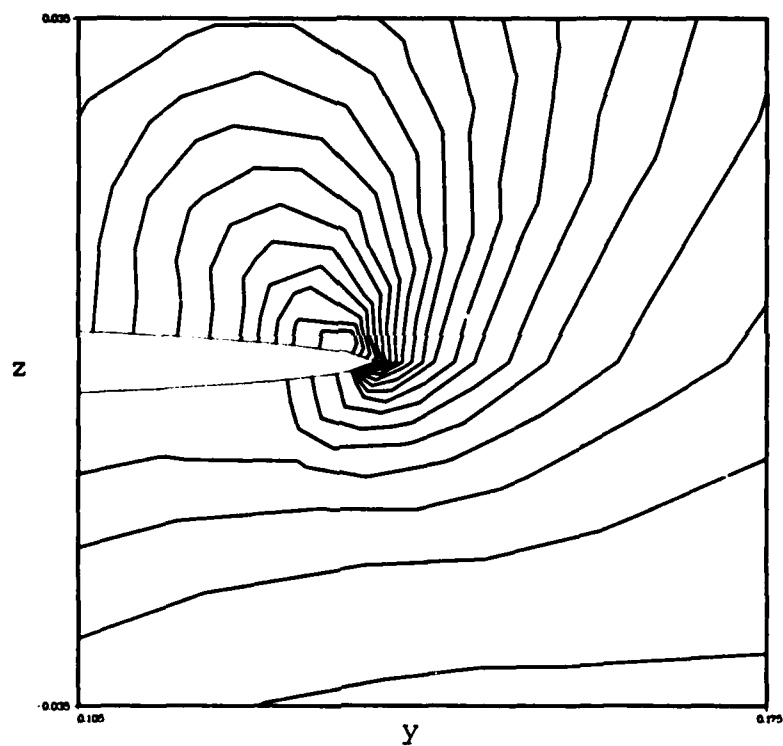
$M_\infty = 0.50$

$\alpha = 90.00$

$Re = 5.0 \cdot 10^5$

(f) Vorticity contours
Figure 48. (Continued).

75-63 DOUBLE DELTA, $J=16$, $Z=.5025$



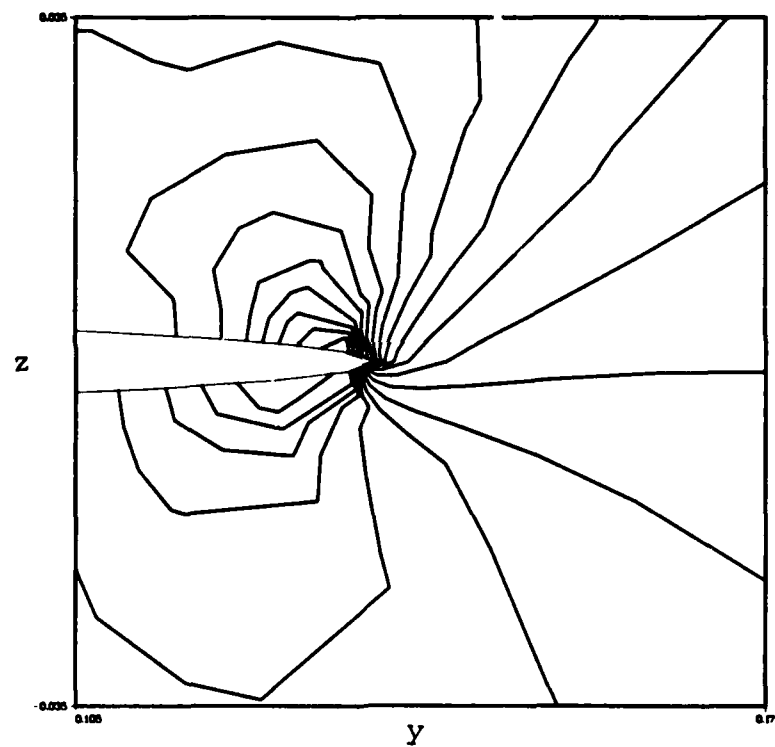
$M_\infty = 0.50$

$\alpha = 90.00$

$Re = 5.0 \cdot 10^5$

(g) Density contours
Figure 48. (Continued)

75-63 DOUBLE DELTA, $J=16$, $Z=.5025$



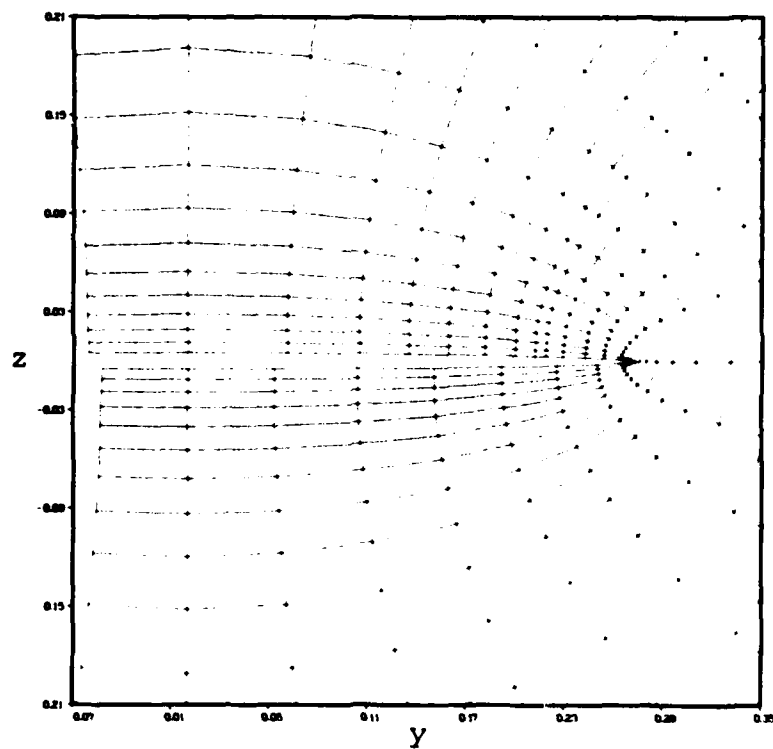
$M_\infty = 0.50$

$\alpha = 90.00$

$Re = 5.0 \cdot 10^5$

(h) Pressure contours
Figure 48. (Concluded).

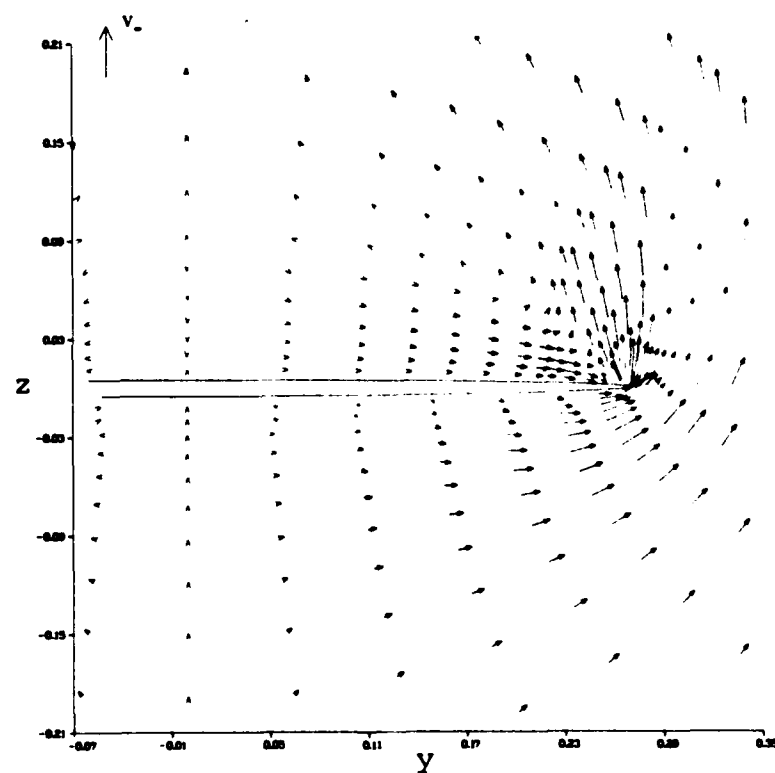
75 63 DOUBLE DELTA J=20 Z=.7632 B=.2681



(a) Grid plot

Figure 49. Crossflow plane characteristics at $x = .76$.

75/63 DOUBLE DELTA J=20 Z=.7632 B=.2681



$M_\infty = 0.50$

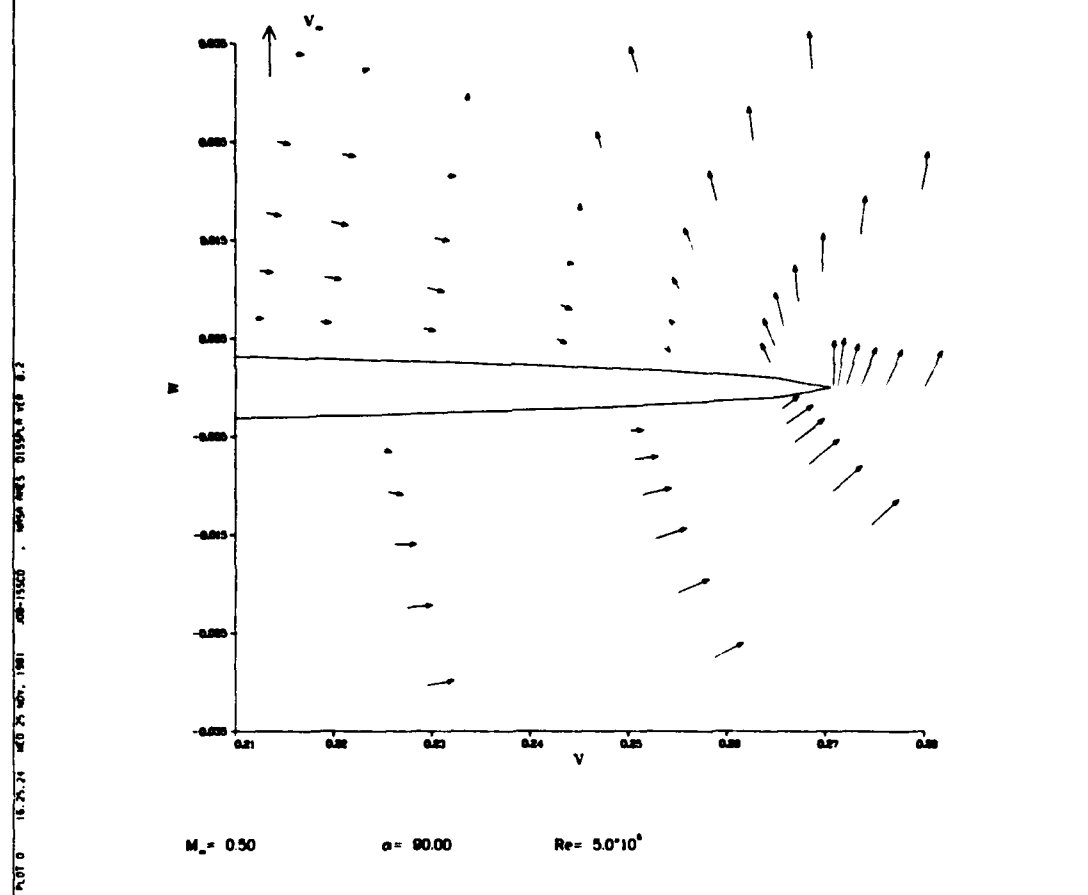
$\alpha = 90.00$

$Re = 5.0 \cdot 10^5$

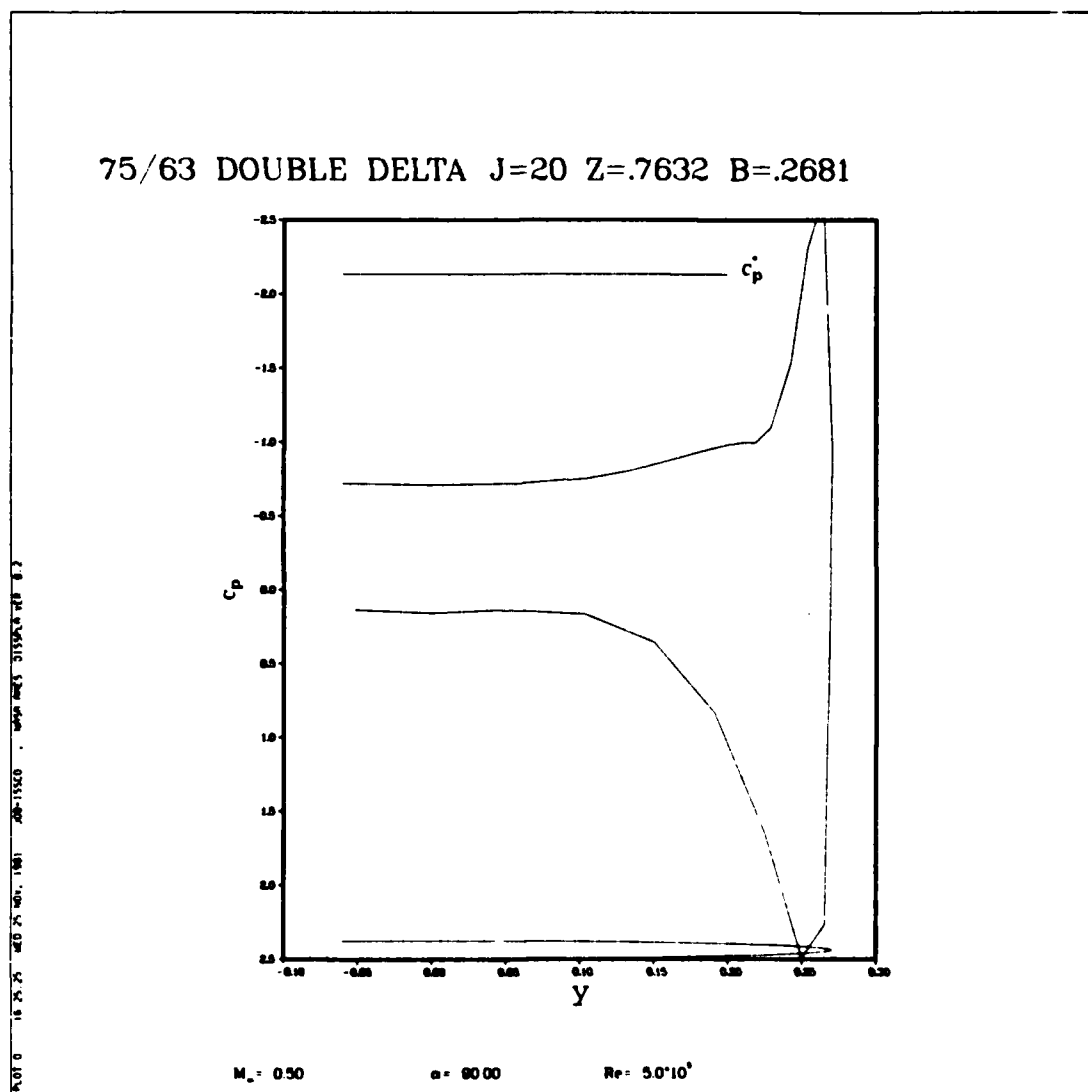
(b) Crossflow plane velocity vectors

Figure 49. Continued

75/63 DOUBLE DELTA J=20 Z=.7632 B=.2681

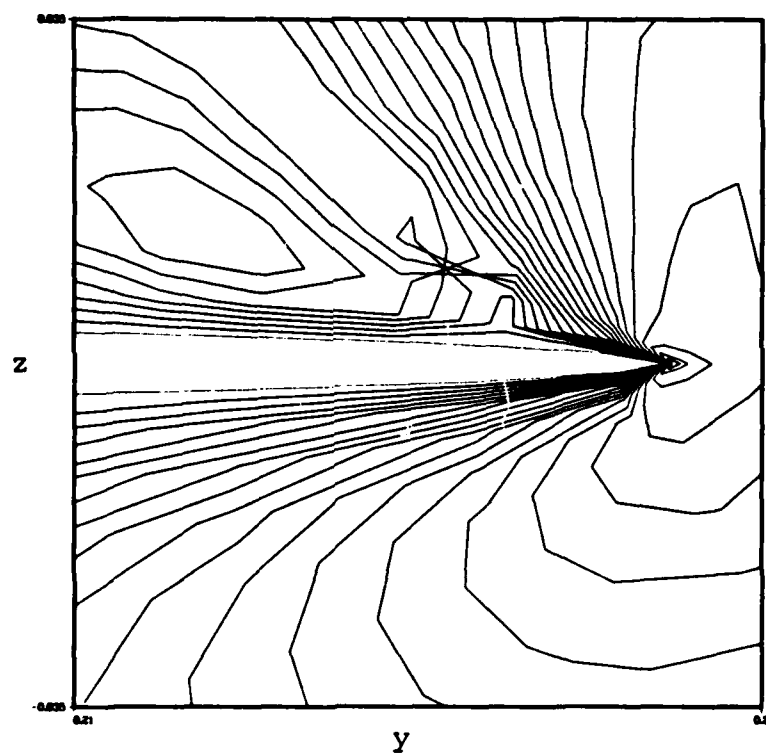


(c) Crossflow plane velocity vectors
Figure 49. (Continued).



(d) Plot of C_p
Figure 49. (Continued).

75/63 DOUBLE DELTA J=20 Z=.7632 B=.2681



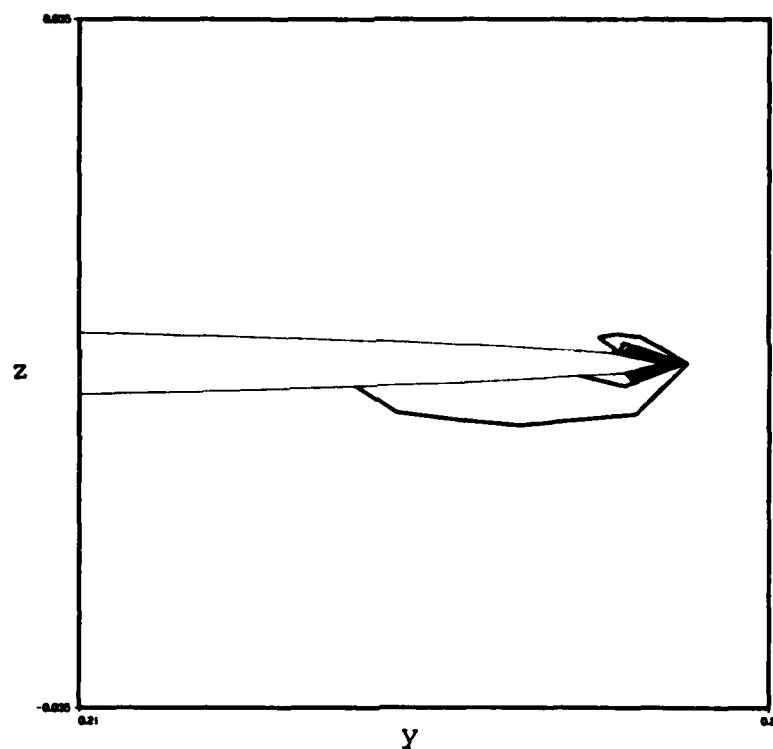
$M_\infty = 0.50$

$\alpha = 90.00$

$Re = 5.0 \cdot 10^5$

(e) Crossflow Mach number contours
Figure 49. (Continued).

75/63 DOUBLE DELTA J=20 Z=.7632 B=.2681



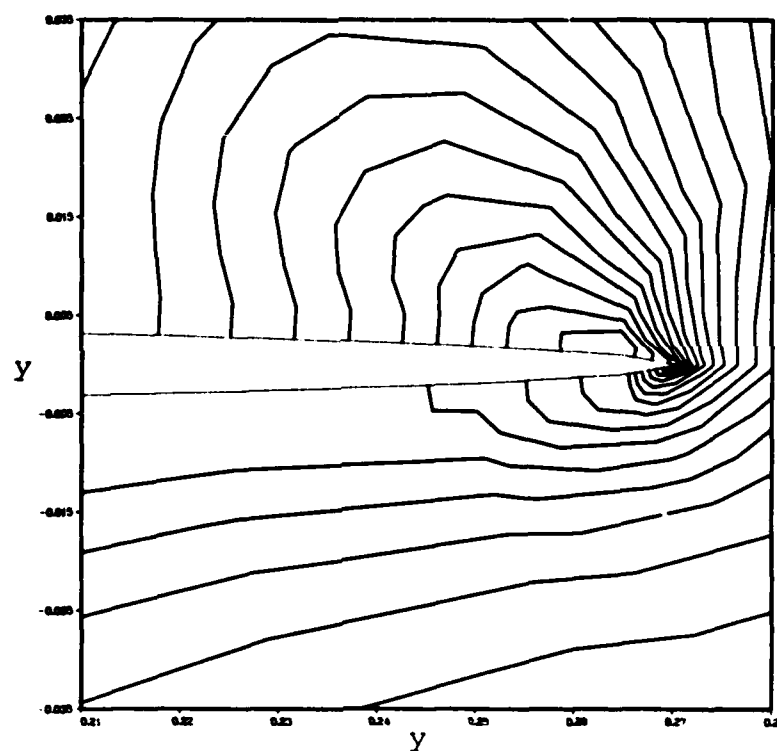
$M_\infty = 0.50$

$\alpha = 90.00$

$Re = 5.0 \cdot 10^5$

(f) Vorticity contours
Figure 49. (Continued)

75/63 DOUBLE DELTA J=20 Z=.7632 B=.2681



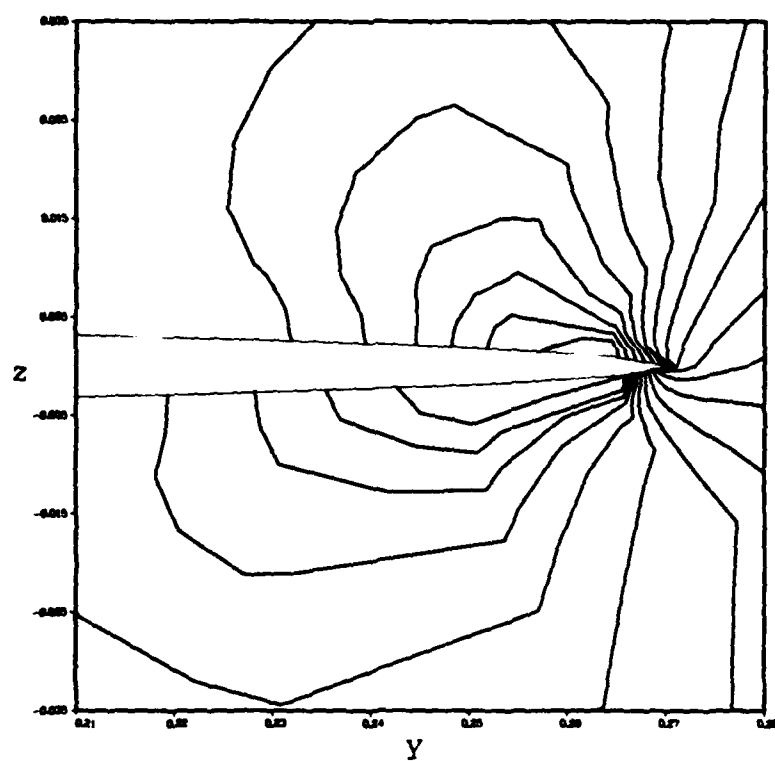
$M_\infty = 0.50$

$\alpha = 90.00^\circ$

$Re = 5.0 \times 10^5$

(g) Density contours
Figure 49. (Continued)

75/63 DOUBLE DELTA J=20 Z=.7632 B=.2681



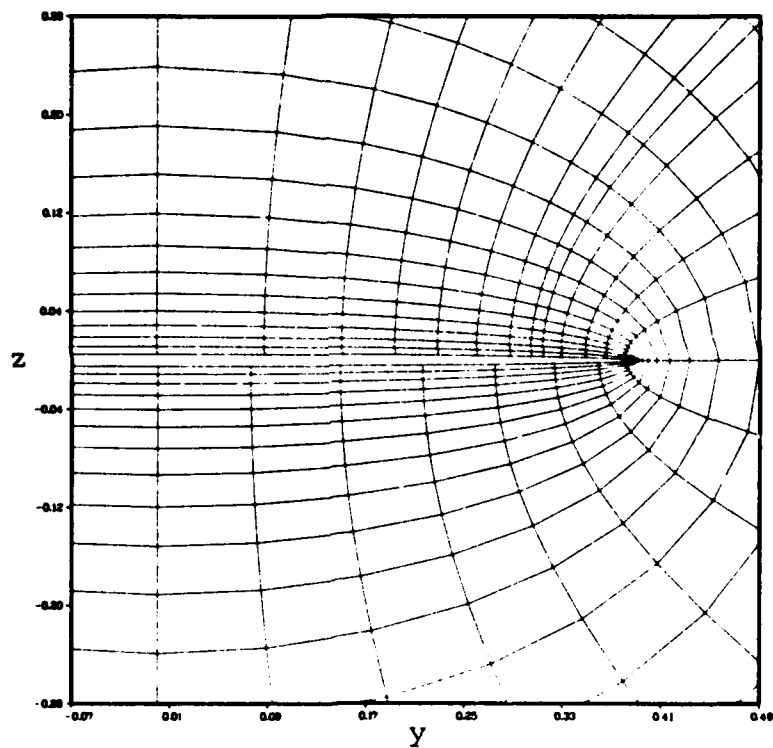
$M_\infty = 0.50$

$\alpha = 90.00$

$Re = 5.0 \times 10^5$

(h) Pressure contours
Figure 49. (Concluded).

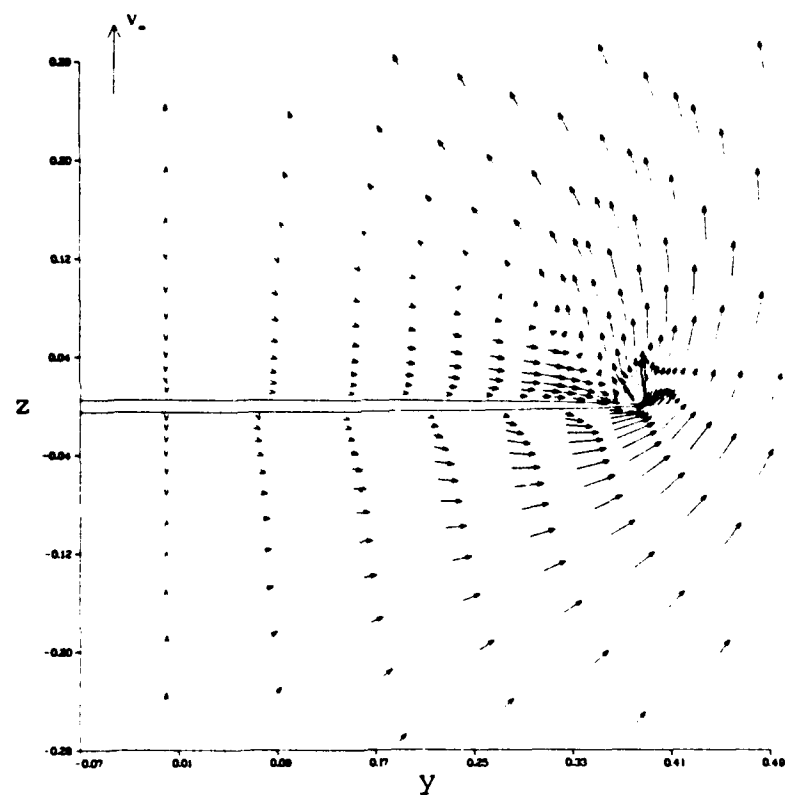
75/63 DOUBLE DELTA J=24 Z=1. B=.3887 TAIL PLANE



(a) Grid plot

Figure 50. Crossflow plane characteristic for $x = 1.0$.

75/63 DOUBLE DELTA J=24 Z=1. B=.3887 TAIL PLANE



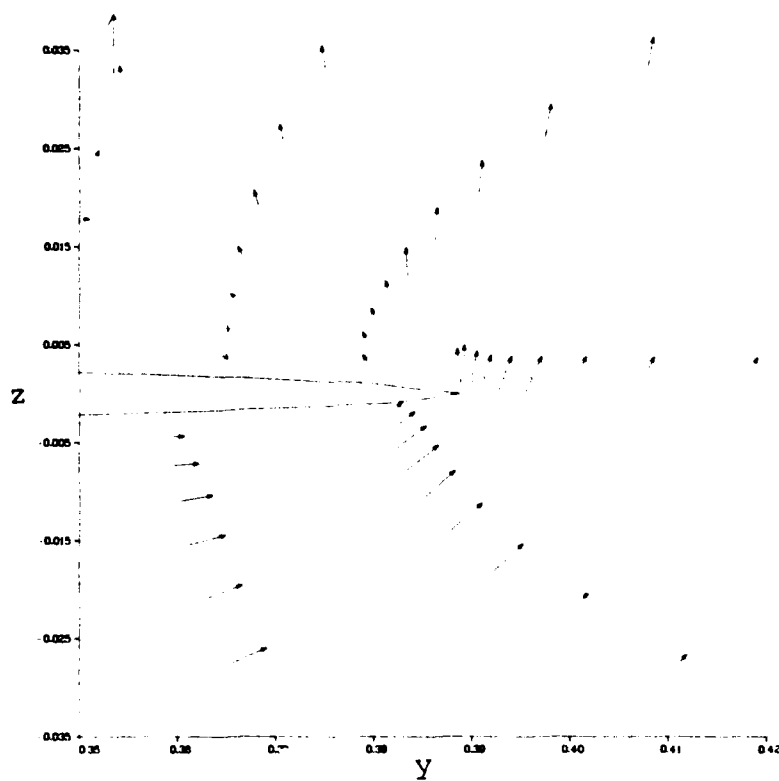
$M_\infty = 0.50$

$\alpha = 90.00$

$Re = 5.0 \cdot 10^5$

(b) Crossflow plane velocity vectors.
Figure 50. (Continued).

75 '63 DOUBLE DELTA J=24 Z=1. B=.3887 TAIL PLANE



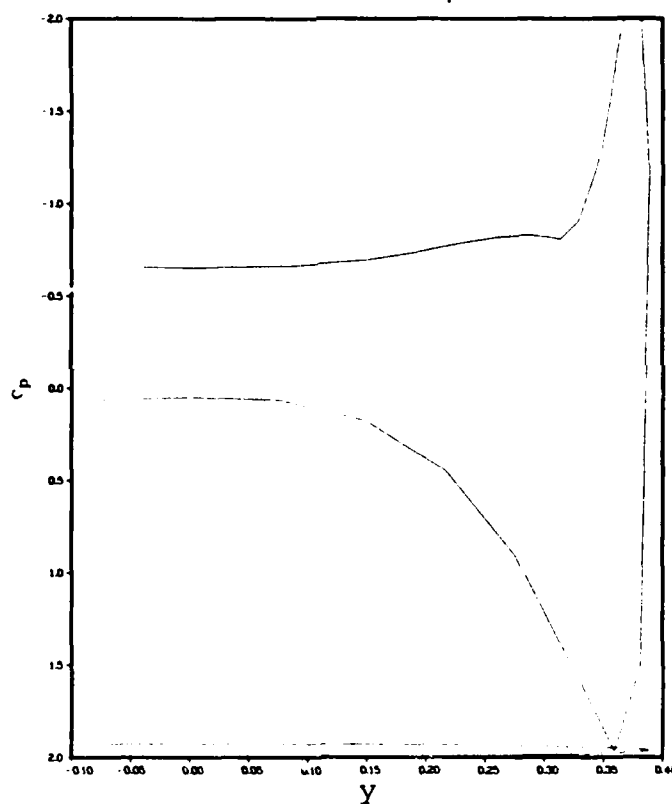
$M_\infty = 0.50$

$\alpha = 90.00$

$Re = 5.0 \cdot 10^5$

(c) Crossflow plane velocity vectors
Figure 50. (Continued).

75.63 DOUBLE DELTA J=24 Z=1. B=.3887 TAIL PLANE



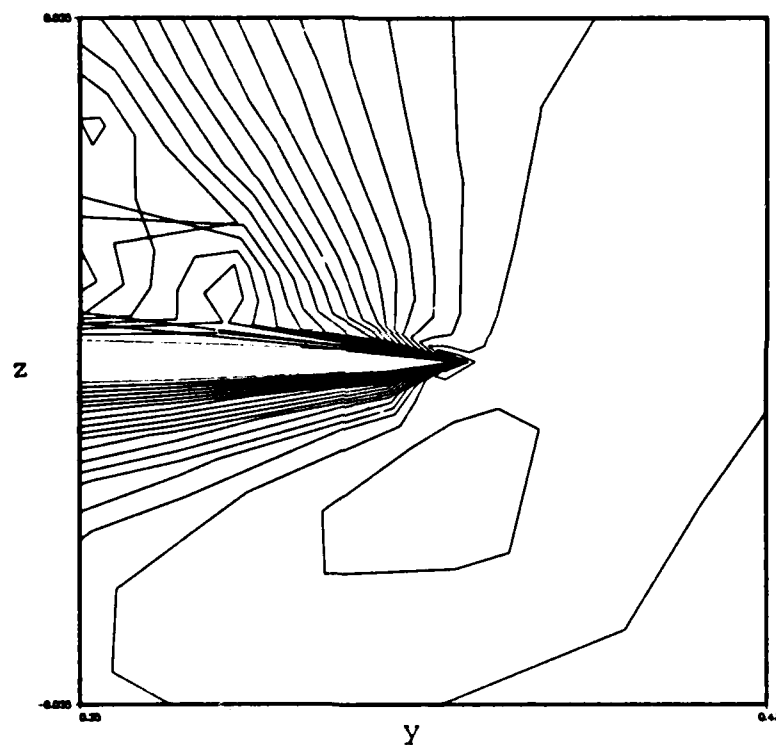
$M_\infty = 0.50$

$\alpha = 90.00$

$Re = 5.0 \cdot 10^7$

(d) Plot of C_p
Figure 50. (Continued).

75/63 DOUBLE DELTA J=24 Z=1. B=.3887 TAIL PLANE



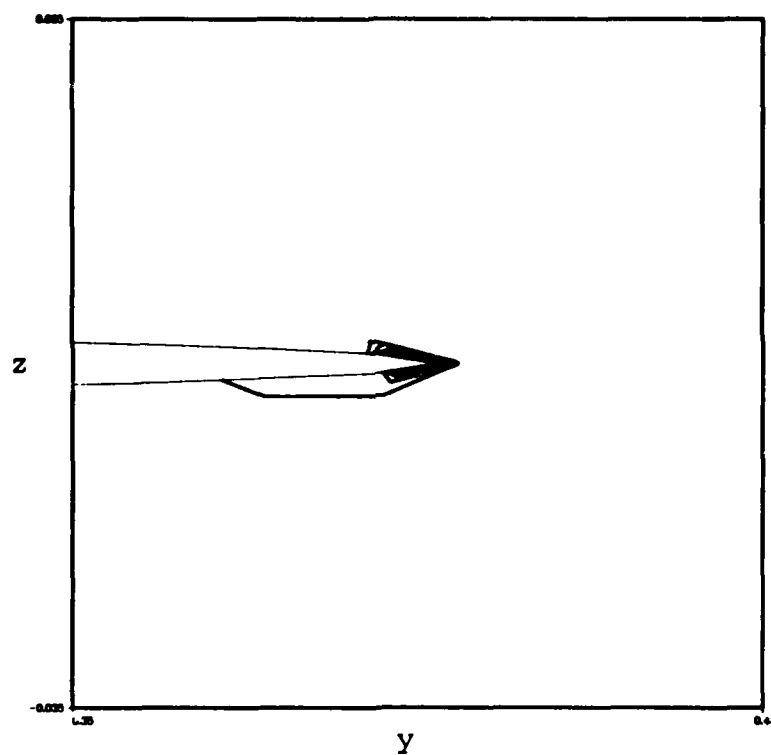
$M_\infty = 0.50$

$\alpha = 90.00$

$Re = 5.0 \cdot 10^5$

(e) Crossflow Mach number contours
Figure 50. (Continued).

75/63 DOUBLE DELTA J=24 Z=1. B=.3887 TAIL PLANE



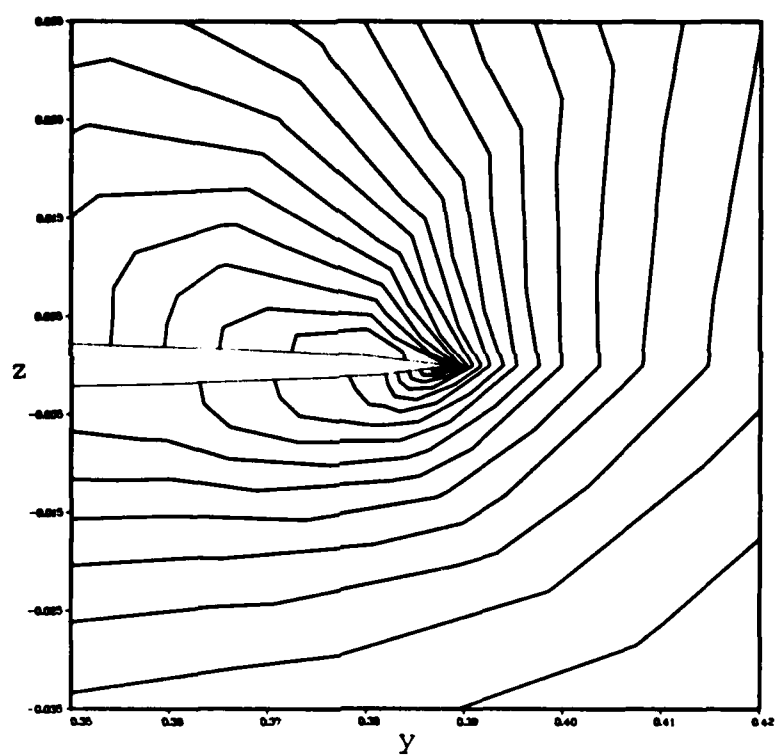
$M_\infty = 0.50$

$\alpha = 90.00$

$Re = 5.0 \cdot 10^5$

(f) Vorticity contours
Figure 50. (Continued).

75/63 DOUBLE DELTA J=24 Z=1. B=.3887 TAIL PLANE



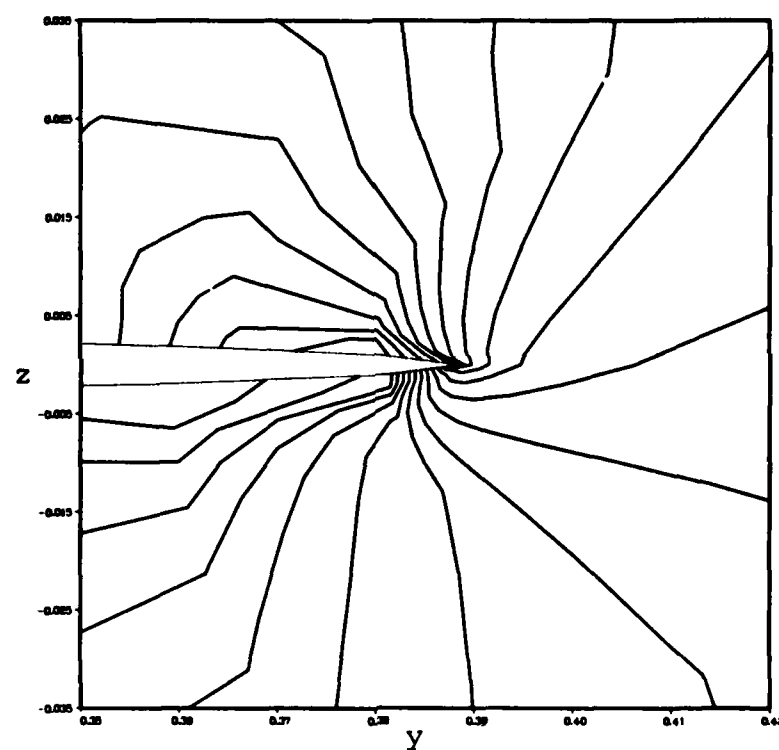
$M_\infty = 0.50$

$\alpha = 90.00$

$Re = 5.0 \cdot 10^5$

(g) Density contours
Figure 50. Continued.

75/63 DOUBLE DELTA J=24 Z=1. B=.3887 TAIL PLANE



$M_\infty = 0.50$

$\alpha = 90.00$

$Re = 5.0 \cdot 10^5$

(h) Pressure contours
Figure 50. (Continued).

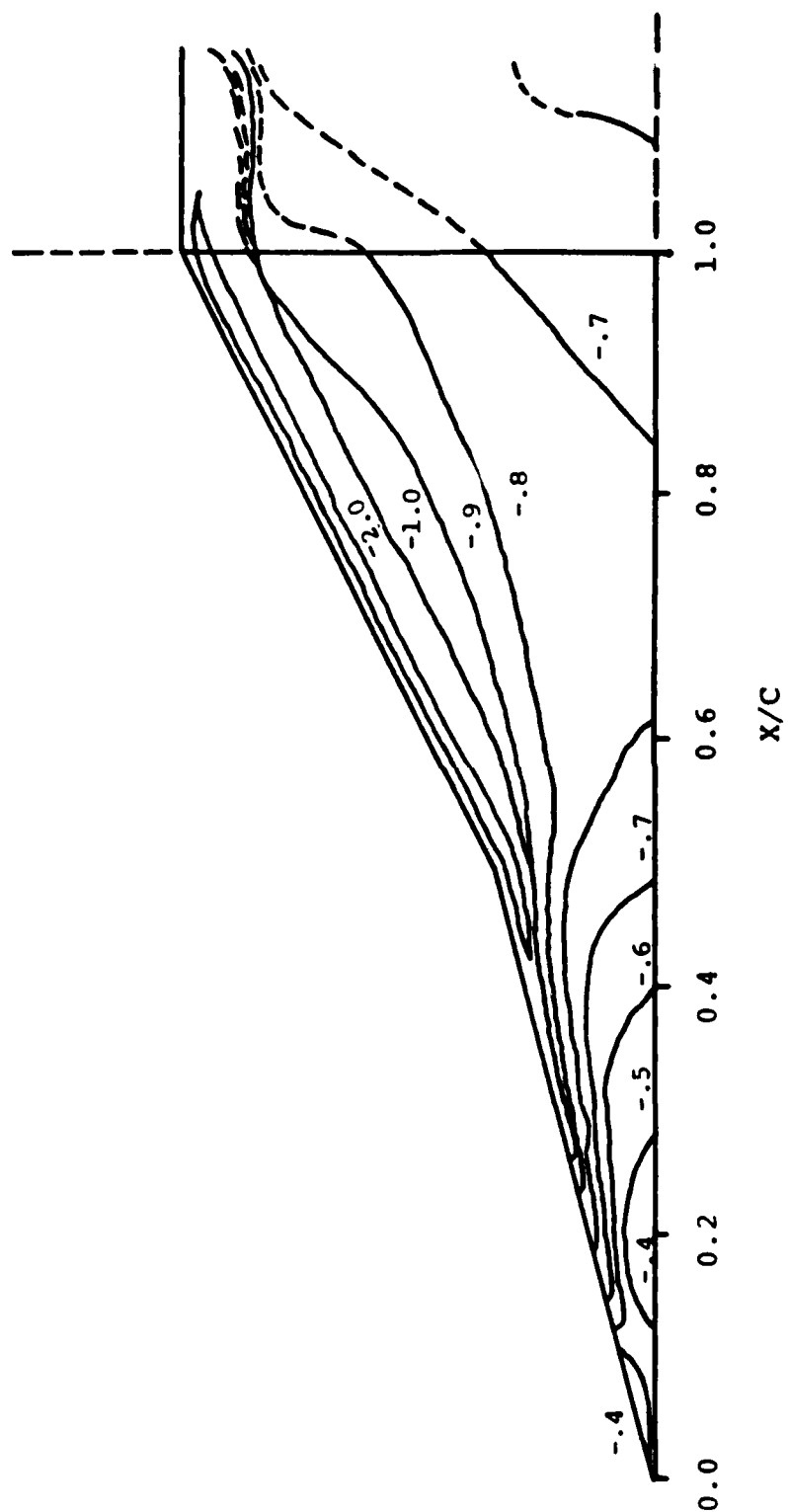


Figure 51. Calculated upper surface pressure coefficient contours, $\alpha = 15^\circ$, $M_\infty = 0.5$.

Upper surface pressure
 $\alpha = 15^\circ$
 Data from Ref. 10.

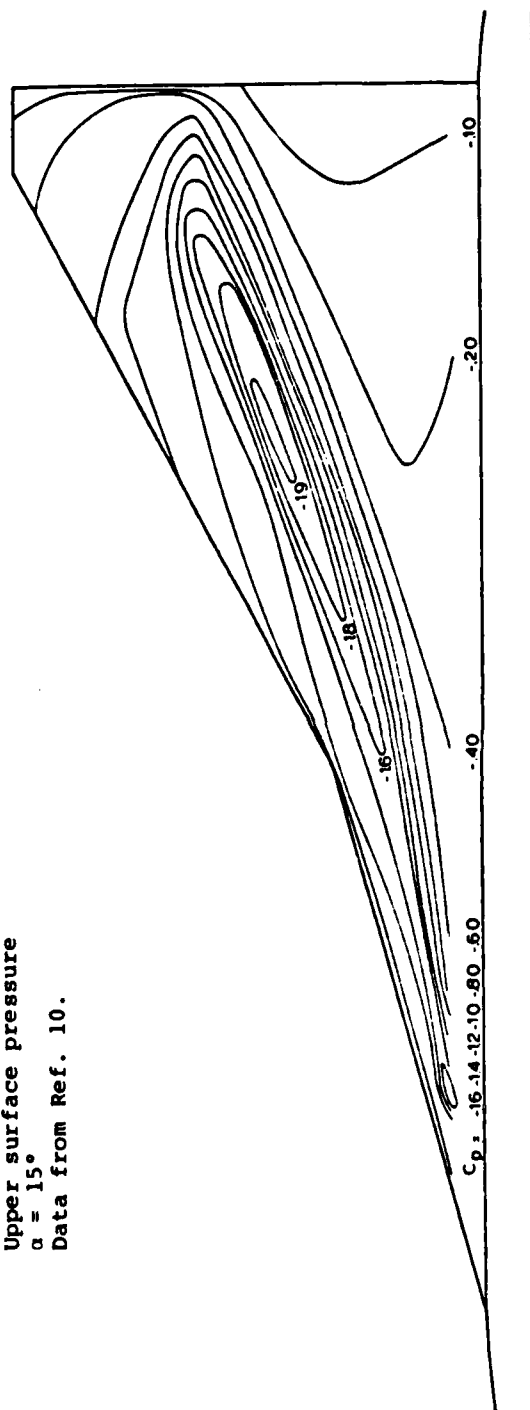


Figure 52. Measured upper surface pressure coefficient contours,
 $\alpha = 15^\circ$, $M_\infty = 0.16$.

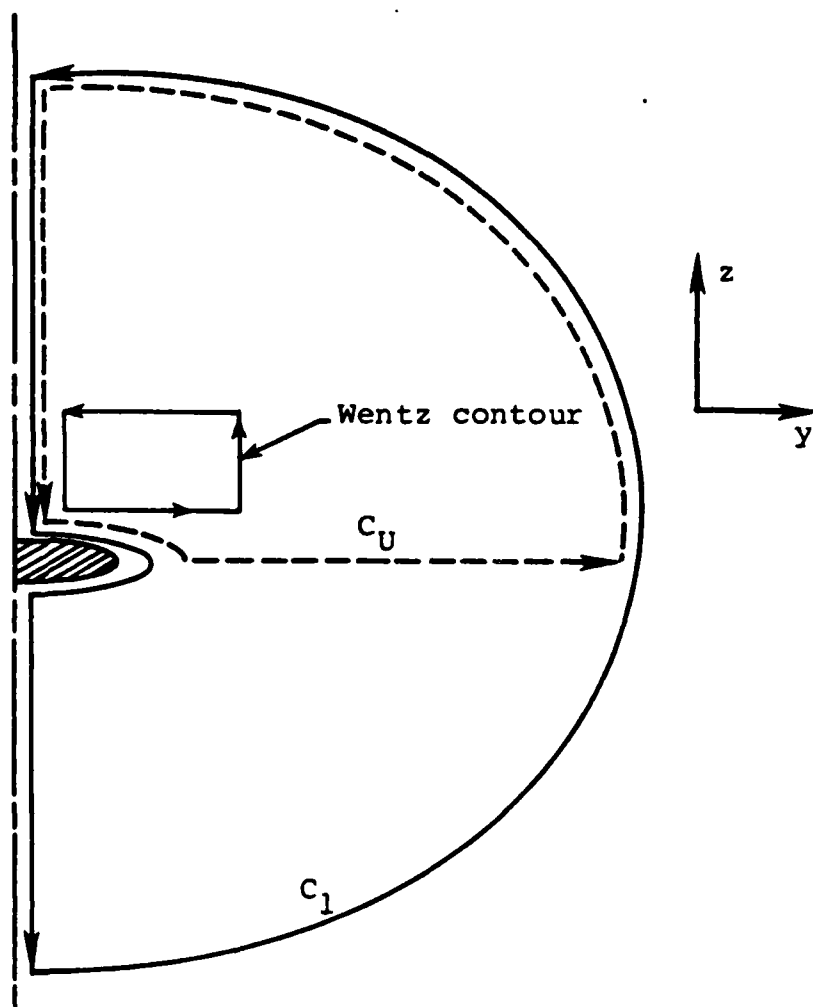


Figure 53. Integration contours for circulation calculation in a crossflow plane.

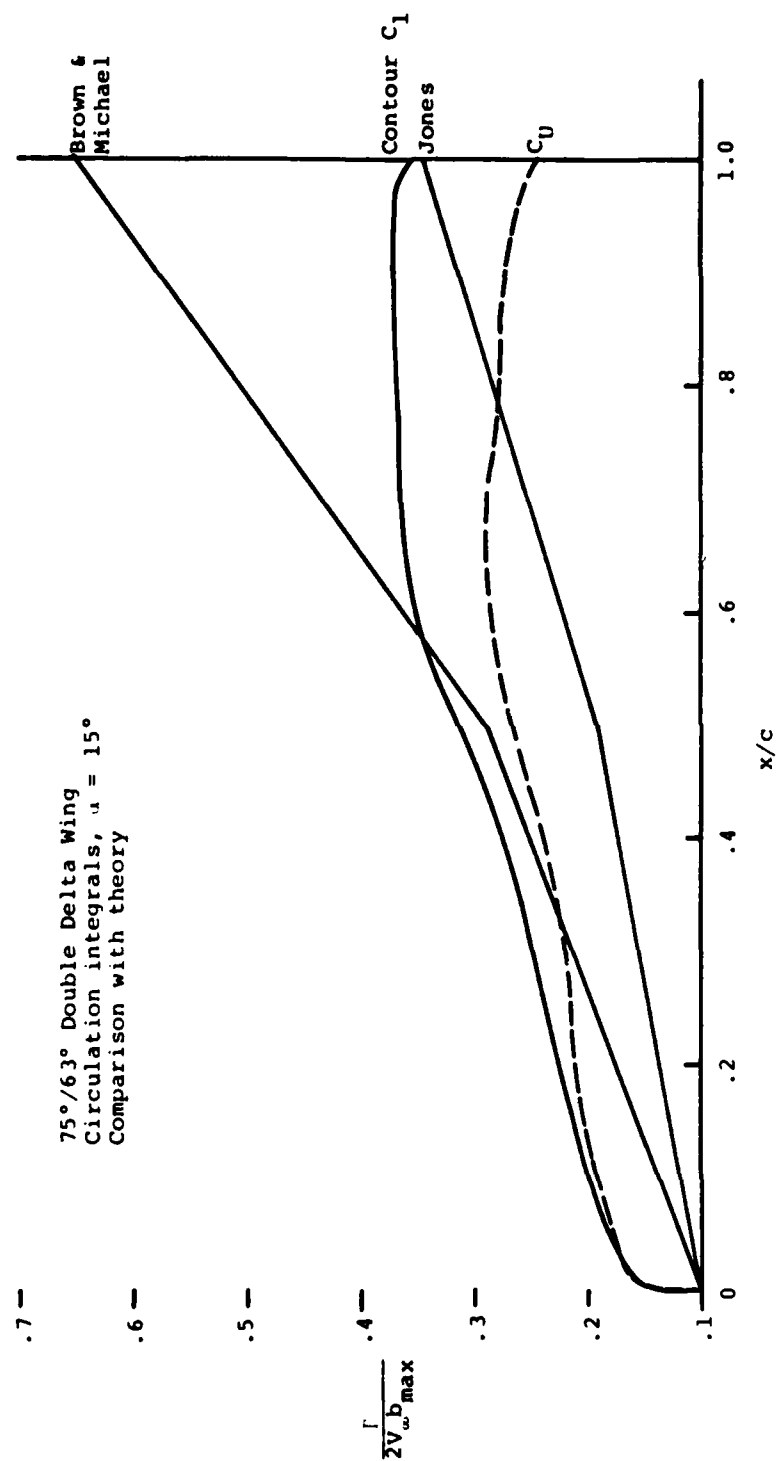


Figure 54. Comparison of circulation integral results with other theories.

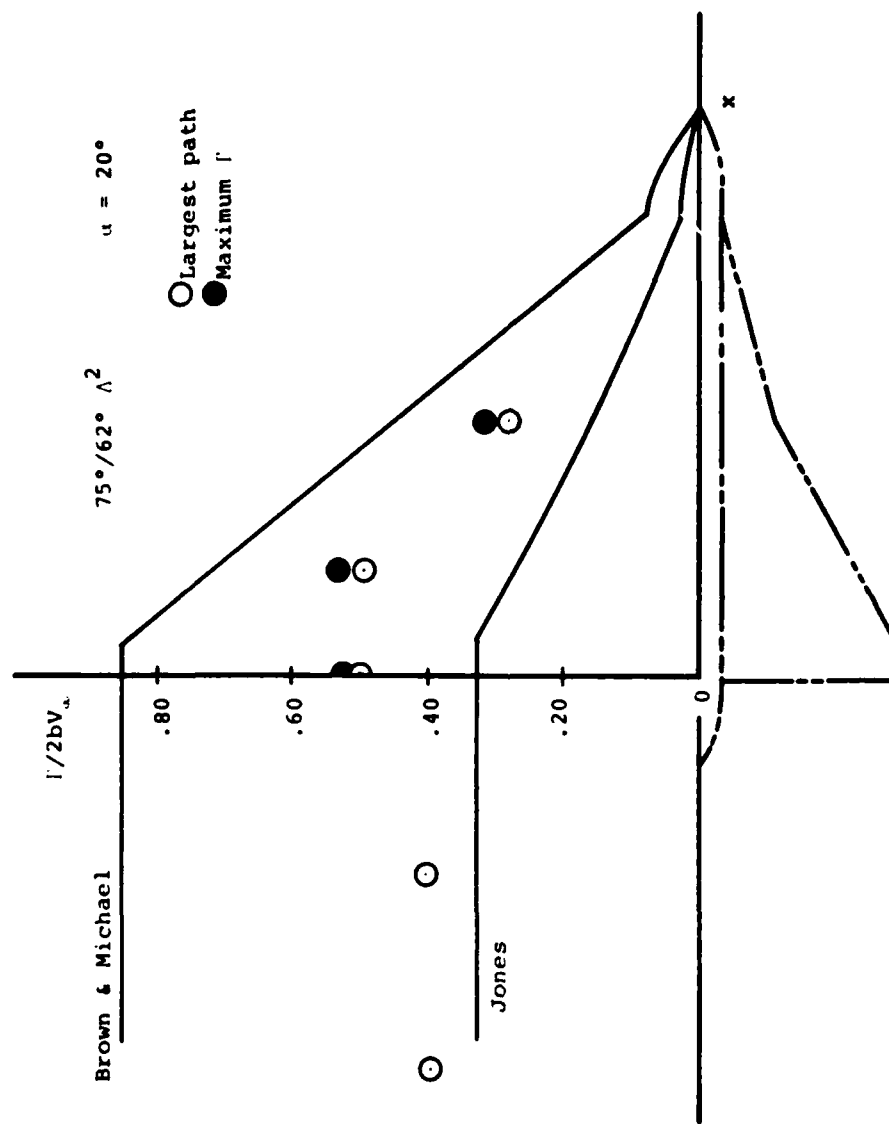


Figure 55. Comparison of measured and predicted circulation results from Wentz. (Ref. 10).

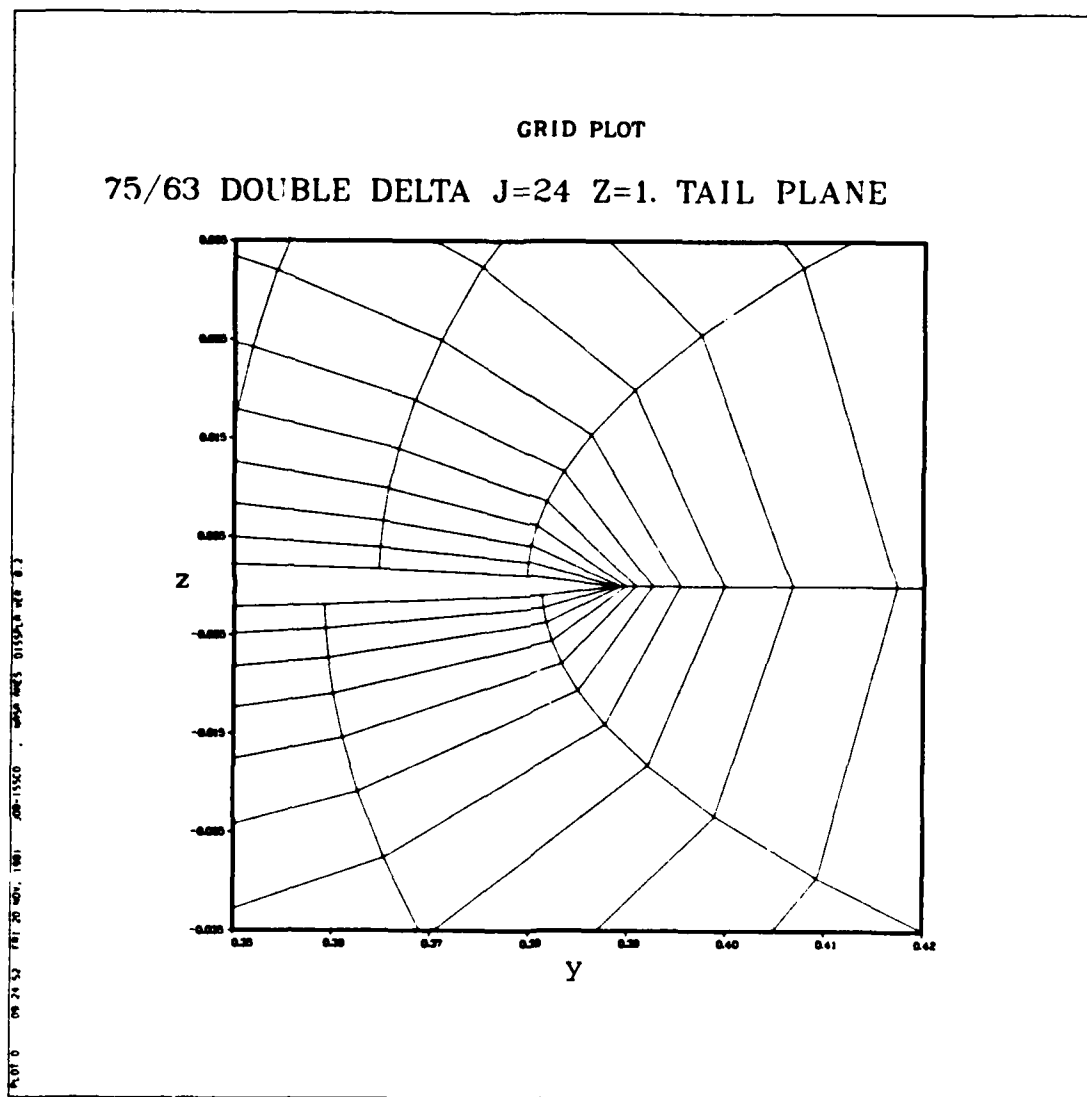


Figure 56. Close up of orthogonal mesh near edge.

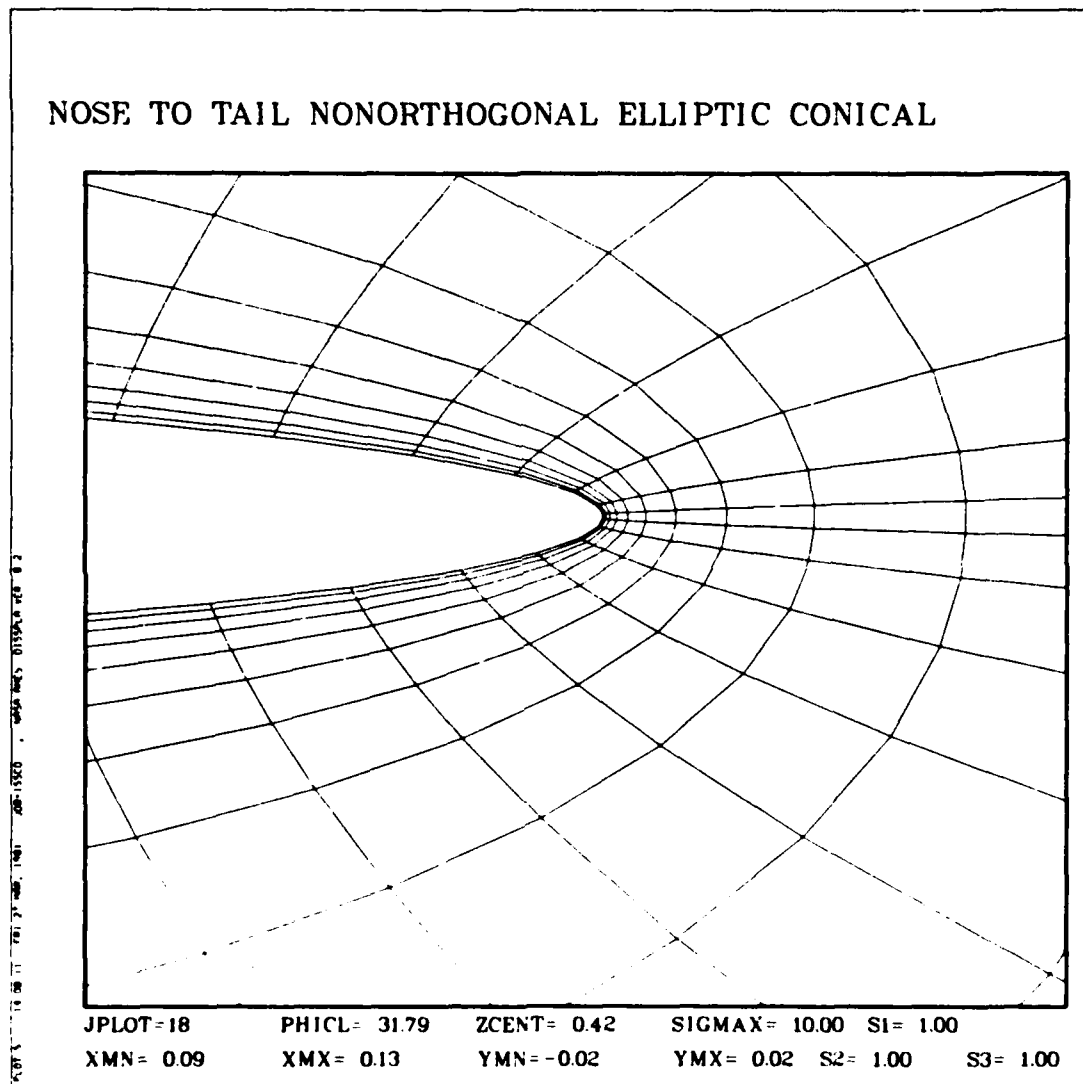


Figure 57. Close up of nonorthogonal mesh near edge.

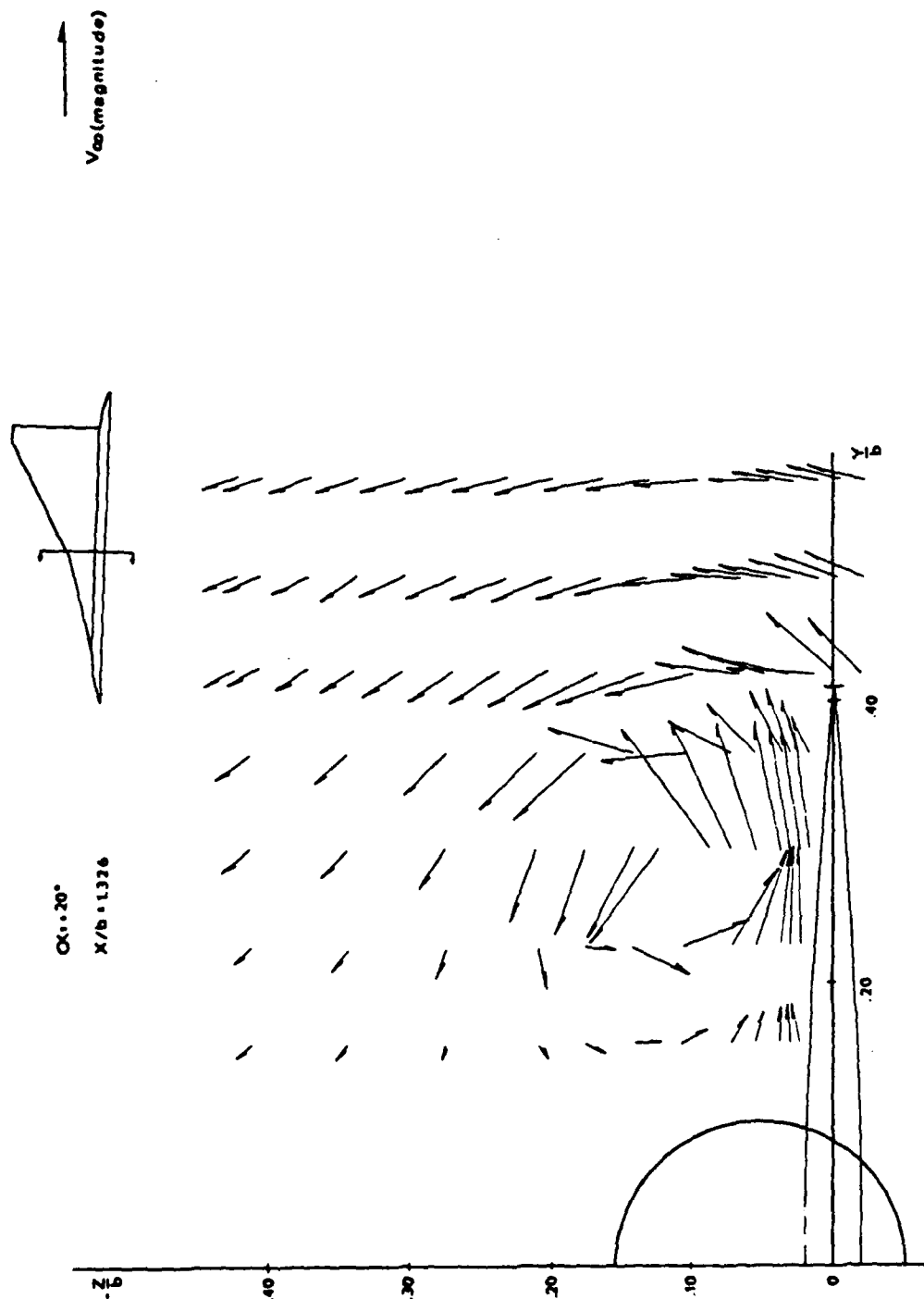


Figure 58. Flow field measurements from Wentz. (Ref. 10).

DISTRIBUTION LIST

Technical Library
Building 313
Ballistic Research Laboratories
Aberdeen Proving Ground, MD 21005

Defense Technical Information Center
Cameron Station, Building 5
Alexandria, VA 22314

Library
Naval Academy
Annapolis, MD 21402

Director, Tactical Technology Office
Defense Advanced Research Projects
Agency
1400 Wilson Boulevard
Arlington, VA 22209

Code 200B
Office of Naval Research
800 N. Quincy Street
Arlington, VA 22217

Code 438
Office of Naval Research
800 N. Quincy Street
Arlington, VA 22217

Dr. J. L. Potter
Deputy Director, Technology
von Karman Gas Dynamics Facility
Arnold Air Force Station, TN 37389

Professor J. C. Wu
School of Aerospace Engineering
Georgia Institute of Technology
Atlanta, GA 30332

NASA Scientific and Technical
Information Facility
P.O. Box 8757
Baltimore/Washington International
Airport, MD 21240

Dr. T. C. Tai
Code 1606
David W. Taylor Naval Ship
Research and Development Center
Bethesda, MD 20084

Dr. G. R. Inger
Department of Aerospace Engineering
Virginia Polytechnic Institute and
State University
Blacksburg, VA 24061

Professor A. H. Nayfeh
Department of Engineering Science
Virginia Polytechnic Institute and
State University
Blacksburg, VA 24061

Dr. A. Rubel
Research Department
Grumman Aerospace Corporation
Bethpage, NY 11714

Commanding Officer
Office of Naval Research Eastern/Central
Regional Office
666 Summer Street, Bldg. 114,
Section D
Boston, MA 02210

Commanding Officer
Office of Naval Research Branch Office
536 South Clark Street
Chicago, IL 60605

Code 753
Naval Weapons Center
China Lake, CA 93555

Mr. J. Marshall
Code 4063
Naval Weapons Center
China Lake, CA 93555

Professor R. T. Davis
Department of Aerospace Engineering
University of Cincinnati
Cincinnati, OH 45221

Library MS 60-3
NASA Lewis Research Center
21000 Brookpark Road
Cleveland, OH 44135

Dr. J. D. Anderson, Jr.
Chairman, Department of Aerospace
Engineering
College of Engineering
University of Maryland
College Park, MD 20742

Professor O. Burggraf
Department of Aeronautical and
Astronautical Engineering
Ohio State University
1314 Kinnear Road
Columbus, OH 43212

Technical Library
Naval Surface Weapons Center
Dahlgren Laboratory
Dahlgren, VA 22448

Technical Library 2-51131
LTV Aerospace Corporation
P. O. Box 5907
Dallas, TX 75222

Library, United Aircraft Corporation
Research Laboratories
Silver Lane
East Hartford, CT 06108

Dr. W. R. Briley
Scientific Research Associates, Inc.
P. O. Box 498
Glastonbury, CT 06033

Library (MS 185)
NASA Langley Research Center
Langley Station
Hampton, VA 23665

Technical Library
Naval Ordnance Station
Indian Head, MD 20640

Professor E. L. Resler
Sibley School of Mechanical and
Aerospace Engineering
Cornell University
Ithaca, NY 14850

Library
Midwest Research Institute
425 Volker Boulevard
Kansas City, MO 64110

Dr. J. J. Riley
Flow Research, Inc.
P. O. Box 5040
Kent, WA 98031

Dr. P. Bradshaw
Imperial College of Science and
Technology
Department of Aeronautics
Prince Consort Road
London SW7 2BY, England

Professor T. Cebeci
Mechanical Engineering Department
California State University, Long
Beach
Long Beach, CA 90840

Engineering Library
University of Southern California
Box 77929
Los Angeles, CA 90007

Commanding Officer
Naval Ordnance Station
Louisville, KY 40214

Professor E. R. G. Eckert
University of Minnesota
241 Mechanical Engineering Building
Minneapolis, MN 55455

Dr. Gary Chapman
Mail Stop 227-4
Ames Research Center
Moffett Field, CA 94035

Library
Naval Postgraduate School
Monterey, CA 93940

Engineering Societies Library
345 East 47th Street
New York, NY 10017

Professor G. Miller
Department of Applied Science
New York University
26-36 Stuyvesant Street
New York, NY 10003

Office of Naval Research
New York Area Office
715 Broadway - 5th Floor
New York, NY 10003

Librarian, Aeronautical Library
National Research Council
Montreal Road
Ottawa 7, Canada

Lockheed Missiles and Space Company
Technical Information Center
3251 Hanover Street
Palo Alto, CA 94304

Commanding Officer
Office of Naval Research
Western Regional Office
1030 East Green Street
Pasadena, CA 91106

Engineering Division
California Institute of Technology
Pasadena, CA 91109

Library
Jet Propulsion Laboratory
4800 Oak Grove Drive
Pasadena, CA 91103

Professor H. Liepmann
Department of Aeronautics
California Institute of Technology
Pasadena, CA 91109

Mr. L. I. Chasen, MGR-MSD Lib.
General Electric Company
Missile and Space Division
P. O. Box 8555
Philadelphia, PA 19101

Technical Library
Naval Missile Center
Point Mugu, CA 93042

Professor S. Bogdonoff
Gas Dynamics Laboratory
Department of Aerospace and
Mechanical Sciences
Princeton University
Princeton, NJ 08540

Dr. J. E. Yates
Aeronautical Research Associates
of Princeton, Inc.
50 Washington Road
Princeton, NJ 08540

Redstone Scientific Information Center
Chief, Document Section
Army Missile Command
Redstone Arsenal, AL 35809

U.S. Army Research Office
P. O. Box 12211
Research Triangle, NC 27709

Editor, Applied Mechanics Review
Southwest Research Institute
8500 Culebra Road
San Antonio, TX 78228

Library and Information Services
General Dynamics - CONVAIR
P. O. Box 1128
San Diego, CA 92112

Office of Naval Research
San Francisco Area Office
One Hallidie Plaza, Suite 601
San Francisco, CA 94102

Library
The RAND Corporation
1700 Main Street
Santa Monica, CA 90401

Dr. P. E. Rubbert
Boeing Aerospace Company
Boeing Military Airplane Development
Organization
P. O. Box 3707
Seattle, WA 98124

Librarian
Naval Surface Weapons Center
White Oak Laboratory
Silver Spring, MD 20910

Engineering Library
McDonnell Douglas Corporation
Department 218, Building 101
P. O. Box 516
St. Louis, MO 63166

Dr. N. Malmuth
Rockwell International Science Center
1049 Camino Dos Rios
P. O. Box 1085
Thousand Oaks, CA 91360

Library
Institute of Aerospace Studies
University of Toronto
Toronto 5, Canada

Professor W. R. Sears
Aerospace and Mechanical Engineering
University of Arizona
Tucson, AZ 85721

Air Force Office of Scientific
Research (SREM)
Building 1410, Bolling AFB
Washington, DC 20332

Chief of Research and Development
Office of Chief of Staff
Department of the Army
Washington, DC 20310

Library of Congress
Science and Technology Division
Washington, DC 20540

Director of Research (Code RR)
National Aeronautics and Space
Administration
600 Independence Avenue, SW
Washington, DC 20546

Library
National Bureau of Standards
Washington, DC 20234

National Science Foundation
Engineering Division
1800 G. Street, NW
Washington, DC 20550

AIR 320D
Naval Air Systems Command
Washington, DC 20361

AIR 950D
Naval Air Systems Command
Washington, DC 20375

Code 2627
Naval Research Laboratory
Washington, DC 20375

SEA 03512
Naval Sea Systems Command
Washington, DC 20362

SEA 09G3
Naval Sea Systems Command
Washington, DC 20362

Dr. Charles Watkins
Head, Mechanical Engineering Dept.
Howard University
Washington, DC 20059

Dr. A. L. Slafkosky
Scientific Advisor
Commandant of the Marine Corps
(Code AX)
Washington, DC 20380

Director
Weapons Systems Evaluation Group
Washington, DC 20350

Research Library
AVCO Corporation
Missile Systems Division
201 Lowell Street
Wilmington, MA 01887

AFAPL (APRC)
AB
Wright Patterson AFB, OH 45433

4-
DT